Universität Bremen

ALFRED-WEGENER-INSTITUT
HELMHOLTZ-ZENTRUM FÜR POLAR- UND MEERESFORSCHUNG

The ocean mesoscale in a warming world:

insights from multiscale modeling

Dissertation

in fulfillment of the requirements for the degree of

Doctor rerum naturalium

Submitted to the

University of Bremen

Faculty 1 – Physics and Electrical Engineering

By

Nathan Beech

29.02.2024

Reviewers

1. Prof. Dr. Thomas Jung,

Alfred Wegener Institute, Helmholtz Centre for Polar and Marine Research, Climate Dynamics

University of Bremen

2. Prof. Dr. Torsten Kanzow,

Alfred Wegener Institute, Helmholtz Centre for Polar and Marine Research, Physical Oceanography of the Polar Seas

University of Bremen

Date of colloquium: 24.05.2024

Abstract

State-of-the-art climate models and computing infrastructure are now able to resolve mesoscale ocean eddy activity in many contexts. However, in computationally intensive model applications, such as the Coupled Model Intercomparison Project (CMIP) or simulations of the high latitudes, grid resolutions largely remain eddy-parameterizing due to resource constraints. These missing mesoscale processes are understood to be crucial drivers of ocean circulation and climate and may become still more relevant in the context of anthropogenic climate change. To overcome the computational limitations of traditional models, multiscale modeling strategies have been developed which can distribute grid resolution and resources based on resolution requirements and research goals. Here, several strategies for resolving the mesoscale using multiscale methods are described and the results of their implementation with the Finite volumE Sea ice Ocean Model (FESOM) are reported. In the first application, FESOM participates in CMIP6 with the strategy of concentrating computational resources on the major eddy-rich regions of the ocean. The resulting simulations are able to reproduce between 51 and 82% of observed eddy kinetic energy (EKE) in each region and project substantial climate change impacts on mesoscale activity for the first time at such a scale. The results include a poleward shift of eddy activity in most western boundary currents; EKE intensification in the Antarctic Circumpolar Current (ACC), Brazil and Malvinas Currents, and Kuroshio Current; EKE decline in the Gulf Stream; and intensification of Agulhas leakage. In a second application, FESOM is used to concentrate computational resources in the Southern Ocean and cost-reducing modeling strategies are used to enable fully eddy-resolving climate change projections with the regionally focused grid. The simulations faithfully reproduce EKE in the Southern Ocean and project intensified eddy activity in line with the CMIP6 analysis. The climate change signal is difficult to reliably discern from natural variability after 1 °C of warming, but becomes clear after 4 °C. Finally, the high-resolution Southern Ocean simulations are used to investigate high-latitude eddy activity where ice cover and low eddy size make observations and traditional modeling methods difficult. Detailed, near circumpolar mesoscale activity is detected and related to gyre circulation, the Antarctic Slope Current, and bathymetry. There is a strong seasonal cycle which suppresses winter eddy activity at the surface and selectively dampens cyclonic eddies. After prolonged anthropogenic warming, broad intensification of eddy activity occurs alongside regional decline, ACC eddy activity encroaches further into the high latitudes, and the seasonal cycle is diminished. Collectively, this

work demonstrates the effectiveness of multiscale modeling in reducing the cost of resolving mesoscale ocean activity, facilitating the study of eddy activity and its interactions with the broader climate in previously unachievable contexts.

Table of Contents

1

Introduction

1.1 Ocean eddy activity and its relevance

Transient oceanic flows fill the global oceans, spanning scales of a few to a few hundred kilometers, or the mesoscale, and representing the majority of kinetic energy in the ocean (von Storch et al., 2012). Collectively, these flows are termed eddy activity and when they form coherent, ring-like structures, they are called eddies. Eddy activity arises from baroclinic or barotropic mechanisms; the former when available potential energy stored within strong density gradients is converted to eddy kinetic energy (EKE), and the latter when mean kinetic energy within largescale flows like currents is converted into EKE. Considering these generation mechanisms, it is not surprising that EKE is concentrated along the energetic western boundary currents of the global oceans (Cheney et al., 1983). However, by tracking coherent eddy structures and identifying eddy presence, it is revealed that this activity is not limited to certain regions, but extends virtually throughout the observable ocean (Chelton et al., 2011). Thus, the impacts of eddy activity, while potentially of varying magnitude, are nonetheless ubiquitous.

As the scientific understanding of ocean circulation has expanded to ever finer scales, the importance of eddy activity has been acknowledged in a growing number of fields. Eddies are known to introduce a nutritional foundation for marine life to regions that can otherwise be relatively static (Falkowski et al., 1991; Oschlies, 2002; Oschlies & Garçon, 1998) and this ecological role extends up trophic levels to marine mammals (Bailleul et al., 2010). Likewise, eddy activity can damage ecosystems by introducing extremes or unfavorable conditions like heatwaves (Bian et al., 2023; Gruber et al., 2011). Consequently, direct relationships between eddy activity and human economic activity are clear (Hobday & Hartog, 2014; Hsu et al., 2015). More separated from human activity, but perhaps ultimately more impactful, are the effects that eddy activity has on broader ocean circulation and the climate. The oceans are a major sink of

anthropogenic carbon (Gruber et al., 2019; Sabine et al., 2004) and eddies facilitate much of the sequestration across the atmosphere-ocean boundary (Ford et al., 2023; Sallée et al., 2012), effectively slowing anthropogenic climate change. Eddies impact near-surface atmospheric conditions including winds, temperature, and precipitation (Frenger et al., 2013), even from beneath sea ice (Huot et al., 2022), and many eddies span over 1000 m vertically, or even the entire water column, connecting disparate ocean layers through coherent structures (Petersen et al., 2013). Both upwelling and downwelling can be facilitated by eddies through numerous mechanisms, but primarily through Ekman pumping generated by the gradient of eddy-induced Ekman transport between the eddy core and perimeter (Gaube et al., 2015; Häkkinen, 1986; Mahadevan et al., 2008). Net vertical transport can depend on an eddy's rotational direction, thermohaline characteristics and surface wind speed, direction, or gradients. Although complex and contradictory vertical transports can occur within eddy populations and even individual eddies, under the right circumstances, the net transport can contribute to processes ranging from deep ocean heat entrainment to global meridional overturning circulation (MOC; Georgiou et al., 2019; Thompson et al., 2014). Through trapping, the entrainment and transport of a water mass within the eddy core (Early et al., 2011; Nakano et al., 2013), and stirring, the local mixture of water masses across density gradients facilitated by eddy rotation (Frenger et al., 2015), eddy activity can flatten isopycnals and modulate horizontal density gradients. This is particularly important for facilitating transport across jets and over continental slopes (Malan et al., 2020; Stewart et al., 2018; Stewart & Thompson, 2015). While an exhaustive description of eddy effects on ocean circulation and climate is beyond the scope of this dissertation, the importance of eddy activity across scientific fields should be clear.

Considering the range of impacts that eddy activity has on critical oceanic processes, it is no surprise that high-quality model simulations are substantially improved when these processes are accounted for. One can reasonably assume that the aforementioned processes are better represented in eddy-resolving models than coarser models, but improvements to broader oceanographic circulation features and bias reductions are also detailed extensively in numerical experiments; in the North Atlantic, eddy-resolving models tend to more accurately reproduce Gulf Stream separation and deep ocean penetration (Chassignet & Xu, 2017; Hurlburt & Hogan, 2008; Sein et al., 2017). In the Southern Ocean, resolved eddy activity improves the modeled representation of overturning circulation and its response to wind forcing (Hallberg & Gnanadesikan, 2006). In the Kuroshio Current, resolving eddies improves the modeled representation of both flow strength and the response to anthropogenic warming (An et al.,

2023). Although locally resolving high-latitude eddy activity is beyond the limitations of most simulations, the impacts of resolving lower-latitude eddy activity can extend to the polar oceans; both Arctic sea surface temperatures and surface currents and the response of Southern Hemisphere sea ice to anthropogenic warming are improved by lower-latitude eddy activity (Docquier et al., 2019; Rackow et al., 2022). In general, ocean models with eddy-resolving horizontal resolution tend to reduce common biases in ocean heat content, salinity, and velocity, although regionally, biases can worsen or appear (Chassignet et al., 2020; Griffies et al., 2015; Hewitt et al., 2020; von Storch et al., 2016).

With an understanding of the role that eddies play in both the real oceans and the simulated, two major roles for eddy-resolving numerical modeling are apparent: firstly, models can serve as digital observation platforms helping to deepen the understanding of eddy activity from a physical and process-based perspective. This could take the form of studying eddies themselves, or their interactions with and impacts on the broader ocean and climate. Second, model simulations with the aim of faithfully reproducing the Earth system can use eddy activity as a source of model skill, improving the reliability of crucial climate information such as projections of anthropogenic climate change. Of course, both of these use cases carry challenges and alternatives; physical processes can be studied using observations, although observation of the ocean is also challenging, particularly at the mesoscale (Weller et al., 2019). Lower-resolution models can parameterize the effects of eddy activity rather than resolving them explicitly, lowering computational costs, but imperfectly representing eddy effects (Gent, 2011). To judge the appropriateness of eddy-resolving simulations and their alternatives, an understanding of the cost of each approach is essential.

1.2 The mesoscale challenge

1.2.1 Observations

Mesoscale activity in the ocean is most often observed via satellite altimetry which measures the sea surface height directly beneath the path of a satellite's orbit. This effectively produces linear datasets of sea surface height, with isolated crossover points where higher frequency data is available (Cheney et al., 1983). Remapping algorithms are then applied to the data, producing gridded data products which are effective outside of the equatorial region and until sea ice veils the ocean surface from satellite view (Taburet et al., 2019). For an observational dataset, the gridded altimetry product is relatively comprehensive in horizontal space, but the quality of the interpolated data can be less robust than the 0.25° regular grid and 10-day

frequency may at first appear (Ballarotta et al., 2019). Regarding mesoscale features, these data products are known to perform poorly in particular regions, primarily the higher latitudes, and can include erroneous mesoscale structures as a result of aliasing over smaller features (Amores et al., 2018). In the polar regions, traditional altimetry maps include large data gaps during the ice-covered season and lower data quality during periods of partial sea ice cover. Recently, approaches using sea ice leads have been developed to provide some data in ice-covered regions (Auger et al., 2022). For this altimetry product, the effective resolution of the data becomes the limiting factor as the typical eddy size shrinks in higher latitudes and the average eddy lifespan becomes shorter. Regardless of the quality of the measurements, the relatively short altimetry record may be insufficient to discern a reliable climate change signal within poorly quantified natural variability and these results can vary between ocean basins (Beech et al., 2022; Martínez-Moreno et al., 2021).

In the lower latitudes, the detection of eddies from in-situ observation platforms is largely overshadowed by satellite and model-based methods due to their far greater spatial coverage and temporal frequency. Additionally, since the altimetry dataset is relatively reliable in these regions and models are better constrained by observations, reliance on either method is generally justified. Nonetheless, in situ observations, typically from drifters, mooring arrays, and ship-deployed instruments, can augment satellite data by providing subsurface information and additional variables like temperature, salinity, or biogeochemical characteristics (Frenger et al., 2015; Li et al., 2020; Yang et al., 2013; Zhang et al., 2016). Conversely, in the higher latitudes, in-situ observations represent the bulk of the observations, but these too are scarce due to the remoteness and ice cover of the polar regions. Here, ice-tethered profilers and ship-based instruments are most common (Manucharyan & Timmermans, 2013; Meneghello et al., 2020; Timmermans et al., 2008; Zhang et al., 2016), although several satellite-based methods are used during periods of partial ice cover (Auger et al., 2022; Kozlov et al., 2019; Manucharyan & Thompson, 2022), on-ice observation stations were used historically (Manley & Hunkins, 1985), and under-ice drifters and moorings are increasingly deployed to more remote regions (Sallée et al., 2023; Wallace et al., 2020). Taken together, research based on a variety of methods manages to touch on a relatively comprehensive range of mesoscale activity in 3-dimensional space, year-round, and with a variety of information. Yet, some estimates place the effectiveness of eddy detection using the lower latitude altimetry dataset between 6 and 16% (Amores et al., 2018), altimetry products of ice-covered regions are too coarse to resolve the local Rossby radius and presumably the bulk of the eddy population (Auger et al., 2023), and the sum of eddy

observations from in-situ sources is a fraction of the population that models and satellites detect (Chelton et al., 2011; Frenger et al., 2015). Consequently, the prospect for numerical models to provide extensive and complete datasets of mesoscale activity is attractive.

1.2.2 Models

To this day, many ocean models employ a grid resolution on which mesoscale processes are sub-gridscale. In other words, physical properties within the modeled space are defined on grid cells larger than a mesoscale structure, effectively reducing the complexity of such structures to an average of their properties. These models use parameterizations to mimic the impacts of mesoscale activity without explicitly resolving them (e.g. Gent & McWilliams, 1990) by adding terms to the fundamental physical equations, modifying the transfer of physical properties in space as a numerical simulation progresses. The exact effects of the parameterizations are estimates derived from the explicitly resolved, larger-scale properties of the same model space using relationships based on theoretical or empirical evidence. This approach is evidently imperfect based on the comparisons of eddy-resolving and parameterizing numerical experiments detailed above, but its advantage is that it comes at almost no additional cost relative to solving the physical equations without the additional terms. The alternative is to reduce the size of the cells within the model domain for which physical properties are calculated until mesoscale structures can be resolved and their effects arise naturally within unchanged physical equations. The tradeoff then, is the number of computations that must be performed in order to physically characterize the same space with greater detail.

Decreasing the grid spacing of a traditional, rectangular model grid increases the number of grid cells in an area by the square of the factor of the decrease (Eq. 1.1). Finer grids also tend to increase the computational cost of a simulation further due to shorter model timesteps, more vertical layers, and scaling inefficiencies in computational infrastructure (Balaji et al., 2017; Koldunov et al., 2019).

(Eq. 1.1) $$N_{grid} = A_{grid} / {D_{grid}}^2$$

where N_{grid} is the number of grid cells, A_{grid} is the horizontal area the grid covers, and D_{grid} is the spacing between points on the grid.

With the aim of resolving eddy activity, the extent to which a grid must be defined is primarily determined by the first baroclinic Rossby radius of deformation. This describes the length scale at which the influence of Earth's rotation is of comparable scale with buoyancy forces (Chelton et

al., 1998) and is a strong approximation of local eddy radii in the global ocean. The Rossby radius varies primarily with latitude and the depth of the water column, meaning eddy-resolving model grid resolutions are quite variable in a global context. For traditional ocean models with limited horizontal resolution flexibility, this further increases the computational cost of resolving the mesoscale, as the lowest Rossby radius in a study region influences the necessary resolution for the entire region. From a global perspective, the lowest Rossby radii will occur at the poles and over continental shelves, where mesoscale eddies can be as small as a few kilometers in diameter. Finally, for mesoscale structures to form in a numerical simulation, model grid spacing must be approximately one half of the local Rossby radius or finer (Hallberg, 2013). However, a range of eddy sizes occurs in all regions, meaning some eddies will be smaller than the local Rossby radius suggests. Therefore, grid spacing of one half the Rossby radius is not always enough to effectively capture the extent of eddy activity in a region (Sein et al., 2017).

In the current state of ocean modeling and computational science, eddy-resolving resolutions are well within the capabilities of state-of-the-art high-performance computing infrastructure when certain tradeoffs are made; resolving the mesoscale tends to preclude other sources of model skill and reliability such as multiple ensemble members, model complexity, tuning, or spin-up length, all of which come at a computational cost of their own. For example, in CMIP6, some of the most robust hindcasts of historical climate and projections of anthropogenic climate change (Eyring et al., 2016), ocean resolutions are almost exclusively too coarse to resolve eddy activity (Hewitt et al., 2020). Even simulations that are broadly considered eddy-resolving, in practice, only have sufficient resolution to resolve eddies in the low to mid-latitudes. Thus, while eddy-resolving model simulations are not uncommon, there are major gaps in the scientific literature regarding the role of eddy activity in the ocean and climate system. Meanwhile, over the past several decades of climate model development, the bulk of advances in model resolution and simulation complexity have come from the exponential growth in computational technology and resources (Balaji et al., 2017; McGuffie & Henderson-Sellers, 2001). Improvements in model efficiency have been modest by comparison (Bauer et al., 2021). Now though, it is increasingly accepted that the rate of advances in computational technology is slowing (Khan et al., 2018) and this deceleration will have direct consequences for the feasible complexity of climate and ocean simulations. Therefore, addressing eddy-related knowledge gaps in climate and ocean science may depend on reducing the computational cost of resolving the mesoscale.

1.3 Multi-scale modeling

In the face of computational challenges for ocean and climate modeling, variable-resolution model grids have emerged as one method to reduce costs by selectively resolving certain scales in certain regions (Danilov, 2013; Ringler et al., 2013). The variable-resolution strategy is particularly effective in the context of resolving mesoscale activity due to the regional inefficiencies of global models without versatile resolutions. Specifically, the global variability of the Rossby radius makes grid resolution requirements highly variable in space. Moreover, eddy activity is concentrated in certain regions and researchers often have specific regional foci independent of large parts of the ocean. Consequently, simulating parts of the mesoscale field and omitting others could drastically reduce simulation costs. The Finite volumE (formerly Element) Sea ice Ocean Model (FESOM; Danilov et al., 2017a; Wang, Danilov, et al., 2014) is one of the most mature models with these capabilities, having been the first variable-resolution model to participate in CMIP (Semmler et al., 2020) and now boasting an extensive record of evaluation and applications (e.g. Li et al., 2024; Rackow et al., 2018; Sánchez-Benítez et al., 2022; Scholz et al., 2019, 2022; Sidorenko et al., 2015). FESOM employs an unstructured triangular mesh, making grid resolution highly flexible as opposed to semi-flexible methods such as nesting (e.g. Schwarzkopf et al., 2019). While there are advantages to the unstructured grid in terms of resource allocation, these models tend to have lower computational efficiency per grid cell compared to regular grids: a problem that affected earlier versions of FESOM more than the most recent ones (Biastoch et al., 2018; Koldunov et al., 2019). However, FESOM also scales more effectively than traditional models, meaning more effective use can be made of substantial computing power and high throughput can be achieved (Koldunov et al., 2019). More importantly for the subject at hand, is that more ocean grid cells are not necessarily more effective at resolving mesoscale activity if they cannot be allocated dynamically. Thus, when employed strategically, the multi-scale capabilities of FESOM can produce a computational advantage over traditional models. In the following chapters, more details regarding FESOM in its various configurations will be outlined in detail. Here, strategies for simulating the mesoscale efficiently with multiscale grids will be outlined in the context of the knowledge gaps and practical challenges described above.

High flexibility regarding horizontal model resolution presents several avenues for approaching eddy-resolving numerical simulations. Given the variability of the Rossby radius at different latitudes and water column depths, a multi-resolution grid can be used to limit the

horizontal resolution to local requirements for resolving eddy activity. Compared to a completely inflexible grid, this would shift the determination of grid resolution requirements from a function of the smallest Rossby radius in the study region to the local Rossby radii throughout. However, in a global simulation, the cost to simulate eddy activity using this strategy would remain high. Further limiting eddy-resolving conditions to eddy-rich regions, namely the western boundary currents and ACC, would make simulations more achievable and could still capture the bulk of the EKE in the global ocean. Alternatively, regionally focused studies may include highly refined regions while limiting resolutions in the majority of the global ocean to more affordable levels. This approach has several advantages over fully regional models with prescribed boundaries; by creating a regional focus within a global simulation, feedbacks with external processes that may not require high resolution can be included. As well, multiple, separated features can be allocated resources based on their relevance, rather than proximity, to a study region. For example, narrow straits needed to facilitate inter-basin exchange can be refined, or major ocean currents can be prioritized in addition to a study region.

FESOM has now been deployed in numerous configurations exploiting the various advantages of multiscale modeling. The effectiveness of various resource allocation strategies has been evaluated in terms of reproducing observed or expected eddy activity, as well as reducing model bias in idealized and realistic configurations (Sein et al., 2016, 2017). The fully flexible model grid has been evaluated relative to the semi-flexible nesting approach in terms of model fidelity and computational cost (Biastoch et al., 2018), and regionally focused grids have been employed for practical applications (Wang et al., 2020; Wekerle et al., 2017). Now, FESOM's multiscale capabilities will be directed toward the challenge of resolving the mesoscale and addressing the knowledge gaps and research challenges outlined above.

1.4 Structure and aims

This introduction has introduced the scarcity of mesoscale processes in both simulations and observations of the high latitudes, as well as most robust projections of climate change as knowledge gaps in current oceanographic and climate science. The challenges impeding eddy-resolving simulations using numerical models have been identified primarily as the high computational costs of increasing model resolutions over long time series and where the Rossby radius is low. Multiscale modeling strategies have been proposed to address these challenges and the ocean model FESOM has been presented as a suitable tool to this end. Next, Chapters 2 to 4 will outline efforts to implement these strategies and their results. These chapters are each

complete studies that are intended to stand independently of this unifying introduction, and therefore, each has its own introduction, methodology, and interpretation of results. Each has either been published or is in preparation for publication and citations are given at the beginning of the respective chapters. In Chapter 5, the dissertation is concluded with a synthesis of the key results of the cumulative work and a brief discussion of opportunities for further research.

In Chapter 2, FESOM's contribution to CMIP6 is used to produce the first long-term projections of ocean eddy activity in the context of climate change. The multiscale strategy in these simulations was to focus computational resources on the eddy-rich regions of the global ocean, primarily the mid-latitude western boundary currents and the ACC. Eddy resolving or permitting conditions were achieved in these regions at the expense of resolution in relatively lower-activity regions, such as gyre interiors, and in regions where resolving eddy activity was infeasible, mainly the high latitudes. The ocean grid was of comparable size to a traditional 0.25° model, but due to the selective refinement was able to simulate eddy activity more effectively than its peers. As a result, substantial and diverse changes in EKE are projected and related to broader impacts of anthropogenic climate change.

In Chapter 3, the results of FESOM's CMIP6 simulations are used as a baseline for the evaluation of a new model configuration, this time with a regional focus on the Southern Ocean, higher resolution in the study region, and more cost-reducing measures. In short, the simulations make use of reduced-resolution spin-up and transient simulations to initialize brief, high-resolution time slice simulations at various points during the progression of anthropogenic climate change. The high-resolution setup is able to reproduce the observed magnitudes of eddy activity accurately, something that the CMIP6 configuration could not, but changes relative to historic conditions are similar to those projected by FESOM in CMIP6. These results are used to assess the reliability of the substantially streamlined simulations and serve as a proof of concept for simulation designs that minimize computational cost to enable truly cutting-edge grid resolutions.

In Chapter 4, the high-resolution simulations introduced in Chapter 3 are used to study mesoscale activity in the high-latitude Southern Ocean, where observations are scarce and numerical models struggle to resolve eddy activity. The analysis is a uniquely pan-Antarctic view of the high-latitude mesoscale ocean and boasts 3-dimensional spatial coverage, unobstructed year-round detail, and projections of climate impacts. This region hosts several key climatic drivers and mediators which may become even more impactful as feedback mechanisms for

anthropogenic warming. The role of mesoscale activity in these processes is explored, both historically, and as a missing feature in virtually all major projections of climate change.

To conclude the dissertation, the effectiveness of multiscale modeling is discussed considering the results of the three studies and the stated goals of improving mesoscale representation in models and filling knowledge gaps regarding mesoscale activity in the climate system. The conclusions identify both the accomplishments and shortcomings of the work, drawing on both to propose avenues for future research. Beyond methodology, the key findings that FESOM was able to reveal regarding the ocean mesoscale are reviewed, particularly in the context of climate change and in the high southern latitudes, where previously little was known.

2

Long-term evolution of ocean eddy activity in a warming world

This chapter is published under the same title in *Nature Climate Change* (Beech et al., 2022).

2.1 Abstract

Mesoscale ocean eddies, an important element of the climate system, impact ocean circulation, heat uptake, gas exchange, carbon sequestration and nutrient transport. Much of what is known about ongoing changes in ocean eddy activity is based on satellite altimetry; however, the length of the altimetry record is limited, making it difficult to distinguish anthropogenic change from natural variability. Using a climate model that exploits a variable-resolution unstructured mesh in the ocean component to enhance grid resolution in eddy-rich regions, we investigate the long-term response of ocean eddy activity to anthropogenic climate change. Eddy kinetic energy is projected to shift poleward in most eddy-rich regions, to intensify in the Kuroshio Current, Brazil and Malvinas currents and Antarctic Circumpolar Current and to decrease in the Gulf Stream. Modeled changes are linked to elements of the broader climate including Atlantic meridional overturning circulation decline, intensifying Agulhas leakage and shifting Southern Hemisphere westerlies.

2.2 Introduction

Since the advent of satellite altimetry, researchers have exploited the concept of geostrophy to characterize the movement of the near-surface ocean (Cheney et al., 1983; Heywood & McDonagh, 1994; Menard, 1983). By balancing the Coriolis force with the pressure gradient, geostrophic currents can be calculated until the Coriolis parameter becomes negligible near the equator (Lagerloef et al., 1999). These currents are accurate enough to identify both consistent, large-scale circulation features such as gyres and boundary currents and smaller short-lived phenomena such as eddies (Chelton et al., 2011). The major drivers of ocean eddies

are barotropic and baroclinic instability that convert mean kinetic energy and available potential energy from the mean flow of ocean currents into eddy kinetic energy (EKE; Constantinou & Hogg, 2019; Gill et al., 1974; Ogata & Masumoto, 2011). These mechanisms connect eddy-rich regions to the paths of major ocean surface flows including gyres and boundary currents, although other factors, such as bathymetry (Endoh & Hibiya, 2001; Heywood & McDonagh, 1994) and wind stress (Hogg et al., 2015), also influence eddy activity. Eddies subsequently impact physical and biological ocean systems through ventilation (Lachkar et al., 2009; MacGilchrist et al., 2017), volume transport (Wang et al., 2017), carbon sequestration (Sallée et al., 2012) and heat and nutrient transport (Crews et al., 2018; Falkowski et al., 1991; Oschlies & Garçon, 1998), fuelling the interest in ocean eddy research.

Early altimetry studies were able to identify western boundary currents as eddy-rich regions and estimate their energy content, spatial scale and movement during the first brief periods for which data were available (Cheney et al., 1983; Menard, 1983). More recent altimetry studies have taken advantage of growing datasets to evaluate variability and change in ocean surface velocities and eddy fields and generally detect modest linear changes (Ding et al., 2018; Hogg et al., 2015; Martínez-Moreno et al., 2019, 2021), although some caution that much longer datasets will be necessary for robust results (Chi et al., 2021). Just as satellite altimetry overcame the spatial and temporal limitations of in situ velocity observations, modern numerical climate models can overcome the temporal limitations of the observational record by simulating datasets longer than the altimetry record will grow for generations to come. However, the length, resolution and ensemble size of model simulations are constrained by computational efficiency and resources.

In the sixth phase of the Coupled Model Intercomparison Project (CMIP6; Eyring et al., 2016), the average ocean resolution is approximately 60 km (Hewitt et al., 2020), which is insufficient to resolve eddies in most of the global ocean. At low latitudes, eddy-present simulations require resolutions of approximately 25 km or finer, and eddy-rich simulations require resolutions of approximately 10 km or finer. At higher latitudes, where the local Rossby radius decreases and the size of ocean eddies shrinks accordingly, resolution demands become greater and even at eddy-rich and eddy-present resolutions, certain characteristics of eddies, including size and frequency, may still not be entirely captured by models (Moreton et al., 2020).

In the face of limited computing resources and a demand for finer resolutions in ocean modeling, it is advantageous to reduce net computational effort relative to grid resolution.

Existing modeling studies of ocean eddies tend to rely on idealized simulations (Hogg et al., 2015), ocean-only models (Patara et al., 2016; Penduff et al., 2011) or simulations limited in spatial coverage, ensemble size or length (Crews et al., 2018; Grist et al., 2021; Regan et al., 2020; Wang et al., 2017). In contrast, the Finite Element Sea-ice Ocean Model (FESOM; Danilov et al., 2004; Wang, Danilov, et al., 2014) enables the concentration of computational resources via an unstructured mesh with which the spatial resolution of regions can be adjusted based on relevance to the global climate system and the needs of the user (Sein et al., 2016, 2017; Wang, Danilov, et al., 2014). This variable-resolution capability, along with excellent scalability (Koldunov et al., 2019), allows FESOM to regionally resolve small-scale ocean processes before similar simulations using regular grids can feasibly achieve the necessary resolution throughout the global ocean. FESOM participated in CMIP6 and contributed to the Intergovernmental Panel on Climate Change's Sixth Assessment Report as the ocean component of the coupled model AWI-CM-1-1-MR (Semmler et al., 2018, 2020), uniquely facilitating eddy-rich and eddy-present ocean resolutions in selected regions (Supplementary Figs. A1, A2) within the already computationally demanding CMIP framework.

In this study, the CMIP6 simulations from AWI-CM-1-1-MR (Semmler et al., 2018, 2020), in which fundamental aspects of mesoscale eddy activity are remarkably well reproduced (Fig. 2.1), are used to assess historical and future changes in EKE given ongoing anthropogenic climate change. Methodology is tailored to the dataset to address challenges in analysing EKE within a changing climate. Consistency with the CMIP framework will allow results to be interpreted in the context of more comprehensive climate change research, such as the Intergovernmental Panel on Climate Change assessment reports, and a wealth of other climate change projections. The satellite altimetry record is put into the perspective of prolonged warming under historical emissions, and a projected emissions scenario and potential physical mechanisms behind simulated EKE changes are investigated.

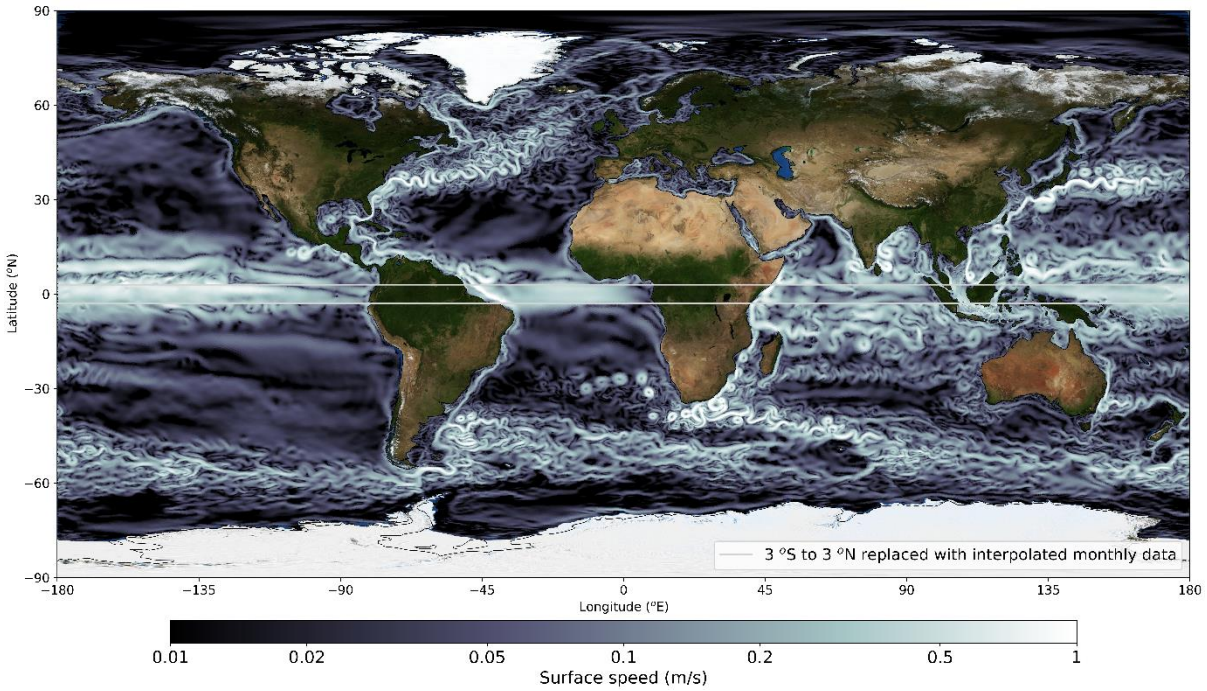

Figure 2.1. Magnitudes of simulated geostrophic ocean surface velocities. A snapshot of geostrophic velocities calculated from sea surface heights simulated by AWI-CM-1-1-MR for CMIP6 historical simulations. The equatorial region highlighted by grey lines (3° S to 3° N) is replaced with monthly mean velocity after linear interpolation to five-day mean time steps. Background image: NASA Earth Observatory.

2.3 Model performance and contextualization of observations

AWI-CM-1-1-MR reproduces observed EKE with remarkable accuracy for a CMIP6 model (Fig. 2.2a,b), most of which are eddy parameterizing (Hewitt et al., 2020). The spatial distribution is particularly well represented compared with observed EKE from a gridded satellite altimetry product (Fig. 2.2b), with regions of high-eddy activity concentrated along well-known ocean surface currents, including western boundary currents and ocean gyres, and a band of high-eddy activity represented in the tropics. Nonetheless, there are some regions in which EKE representation is noticeably different, such as the lower-than-observed simulated EKE corresponding to preconditioned regions of insufficient grid resolution around the East Australian Current and the Mozambique Channel. EKE distribution in the North Atlantic follows a path more zonal than is observed, which reflects the common challenges of Gulf Stream separation bias and North Atlantic current representation in climate models often attributed to grid resolution (Drews et al., 2015; Wang, Zhang, et al., 2014). In FESOM, the path can be improved with higher model resolution, although this is not the only factor (Sein et al., 2017). Because the ocean grid of AWI-CM-1-1-MR can only be considered eddy-present in large parts of

major ocean currents (Supplementary Figs. A1, A2), it can be expected that modeled EKE is lower than is observed by satellites, ranging from about 51% of observed EKE in the Antarctic Circumpolar Current (ACC) to about 82% in the Kuroshio Current (Supplementary Table A1). The magnitude of EKE variability is more accurately resolved (Supplementary Table A2) but again underrepresents observations. This underrepresentation must be acknowledged as a limitation when interpreting EKE change within these simulations.

The internal variability of the modeled EKE ensemble over the 28-year observational period suggests that the signal-to-noise ratio of anthropogenic changes to natural variability is still quite low (Fig. 2.3). Despite this, previous analysis of the altimetry record has identified statistically significant positive linear trends in the Agulhas, ACC and Brazil and Malvinas currents (BMC), and non-significant increases have been identified in the Gulf Stream and Kuroshio (Martínez-Moreno et al., 2021). To contextualize these observations, simulated Gulf Stream EKE during the observational period (1993–2020) changes very little, and the ensemble spread includes both positive and negative trends (Supplementary Fig. A3), the observed period and the long-term projections (Supplementary Fig. A3). Thus, in most regions, the modeled results indicate that the length of the observational record is still insufficient to capture long-term EKE changes either in character or magnitude and that care must be taken when distinguishing anthropogenic change from natural variability. Differences in the magnitude of linear change over the observed and projected periods could be indicative of a nonlinear EKE response to anthropogenic forcing, nonlinear GHG emissions, high natural variability or a time of emergence of change occurring at some point during the observational period.

2.4 Eddy kinetic energy change

Unlike model performance and the coherence of simulated EKE change during the altimetry era, the long-term modeled projections of EKE cannot be validated using observations. Instead, they must be interpreted with respect to current knowledge of ocean circulation and climate dynamics, applicable historical analogues and the published literature. The following paragraphs will link the long-term projections of EKE to the potential physical mechanisms responsible for them, and by doing so, solidify the reliability of the modeled results.

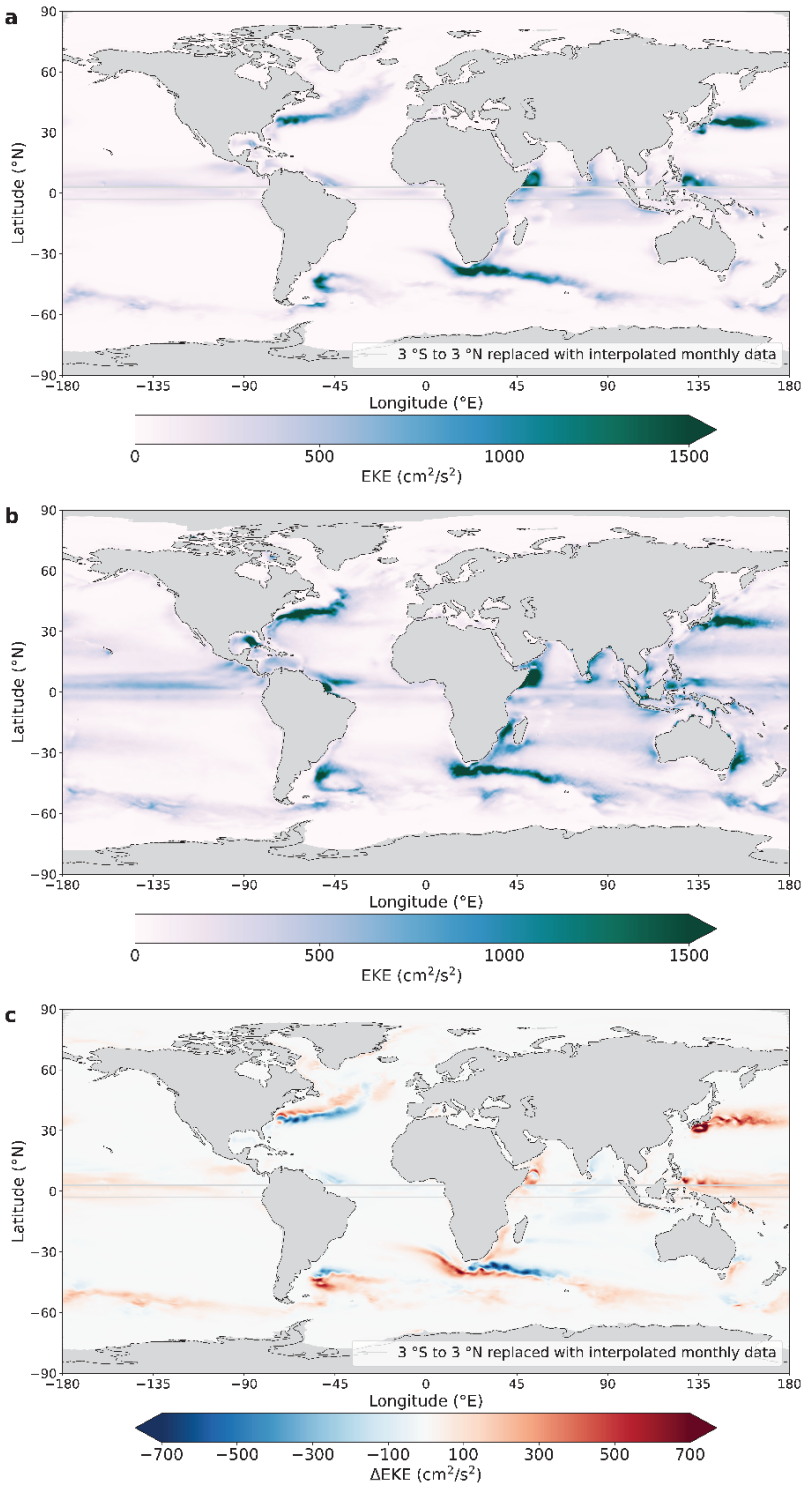

Figure 2.2. Simulated and observed eddy kinetic energy patterns in the global ocean. (a) Ensemble mean of simulated eddy kinetic energy during the observational period (1993–2020). **(b)** Observed mean eddy kinetic energy (1993–2020). **(c)** Change in ensemble mean of eddy kinetic energy between historical (1860–1949) and projected (2061–2090) periods with GHG forcing, according to SSP3–7.0.

2.4.1 The Gulf Stream

In addition to the widely anticipated poleward shift of the Gulf Stream (Caesar et al., 2018; Yang et al., 2016, 2020), the North Atlantic is projected to experience a major decrease in eddy activity over the twenty-first century (Fig. 2.3a). After a slight increase between the mid-twentieth century and the present, the ensemble mean of simulated EKE falls by approximately 2.5 standard deviations (σ) by 2090 at a rate of −0.84 σ °K^{-1} after mean global surface temperature (MGST) surpasses a 1 °K anomaly threshold (Figs. 2.3a, 2.4a). One explanation for this decrease could be simulated Atlantic Meridional Overturning Circulation (AMOC) weakening (Bakker et al., 2016), which is present in much of the CMIP6 ensemble (Weijer et al., 2020), including AWI-CM-1-1-MR (Supplementary Figs. A4, A5; Semmler et al., 2020) and would reduce volume transport through the upper Gulf Stream where eddy activity occurs. The modeled dataset reveals a relationship between unfiltered AMOC and Gulf Stream EKE of 0.23 σ Sv^{-1} (Supplementary Fig. A6), which, while significant, explains relatively little of the simulated interannual EKE variability in the Gulf Stream (R^2 = 0.10; Supplementary Fig. A6). Isolating low-frequency variability reveals a much stronger relationship of 0.36 σ Sv^{-1} (R^2 = 0.24; Supplementary Fig. A6), which suggests that EKE measured from satellite altimetry could be a fingerprint of long-term changes in AMOC strength.

2.4.2 The Kuroshio Current

Interestingly, the Kuroshio is the only western boundary current for which the eddy field is not projected to shift poleward (Fig. 2.2c). This has some precedence in the existing literature, as there is contradictory evidence regarding overall spatial change in the Kuroshio (Wu et al., 2012; Yang et al., 2016), and it exhibits a weaker poleward shift relative to natural variability compared with other western boundary currents (Yang et al., 2020). This exception may also be due to a disconnection between surface and subsurface flow in the region, which diverged in 2002, after which only the subsurface continued to shift poleward (Wu et al., 2021). Change in the magnitude of Kuroshio EKE is clearer; the ensemble mean increases by approximately 4 σ by 2090 and rises at a rate of 1.56 σ °K^{-1} after MGST surpasses a 1 °K anomaly threshold (Figs. 2.3b, 2.4b).

Notably, individual ensemble members exhibit periods of EKE in the Kuroshio substantially higher than the mean (for example, 2040–2050; Fig. 2.3b). Closer inspection of these periods reveals that changes between the Large Meander (LM) and Non-Large Meander (NLM) states of the Kuroshio (Endoh & Hibiya, 2001; White & McCreary, 1976) result in large

velocity anomalies along both paths. These anomalies are the result of a spatial oscillation in mean flow but can be misinterpreted as time-varying flow due to the bimodal nature of the path of the Kuroshio (Supplementary Video A1). It should, therefore, be concluded that the intermittent periods of particularly intense EKE in the Kuroshio (Fig. 2.3b) are not entirely representative of eddy activity, nor is the region of high EKE along the paths of the LM and NLM realistic (Fig. 2.2c). The same analysis of the observational dataset, which defines anomalies with respect to a reference period, reveals a similar pattern of intermittent eddy activity along the paths of the LM and NLM (Fig. 2.3b, Supplementary Video A2). This suggests that seemingly unrealistic high EKE in regions with spatially oscillating mean flow is an issue affecting methodology rather than the dataset. While distinguishing these periods of apparently high EKE from the overall eddy activity in the Kuroshio, there still appears to be an increase in the magnitude of EKE (Figs. 2.3b, 2.4b). Such an increase can be attributed to greater volume transport through the upper-layer Kuroshio, which increased by approximately 1 Sv, or 8% of the historical mean over the course of the simulations (Supplementary Figs. A4, A5, Supplementary Table A4). This response has been predicted in the context of climate change using both numerical models and observations as a result of intensified local wind stress (Zhang et al., 2017), ocean stratification (Chen et al., 2019) and tropical cyclones (Zhang et al., 2020). Further analysis of the relationship between Kuroshio volume transport and EKE is confounded by the correlation between high (low) volume transport and the LM (NLM) path (Kawabe, 1995), and by extension, the aforementioned unrepresentatively high EKE values. For this reason, correlation between EKE and volume transport in the Kuroshio is not investigated.

2.4.3 The Agulhas Current

Modeled results show the eddy-rich region corresponding to the Agulhas Current shifting westward and poleward as warming continues (Fig. 2.2c). A positive trend of $0.29\ \sigma\,°K^{-1}$ is identified in the Agulhas (Fig. 2.4c), and while statistically significant, temperature rise is a poor predictor of local EKE ($R^2 = 0.03$). Despite relatively little change in magnitude (Fig. 2.3c), EKE change in the Agulhas region can provide insight into local ocean circulation. The substantial projected intensification of eddy activity from the southern coast of Africa into the South Atlantic appears to be indicative of Agulhas leakage: the transport of warm, salty Indian Ocean water into the South Atlantic. Agulhas leakage tends to take the form of mesoscale activity (Lutjeharms & Ballegooyen, 1988; Olson & Evans, 1986) and simulated leakage approximated by volume transport (Supplementary Table A4) increases by approximately 6 Sv, or 28% of the historical mean, over the course of the simulations (Supplementary Figs. A4, A5).

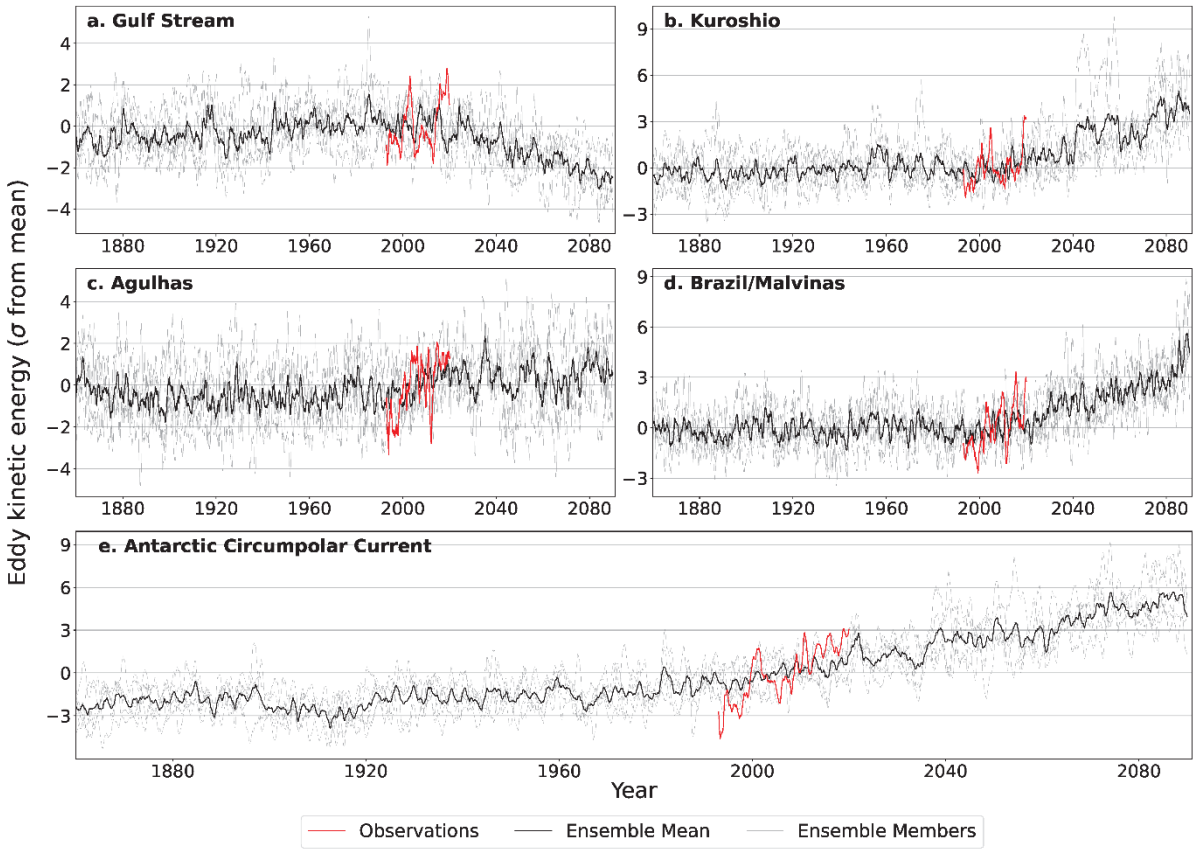

Figure 2.3. Regional eddy kinetic energy change. Observed and simulated area-integrated regional eddy kinetic energy anomalies normalized relative to conditions during the observational period (1993–2020). Sigma (σ) represents the standard deviation of conditions during the observational period (1993–2020) in each basin, respectively. **(a)** The Gulf Stream. **(b)** The Kuroshio Current. **(c)** The Agulhas Current. **(d)** BMC. **(e)** ACC.

Increased Agulhas leakage has been identified as a result of historical climate change using both hindcast modeling simulations (Biastoch et al., 2009) and observations (Backeberg et al., 2012; Rouault et al., 2009) and prior modeling studies have projected further increases as climate change continues (Biastoch & Böning, 2013). Proxy records have also linked increased inter-ocean exchange through the Agulhas to periods of rapid warming during transitions from glacial to interglacial conditions (Peeters et al., 2004), which could be analogous to anthropogenic climate change. Heat and salinity transported from the Indian Ocean to the South Atlantic by Agulhas leakage contribute to AMOC strength (Biastoch et al., 2008; Gordon, 1986; Knorr & Lohmann, 2003; Weijer et al., 1999), but the decline of AMOC in our simulations (Supplementary Figs. A4, A5, Supplementary Table A4) indicates that the overall effect of anthropogenic climate change on AMOC will be negative. High Agulhas leakage and a southwestward shift of the Agulhas retroflection have been associated with lower overall Agulhas transport (van Sebille et al., 2009).

Our simulations reinforce this association, as Agulhas volume transport is projected to decrease by 10 Sv or 15% of mean historical transport. EKE change in the Agulhas can be attributed to the poleward shift and intensification of Southern Hemisphere westerly winds (Backeberg et al., 2012; Bard & Rickaby, 2009; Biastoch et al., 2009; Cai, 2006) and this, too, is consistent with the modeled dataset in which mean zonal surface wind decreases between approximately 25–45° S and increases south of approximately 45° S (Supplementary Fig. A7).

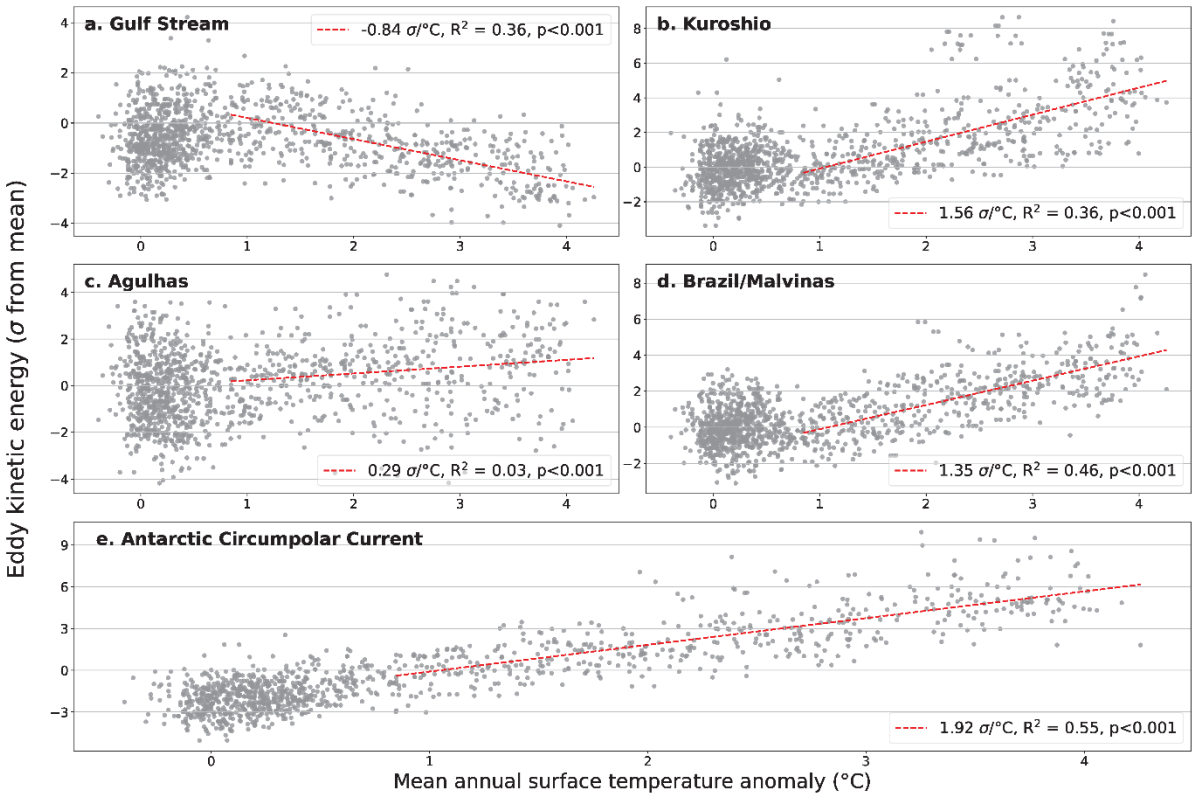

Figure 2.4. Regional eddy kinetic energy change relative to temperature rise. Simulated area-integrated regional eddy kinetic energy anomalies normalized relative to conditions during the observational period (1993–2020) and plotted relative to simulated mean annual surface temperature anomalies from mean conditions between 1850 and 1899. Linear trends are fit to EKE anomalies after an 11-year running mean of mean annual surface temperature anomalies surpasses 1 °K. **(a)** The Gulf Stream. **(b)** The Kuroshio Current. **(c)** The Agulhas Current. **(d)** BMC. **(e)** ACC.

2.4.4 The BMC

EKE in the BMC basin is projected to shift southward (Fig. 2.2c) and increase in magnitude by approximately 5 σ by 2090 (Fig. 2.3d) at a rate of approximately 1.35 σ °K^{-1} (Fig. 2.4d). The spatial EKE shift is corroborated by analysis of the relatively short observational record, which has already detected a modest southward shift of the currents in this region (Drouin et al., 2021;

Goni et al., 2011; Lumpkin & Garzoli, 2011). Independent numerical experiments have further corroborated this result (Combes & Matano, 2014; De Souza et al., 2019) and attribute the spatial shift of the BMC to a weakening of the Malvinas Current as Southern Hemisphere westerlies shift south. The simulations considered here produce similar conditions; westerlies shift south over the Southern Ocean (Supplementary Fig. A7), and volume transport through the Malvinas Current decreases by approximately 11 Sv, or 15% of the historical mean (Supplementary Figs. A4, A5, Supplementary Table A4). Observational studies of the intensity of transport through the BMC have generally found insignificant or no trends (Goni et al., 2011; Lumpkin & Garzoli, 2011), but palaeoclimatic evidence of ocean transport in the region may set a precedent for rising EKE. Sediment core proxy records have linked periods of high volume transport in the Brazil Current to weak AMOC (Chiessi et al., 2014; Meier et al., 2021), which is consistent with the approximately 3 Sv, or 17% decline of simulated AMOC in these simulations (Supplementary Figs. A4, A5, Supplementary Table A4). AMOC is a relatively strong indicator of BMC EKE, particularly considering low-frequency variability ($R^2 = 0.53$, Supplementary Fig. A6). The mechanism for this change theorized from proxy evidence is that as the northward removal of warm, salty water from the southern and tropical Atlantic lessens, transport shifts towards a southward route in response to a build-up of heat and salinity (Arz et al., 1999; Chiessi et al., 2014; Meier et al., 2021; Zhu & Liu, 2020). Once again, the modeled dataset supports this hypothesis; volume transport through the North Brazil Current decreases by approximately 2 Sv, or 6% of the historical mean, and increases through the Brazil Current by approximately 2 Sv, or 4% of the historical mean, over the course of the simulations (Supplementary Figs. A4, A5, Supplementary Table A4). Linear regression reveals significant relationships between BMC EKE and Brazil and North Brazil Current volume transport, particularly after isolating low-frequency variability (Supplementary Fig. A6).

2.4.5 The ACC

In the ACC, intensification of strong atmospheric westerly winds (Marshall, 2003) has already imparted more energy to the surface ocean via wind stress (Allison et al., 2010). This has increased Southern Ocean eddy activity while transport has remained stable according to the theory of eddy saturation (Munday et al., 2013). Our projections suggest this will continue throughout the twenty-first century (Supplementary Fig. A7), resulting in ensemble mean EKE approximately 6 σ greater than the observational period mean by 2090 (Fig. 2.3e). EKE is projected to rise at a rate of 1.92 σ °K^{-1} after the 1 °K MGST anomaly threshold (Fig. 2.4e). Meanwhile, transport through the Drake Passage decreased by approximately 2 Sv, or 1% of

historical mean annual transport (Supplementary Figs. A4, A5, Supplementary Table A4). Although a statistically significant change, this is most likely physically inconsequential to the local conditions, suggesting that the ACC simulated by FESOM is at or near its eddy-saturated state, where stronger winds no longer increase mean transport but instead intensify eddy activity. Interestingly, the ACC is the only basin considered here where simulated EKE rise begins before the start of the observational period (Fig. 2.3e), suggesting that observed trends here should already reflect long-term change. Indeed, simulated ACC EKE rises at approximately the same rate both during and after the observational period (Supplementary Fig. A3). However, it has been shown that EKE rise in response to wind stress along the ACC is greater in higher-resolution models (Munday et al., 2013), meaning EKE rise could be even more intense than these projections if a higher-resolution mesh is used.

2.5 Conclusions

Analysis of EKE in the world's oceans has historically been limited by the length of the satellite altimetry record and the computational challenge of modeling long time series at eddy-present resolutions. AWI-CM-1-1-MR, and specifically the ocean component, FESOM, contends with these challenges using a highly scalable dynamical core, along with an unstructured mesh and variable-resolution ocean grid. As a result, AWI-CM-1-1-MR's CMIP6 contribution is able to reproduce key features of global eddy activity, creating a unique opportunity to investigate how eddy activity might change in a warming world. Although AWI-CM-1-1-MR's unique characteristics have made this study possible, it will be essential for future work to corroborate the results using a diverse model ensemble.

Our analyses of CMIP6 simulations from AWI-CM-1-1-MR reveal pronounced long-term changes in projected EKE on a global scale. Early indications of these changes may be present in the observational record (Martínez-Moreno et al., 2021), but EKE changes in most eddy-rich regions do not yet appear to be wholly representative of long-term change either in character or magnitude. Nonetheless, the observational record is generally not contradictory to our results because modeled EKE change during the observational period is also not yet reflective of long-term projections in most regions. Importantly, the onset of EKE changes relative to both time and MGST rise suggests that these changes should become increasingly clear relatively quickly as the observational record grows, making the altimetry dataset a crucial tool for evaluating these projections. Several of the long-term modeled projections reflect changes that have begun to appear in the observational record or other existing literature. A poleward shift of eddy activity

follows the poleward shift of many major ocean currents expected in a warming climate (Wu et al., 2012; Yang et al., 2016, 2020). The ACC appears eddy-saturated as intensifying Southern Hemisphere westerlies increase eddy activity and ACC volume transport remains relatively stable (Munday et al., 2013). Lower transport through the Agulhas Current reflects a more southwestward retroflection and more Agulhas leakage (van Sebille et al., 2009). Eddy activity in the BMC shifts south while the strength of the Malvinas Current decreases and Southern Hemisphere westerlies shift south. Other results can generally be reinforced by anticipated anthropogenic impacts on ocean circulation. Decreasing EKE in the North Atlantic occurs concurrently with the widely anticipated decline of AMOC (Bakker et al., 2016; Caesar et al., 2018; Weijer et al., 2020). Substantial growth of Kuroshio EKE occurs in conjunction with an anticipated strengthening of Kuroshio volume transport (Chen et al., 2019; Zhang et al., 2017, 2020). Increased EKE in the southeastern Atlantic reflects greater Agulhas leakage, which is anticipated in a warming world based on palaeoclimatic and modeled evidence (Backeberg et al., 2012; Biastoch et al., 2009; Peeters et al., 2004; Rouault et al., 2009). Intensification of BMC EKE reflects a shift of thermohaline circulation in the Atlantic towards a southern route, consistent with model and palaeoclimatic evidence (Arz et al., 1999; Chiessi et al., 2014; Meier et al., 2021; Zhu & Liu, 2020). The representation of various anticipated impacts of anthropogenic climate change by modeled EKE suggests that EKE discerned from satellite data could be a useful proxy for large-scale climatic changes that is more conveniently observed than in situ monitoring of ocean velocities or overturning circulation.

2.6 Methods

2.6.1 Model configuration

In AWI-CM-1-1-MR, FESOM version 1.4 employs a finite-element numerical core with a 46-layer ocean mesh varying in horizontal resolution from approximately 8 km to 80 km (Semmler et al., 2020). FESOM's horizontal grid uses triangular cells of variable size rather than a traditional rectangular grid to vary grid resolution (Wang, Danilov, et al., 2014). The mesh used in these simulations was designed with particular consideration of observed sea surface height (SSH) variability as an indicator of dynamically active regions, and these regions are refined to sufficient resolution to simulate eddies based on the local Rossby radius of deformation (Sein et al., 2016, 2017). Thus, computational resources are allocated according to the observed presence of high local mesoscale activity, and resolution requirements for the simulation of mesoscale activity. While the design of the mesh is an attempt to make the best use of considerable

computational resources needed to carry out full CMIP6 experiments, the nominal ocean resolution of 25 km, or approximately 0.83 million ocean nodes, cannot produce eddy-rich conditions across the entire globe under any configuration. Rather, the mesh configuration (Supplementary Fig. A1) compromises on resolution in large areas of relatively low eddy activity, but by doing so, local grid refinements can exceed ½ of the local Rossby radius (R) along the paths of major ocean currents where high-eddy activity is observed. Importantly, ½ R is a crucial threshold below which eddy-resolving conditions can be reached (Hallberg, 2013), although the characteristics of the simulated eddies, such as size, speed or longevity, may still not reflect observations (Moreton et al., 2020), which could be a potential weakness in these simulations. Regions of high grid refinement are broader than observed regions of high SSH variability, to the extent that resources allow and steep resolution gradients are avoided; however, the potential for mesoscale activity to shift spatially beyond the refined grid regions remains a limitation of variable-resolution modeling. Outside of regions with sufficient resolution to simulate eddies, Gent–McWilliams eddy parameterization (Gent & McWilliams, 1990) is gradually introduced (Wang, Danilov, et al., 2014). Information regarding the configuration of the atmospheric component and coupling is in the Supplementary Notes.

2.6.2 Data

2.6.2.1 Model Data from AWI-CM-1-1-MR

This analysis considers a five-member ensemble of historical simulations and climate change projections (Semmler et al., 2018) under shared socio-economic pathway (SSP) 3–7.0 following the CMIP6 standards (Eyring et al., 2016). Spin-up information for the simulations is available in the Supplementary Notes. Emissions scenarios in CMIP6 are based on a matrix of SSPs (O'Neill et al., 2017) and representative concentration pathways (Moss et al., 2010). SSP3–7.0 describes a relatively high-emissions scenario in which CO2 levels are roughly doubled by the end of the century (Eyring et al., 2016; Masson-Delmotte et al., 2021; O'Neill et al., 2017). Other models from the CMIP6 ensemble were considered for inclusion in this analysis, as explained in the Supplementary Notes, but it was concluded that the variable-resolution capabilities of AWI-CM-1-1-MR make it uniquely suited to this study.

Geostrophic ocean surface velocities were calculated using daily SSH with (Eq. 2.1) and (Eq. 2.2).

(Eq. 2.1) $$u = -gf \frac{\partial SSH}{\partial y}$$

(Eq. 2.2) $$v = gf \frac{\partial SSH}{\partial x}$$

where u and v refer to zonal and meridional geostrophic velocities, respectively, where x and y are the longitudinal and latitudinal positions, respectively, where g is gravitational acceleration and f is the Coriolis parameter.

The use of daily SSH enables EKE to be calculated with a five-day mean temporal resolution, whereas only monthly mean ocean velocity data are available directly as model output. Moreover, the use of geostrophic velocities rather than direct model output allows for a more direct comparison with the altimetry dataset. More data processing steps are outlined in the Supplementary Notes. A visual representation of the velocity dataset (Fig. 2.1) demonstrates the effectiveness of the geostrophic velocity calculations and AWI-CM-1-1-MR in reproducing both overall surface flows and mesoscale activity. Supplementary Video A3 demonstrates this further through the animation of two sample years of velocity data.

To link EKE to other changes in the climate system, several additional variables were selected from model output and used to characterize the conditions surrounding simulated EKE change. Ocean velocity data (variables vo and uo) were used to calculate mean annual volume transport across chosen transects corresponding to currents that are hypothesized as physical drivers of EKE change (Supplementary Figs. A4, A5). Transects were selected based on the published literature and to approximate the locations of in situ measurements of volume transport (Supplementary Table A4). The simulated stream function of AMOC at approximately 26° N and 1,040 m depth was also computed (Supplementary Table A4). Surface wind speed (variable sfcWind) was averaged across lines of latitude to assess change in the magnitude of mean zonal surface winds (Supplementary Fig. A7).

2.6.2.2 Satellite altimetry observations

To assist in the evaluation of simulated EKE, gridded geostrophic velocity anomaly observations (variables ugosa and vgosa) between 1993 and 2020 from the Copernicus Marine Environment Monitoring Service and based on AVISO+ satellite altimetry were compared to the simulated data. The gridded observational data has a resolution of 0.25° by 0.25° and the equatorial band between 5° S and 5° N is replaced with approximated data (Lagerloef et al., 1999). The reference period used to compute anomalies in the altimetry dataset is 1993–2012. More information on processing of the altimetry dataset for this analysis can be found in the Supplementary Notes.

2.6.3 Eddy kinetic energy calculations

EKE can be defined as the energy contained by the time-varying component of ocean velocities, which are typically quantified as anomalies of ocean velocity. To account for potential changes in the mean state of ocean surface velocities in anomaly calculations, detailed in the Supplementary Notes, a running mean was removed from the raw data rather than a reference period mean. For each five-day period n in year j, a 21-year centered window of the same period n is considered from ten years prior, to ten years after year j. The ensemble mean of this window is then removed from the raw data to produce the anomaly as per equation (Eq. 2.3). This method effectively filters both low-frequency and seasonal variability from the velocity data and interprets the remaining variability as the anomalies representative of eddy activity. Finally, velocity anomalies were used to calculate EKE as per equation (Eq 2.4). The ensemble mean of 21-year running means from each ensemble member represents 105 data points of reference surface velocity data intended to represent the mean state of surface flow while losing only ten years of data at the beginning and end of each time series. Due to internal variability, the ensemble members may differ slightly in their simulation of mean flow, but these differences are expected to be smaller than those stemming from seasonality or the effects of climate change, making an ensemble mean preferable for characterizing mean flow.

(Eq. 2.3) $$u_{n,j}{}' = u_{n,j} - ENSavg(u_{\overline{n,j-10:j+10}})$$

(Eq. 2.4) $$EKE_{n,j} = \frac{1}{2}\left(u_{n,j}{}'^2 + v_{n,j}{}'^2\right)$$

where ENSavg() refers to the ensemble mean and prime (′) denotes an anomaly. For meridional velocity anomalies in equation (Eq. 2.3), replace u with v.

The long-term analysis of modeled EKE takes advantage of the length of the dataset and an ensemble of simulations to address the changing mean state of the global ocean due to anthropogenic climate change. To assess model fidelity, modeled data were compared to a shorter satellite altimetry dataset (1993–2020). For this comparison, anomalies of both datasets were calculated with respect to a 20-year reference period (1993–2012).

Time series of area-integrated EKE are produced by multiplying EKE by cell area and summing the results within selected basins (Supplementary Fig. A2). Basins were selected to encompass regions of high-eddy activity in the observed and modeled datasets both historically, and as it is projected at the end of the simulations, to capture spatial shifts. The resolution of the model grid was also considered when defining basins so that eddy-parameterizing regions are

not included. Direct comparison of EKE in different ocean basins should be avoided, as lower (higher) area-integrated EKE may represent greater (lesser) eddy activity in a smaller (larger) area. This, along with the general underrepresentation of EKE compared with observations due to grid resolution, prompts the use of standardized EKE values based on mean and standard deviation of EKE during the observational period (Eq. 2.5). This representation of EKE conveys change relative to conditions during the observed period (1993–2020) for each ensemble member and the observations respectively.

(Eq. 2.5) $$EKE_{i\ (standardized)} = \frac{(EKE_i - \overline{EKE})}{\sigma_{EKE}}$$

where i refers to a five-day mean time step, σ refers to the linearly detrended standard deviation during the observational period (1993–2020) and $\overline{EKE}$ refers to mean EKE during the observational period (1993–2020).

2.6.4 Characterization of change

Change in EKE within the observational record is typically assessed using linear trends (Ding et al., 2018; Hogg et al., 2015; Martínez-Moreno et al., 2021). However, in the context of longer modeled datasets, the observational record becomes a mere snapshot of larger regimes of change, demonstrating the constraints of observation-based studies. The comprehensive modeled dataset is used to address several of these constraints. To account for the uncertainty regarding future GHG emissions and climate change mitigation, EKE trends are reported relative to MGST rise relative to a 1850–1899 mean, facilitating comparison with other emissions scenarios and grounding projections of future change in a more physical basis than temporal trends. To distinguish a robust climate change signal from natural variability, least-square linear trends relating EKE to MGST rise are calculated using data after the ensemble mean of an 11-year running mean of MGST anomalies surpasses a threshold of 1 °K (Fig. 2.4). The spatial distribution of EKE change over time is quantified by subtracting historical EKE conditions (1860–1949) from conditions at the end of the century (2061–2090; Fig. 2.2c), capturing a period of approximately 3.3 °K of warming, and the statistical significance of change was confirmed using a t-test (not shown). Together, these metrics should provide a reasonably comprehensive assessment of EKE change in the context of anthropogenic climate change.

Large-scale climatic conditions including volume transport, AMOC and southern hemisphere westerlies are reported to assist with the interpretation of EKE change relative to the broader effects of anthropogenic climate change. The probability density distributions of

mean annual volume transport across selected transects and AMOC are reported for historical (1860–1949) and end-of-century projected (2061–2090) periods, along with the absolute and percentage changes (Supplementary Fig. A4, Supplementary Table A4). Time series of the same volume transport and AMOC data are reported in Supplementary Figure A5, and change in zonal mean surface wind speed between the same historical and projected periods is reported in Supplementary Figure A7. Simple linear regression is used to assess the relationship between volume transport and EKE where relationships are expected based on the published literature (Supplementary Fig. A6). Regression analysis is applied to unfiltered volume transport, AMOC and EKE data and low-pass-filtered data with a threshold of ten years to better identify relationships within high sub-decadal variability. The filtering was performed by applying Fourier transformations to the time series of each ensemble member, removing frequency signals greater than the 1/10 Hz threshold, applying an inverse Fourier transformation and discarding imaginary components.

3

Exploring the ocean mesoscale at reduced computational cost with FESOM 2.5: efficient modeling strategies applied to the Southern Ocean

This chapter is published under the same title in *Geoscientific Model Development* (Beech et al., 2024).

3.1 Abstract

Modeled projections of climate change typically do not include a well-resolved ocean mesoscale due to the high computational cost of running high-resolution models for long time periods. This challenge is addressed using efficiency-maximizing modeling strategies applied to 3 km simulations of the Southern Ocean in past, present, and future climates. The model setup exploits reduced-resolution spin-up and transient simulations to initialize a regionally refined, high-resolution ocean model during short time periods. The results are compared with satellite altimetry data and more traditional eddy-present simulations and evaluated based on their ability to reproduce observed mesoscale activity and to reveal a response to climate change distinct from natural variability. The high-resolution simulations reproduce the observed magnitude of Southern Ocean eddy kinetic energy (EKE) well, but differences remain in local magnitudes and the distribution of EKE. The coarser, eddy-permitting ensemble simulates a similar pattern of EKE but underrepresents observed levels by 55%. At approximately 1 °C of warming, the high-resolution simulations produce no change in overall EKE, in contrast to full ensemble agreement regarding EKE rise within the eddy-permitting simulations. At approximately 4 °C of warming, both datasets produce consistent levels of EKE rise in relative terms, although not absolute magnitudes, as well as an increase in EKE variability. Simulated EKE

rise is concentrated where flow interacts with bathymetric features in regions already known to be eddy-rich. Regional EKE change in the high-resolution simulations is consistent with changes seen in at least four of five eddy-permitting ensemble members at 1 °C of warming and all ensemble members at 4 °C. However, substantial noise would make these changes difficult to distinguish from natural variability without an ensemble.

3.2 Introduction

Mesoscale activity in the Southern Ocean has been the subject of much research and interest in recent years due to the intensification of Southern Hemisphere westerlies (Marshall, 2003), the phenomena of eddy saturation and compensation (Bishop et al., 2016; Munday et al., 2013), and the potential for carbon sequestration in the face of ongoing anthropogenic emissions (Frölicher et al., 2015; Landschützer et al., 2015; Sallée et al., 2012). Satellite observations already reveal an intensification of eddy activity in the Antarctic Circumpolar Current (ACC), and changes are attributed primarily to wind stress (Hogg et al., 2015; Marshall, 2003; Martínez-Moreno et al., 2021). Modeling studies have been able to reproduce the observed changes, as well as project continued intensification throughout the 21st century (Beech et al., 2022), but the modeled results rely on only partially resolved eddy activity relative to observations, leaving open the possibility for new findings or greater clarity.

Advances in computational capabilities have enabled ocean modeling science to make great progress in overcoming the substantial computational burden of simulating the mesoscale. However, shortcomings remain, particularly in the Southern Ocean where the Rossby radius can be as small as 1 km, increasing the computational cost of resolving eddies (Hallberg, 2013). Even model resolutions that can generally be considered eddy-resolving are only eddy-permitting poleward of 50° if grid spacing does not vary in space (Hewitt et al., 2020). This highlights an efficiency challenge in simulating the mesoscale with traditional model grids; resolutions necessary to resolve high-latitude, small-radius eddies are both prohibitively expensive and unnecessary to resolve mesoscale eddies in the lower latitudes. Fortunately, a growing number of modeling alternatives to traditional grids now enable dynamic spatial allocation of resources (Danilov, 2013; Danilov et al., 2017; Jungclaus et al., 2022; Ringler et al., 2013), creating the opportunity to more efficiently resolve the mesoscale.

As resource allocation in high-resolution modeling becomes spatially flexible in the pursuit of more efficient configurations, the temporal component must also be scrutinized for efficiency. Traditional modeling approaches require long spin-up periods in order to equilibrate

the deep ocean and reduce model drift (Irving et al., 2021). Although the impacts of drift are not negligible, they generally affect large-scale processes in the deep ocean; mesoscale processes that require high resolutions to simulate are typically fast to equilibrate and will appear relatively quickly wherever large-scale ocean conditions lead to their creation. Admittedly, one cannot entirely disentangle the two scales, as mesoscale activity does affect the position of fronts, stratification, and the paths of ocean circulation (Chassignet & Xu, 2017; Marshall, 2003; Marzocchi et al., 2015). Yet, with equilibration times for the deep ocean on the scale of thousands of years (Irving et al., 2021), the possibility, and ultimately necessity, to reduce the resolution of spin-up runs relative to production runs must be investigated.

Advancing the concept of dynamic temporal allocation of resources further, the traditional transient climate change simulation also represents an efficiency bottleneck for some applications; by modifying the climate continuously in time, each year of a transient simulation is effectively a single realization of a global mean climatic state that varies from the following and preceding years by only a fraction of a degree. For some applications, like hindcasts of real events or trend analysis, this approach may be desirable, but for assessing the impacts of climate change with limited resources and a low signal-to-noise ratio, a larger sample of realizations for a consistent climatic state may be more suitable.

Aside from oceanic concerns, the atmosphere can have substantial impacts on mesoscale activity in climate models. Most simply, with a coupled atmosphere, absolute surface winds will react to ocean eddy activity, whereas atmospheric forcing will not, resulting in more eddy killing by wind stress (Renault et al., 2016). Additionally, an atmosphere coupled to a high-resolution ocean must be of similarly high resolution for certain mesoscale interactions to be resolved (Byrne et al., 2016). Ultimately, the modeled atmosphere further escalates the already exponential cost of increasing ocean resolution by requiring more computational resources in order for the benefits of the resolved mesoscale to fully transfer to the broader climate.

To address the computational inefficiencies outlined above, a novel simulation configuration is proposed, combining several experimental modeling approaches. Simulations will exploit the multi-resolution Finite volumE Sea-ice Ocean Model (FESOM) (Danilov et al., 2017) employing a high-resolution unstructured mesh that concentrates computational resources on the Southern Ocean while maintaining grid resolution in the remainder of the global ocean that can still be considered high resolution, as in, for example, HighResMIP (Haarsma et al., 2016). The multi-resolution strategy overcomes the efficiency challenges of resolving high-

latitude eddies without needlessly increasing tropical resolutions, as well as limiting the focus and computational requirements to one hemisphere. The high-resolution simulations will make use of a spin-up simulation on a medium-resolution, eddy-permitting mesh to avoid the computational burden of allowing an eddy-resolving ocean to equilibrate deep, slow-changing processes. The eddy-permitting mesh will also be used to simulate the transient periods between shorter, high-resolution time slices, increasing the signal-to-noise ratio of the results by separating the production data further in time and the progression of anthropogenic climate change. Finally, the ocean model will be forced with atmospheric data from existing coupled simulations (Semmler et al., 2020). Although this will not facilitate mesoscale atmosphere–ocean interaction, the simulation will reflect the climatic development of an eddy-permitting simulation of the future atmosphere without the additional computational requirements.

The Southern Ocean is one of the world's hotspots for mesoscale activity and a region where substantial change is anticipated in the context of anthropogenic climate change (Beech et al., 2022). Simultaneously, the high latitude of the region makes eddy-resolving model simulations computationally demanding and observational data relatively scarce (Auger et al., 2023; Hallberg, 2013). Yet, as the climate changes, the importance of the Southern Ocean grows as a heat and carbon sink, an ecosystem, and a medium for feedback between the atmosphere and ocean (Byrne et al., 2016; Frölicher et al., 2015). Thus, the study of the Southern Ocean demands innovation in the modeling field to produce high-resolution simulations at reduced computational cost. This study maximizes grid resolution relative to computational cost using an unstructured, multi-resolution grid, a medium-resolution spin-up simulation, and atmospheric forcing from lower-resolution coupled simulations in order to focus resources as much as possible on resolving mesoscale activity in the study region. The resulting simulations enable an exploratory analysis of the past, present, and future of the Southern Ocean with a fully resolved mesoscale. Simulations with this cost-efficient, high-resolution configuration are presented in comparison to a comprehensive ensemble of eddy-permitting simulations to assess the performance of the efficiency-focused approach in reproducing mesoscale activity and its response to climate change.

3.2 Methods

3.2.1 Experimental setup

This analysis contrasts a subset of simulations from AWI-CM-1-1-MR's contribution to the sixth phase of the Coupled Model Intercomparison Project (CMIP6; Semmler et al., 2020)

(hereafter referred to as the AWI-CM-1 ensemble), with single-member standalone ocean simulations using an updated version of FESOM (FESOM 2.5) and a mesh substantially refined to a resolution surpassing 3 km in the Southern Ocean (hereafter referred to as the SO3 simulations; Supplementary Fig. B1). Observations of ocean surface velocity derived from satellite altimetry data are also used to evaluate model performance for both modeled datasets during the period of overlap with the altimetry record. The AWI-CM-1 simulations consist of the five-member ensemble of historical simulations and the five-member ensemble of climate change projections under shared socioeconomic pathway (SSP) 3-7.0 which were performed by AWI-CM-1-1-MR in CMIP6 (Semmler et al., 2020). These are state-of-the-art CMIP6 experiments and benefit from the multiple ensemble members and long spin-up times that CMIP simulations typically boast. However, while the AWI-CM-1 ensemble reproduces eddy activity remarkably well within the context of CMIP6 (Beech et al., 2022), high-resolution ocean modeling now far surpasses even the highest ocean resolutions in the CMIP6 ensemble. Conversely, the SO3 simulations push the limits of ocean resolution but rely on several measures for maximizing computational efficiency that may impact the robustness of the simulations. Details on the experimental setup for CMIP6 and ScenarioMIP are widely available (Eyring et al., 2016; O'Neill et al., 2017), and information more specific to AWI-CM-1-1-MR's contribution has been published previously (Semmler et al., 2020). The following sections will outline the details of the SO3 simulations.

To produce initial conditions for the high-resolution model simulations on the SO3 mesh, a medium-resolution, eddy-permitting, ocean-only transient simulation was first run from 1851 to 2100 using the same ocean mesh employed by AWI-CM-1-1-MR in CMIP6 (Semmler et al., 2020). This mesh has been shown to effectively reproduce eddy activity in active regions while maintaining a computational cost comparable to a traditional 1/4° model (Beech et al., 2022). The transient simulation was initialized with conditions for ocean temperature and salinity, as well as sea ice concentration, thickness, and snow cover taken from the end of the first year (1850) and first ensemble member (r1i1p1f1) of AWI-CM-1-1-MR's historical simulations in CMIP6 (Semmler et al., 2018, 2020, 2022a, 2022b). In this way, the model undergoes a semi-cold start in which ocean conditions are not exact continuations of the previous coupled simulation but should be far closer to equilibrium than a true cold start initialization. The eddy-permitting transient simulation was forced using atmospheric data from the same ensemble member of the historical CMIP6 simulations until 2014 (Semmler et al., 2022a) and thereafter using the first ensemble member of AWI-CM-1-1-MR's ScenarioMIP simulations for SSP 3-7.0 (Eyring et al., 2016; O'Neill et al., 2017; Semmler et al., 2022b). This approach to forcing takes advantage of a

coupled simulation, CMIP6, to produce a forcing dataset of better temporal and spatial coverage than the observational record and which maintains a realistic transient climate throughout anthropogenic impacts during the 21st century.

In the years 1950, 2015, and 2090, FESOM is reinitialized with the high-resolution ocean grid, SO3 (Supplementary Fig. B1), using the same semi-cold start approach and forcing dataset that were implemented for the eddy-permitting transient simulation described previously. These years were chosen to represent a historical period, beginning in 1950, when the effects of climate change on EKE should be small or none (Beech et al., 2022); a near-present period, beginning in 2015, in which the simulations will overlap with satellite altimetry data; and a projected period, beginning in 2090, which should include a strong climate change signal. The latter two simulated periods represent 1.07 and 3.74 °C of warming, respectively, in the first ensemble member of the AWI-CM-1 ensemble defined as a rise in the 21-year running mean of global mean 2 m air temperatures. Warming of the ensemble mean is similar: 1.08 and 3.76 °C, respectively, and warming is henceforth approximated as 1 and 4 °C in Figure 3.4 and the text. Initial conditions for these shorter time-slice simulations are taken from the end of the previous year of the eddy-permitting transient simulation. The high-resolution simulations are each integrated for 6 years with the first year ignored as a true spin-up, leaving 5 years of data for each time period. The high-resolution grid is, in truth, a regionally refined mesh in which a 25 km global resolution is refined to approximately 2.5 km, following (Danilov, 2022), primarily south of 40 °S, but with other pertinent regions, such as the Agulhas Current and several narrow straits, also refined. In this way, the model is able to simultaneously achieve eddy-rich conditions in the Southern Ocean and many of the nearby active regions, as well as a global resolution that would still be considered high in the context of CMIP6 (Hallberg, 2013; Hewitt et al., 2020). While model drift may be a concern with such a short true spin-up period, this should affect each of the high-resolution time slices similarly and to a limited extent due to their short integration lengths. Thus, the differences between the high-resolution ocean simulations should primarily reflect anthropogenic climate impacts simulated during the eddy-permitting transient run and present in the forcing dataset.

3.2.2 Model configuration

The Finite volume Sea-ice Ocean Model version 2.5 is a post-CMIP6 era model, having been refactored to a finite-volume configuration from the finite-element version (FESOM 1.4; Wang, Danilov, et al., 2014) employed in CMIP6 and transitioned to arbitrary Lagrangian–Eulerian vertical coordinates, among other improvements (Danilov et al., 2017; Scholz et al.,

2019, 2022). FESOM's most distinguishing feature among mature ocean models is the unstructured horizontal grid that exploits triangular grid cells which can smoothly vary in size to change the horizontal grid resolution in space. In these simulations, full free surface, or z∗, vertical coordinates were used, allowing the vertical model layer thicknesses to change in time. Gent–McWilliams eddy parameterization (Gent & McWilliams, 1990) is scaled with resolution according to (Ferrari et al., 2010), and vertical mixing is simulated by a k-profile parameterization scheme (Large et al., 1994).

The SO3 mesh consists of over 22 million surface elements (triangle faces) or 11 million surface nodes (triangle vertices) and 70 vertical layers. The simulations produce about 1.1 terabytes of data per simulated year of 3D daily data stored on nodes. For reference, the medium-resolution mesh used in the AWI-CM-1 ensemble is 1.6 million surface elements or 0.83 million surface nodes and 46 vertical layers and produces approximately 56 GB per simulated year of 3D daily data stored on nodes. The model was run on 8192 CPU cores with a typical throughput of approximately 0.65 simulated years per day, consuming approximately 5.5 million CPU hours in total despite the various cost-saving modeling approaches. It should be noted, however, that the throughput in high-resolution production simulations like this is highly dependent on the volume and choice of data being saved. The simulations and following analyses were performed using the high-performance computing system, Levante, at the German Climate Computing Center (DKRZ).

The ocean model is forced by several atmospheric variables at a 6 h resolution, although one forcing variable, humidity, is interpolated monthly data. The forcing data are supplied to the model on the regular atmospheric grid used in the coupled setup during AWI-CM-1-1-MR's CMIP6 simulations (Semmler et al., 2018) and interpolated to the multiresolution grid used in the respective simulations by FESOM. Runoff data are a monthly climatology, and dynamic ice sheet coupling is not included, meaning the freshwater influx from the Antarctic continent does not react to warming, which may impact certain processes, such as the timing and intensity of sea ice loss (Bronselaer et al., 2018; Pauling et al., 2017).

3.2.3 Modeled ocean velocity data

Geostrophic balance is an idealized approximation that does not match real ocean velocities for several reasons, including the presence of ageostrophic flow, such as Ekman transport, as well as assumptions made in the derivation of (Eq. 3.1) and (Eq. 3.2). Specifically, geostrophic balance between the Coriolis effect and the pressure gradient is valid under the assumption that the curl of horizontal velocities or vorticity is small relative to the magnitude of

overall flow. In models, this assumption is relatively close to reality in coarse-resolution simulations where geostrophic flow dominates, but on higher-resolution meshes, where submesoscale flows are well-resolved, these omitted terms become larger. Therefore, while using geostrophic velocities for both high-resolution and coarse-resolution modeled datasets would be methodologically consistent, the error introduced would be systemically larger for the finer-resolution dataset than the coarser. Therefore, we do not consider the use of geostrophic velocities for both modeled datasets in this analysis to bring the data into closer agreement. Rather, for the AWI-CM-1 dataset, where daily ocean velocities were not saved (Semmler et al., 2018), geostrophic velocities derived from sea surface height with (Eq. 3.1) and (Eq. 3.2) are the best possible choice, and fortunately, as described earlier, the error introduced by the assumptions of geostrophic balance will be small. For the SO3 simulations, direct model output was saved and is preferred, particularly given the high resolution of the mesh.

(Eq. 3.1) $$u = -gf \frac{\partial SSH}{\partial y}$$

(Eq. 3.2) $$v = gf \frac{\partial SSH}{\partial x}$$

where u and v refer to zonal and meridional geostrophic velocities, respectively, where x and y are the longitudinal and latitudinal positions, respectively, where g is gravitational acceleration and f is the Coriolis parameter.

The omission of Ekman transport, the primary source of ageostrophic oceanic flow from atmospheric influences, can be relatively well addressed in the SO3 dataset by selecting modeled velocities just below the Ekman layer. At depths of 25–30 m below sea level, the bulk of Ekman transport can be avoided (Price et al., 1987), while velocities should not substantially differ from those at the surface. What ageostrophic flow remains in the model output velocities should be primarily large scale and small relative to geostrophic flow in the high-energy regions of the ocean, including the ACC (Yu et al., 2021).

3.2.4 Altimetry data

An observational data product of gridded, daily geostrophic velocities derived from along-track satellite altimetry from crossover data is taken from the Data Unification and Altimeter Combination System (DUACS) (Taburet et al., 2019). The gridded product has a resolution of 0.25°, although effective resolution at high latitudes may be much lower (Ballarotta et al., 2019). Recently, improved data have become available in the ice-covered regions of the Southern Ocean (Auger et al., 2022) but do not yet cover the full present-day simulated period (2016–2020) in

this study. Absolute velocities from the gridded altimetry product were used to calculate anomalies and EKE using (Eq. 3.3) and (Eq. 3.4) below for consistency with the modeled dataset.

3.2.5 EKE analysis

Velocity anomalies are defined by subtracting the multi-year monthly climatology of each respective 5-year period from daily velocities with (Eq. 3.3).

(Eq. 3.3) $$u'_i = u_i - u_m$$

where u_i is the daily zonal velocity, $'$ denotes an anomaly, and u_m is a monthly mean. For meridional velocities (v) substitute u with v.

Eddy kinetic energy is calculated from ocean velocities according to (Eq. 3.4).

(Eq. 3.4) $$EKE_i = 0.5\,(\,{u'_i}^2 + {v'_i}^2\,)$$

where i denotes a daily value and $'$ denotes an anomaly.

EKE was calculated on the native grid of each dataset and then interpolated to a 0.25° grid for all analyses. In Figures 3.1 and 3.3, EKE was first calculated on a daily timescale and coarsened to 5-day means before analysis to reduce computational costs during post-processing. Area-integrated EKE (Figs. 3.1, 3.3) is calculated by summing the area-weighted EKE of each grid cell in the study region defined as the zonal band between 45 and 65 °S. The Brazil–Malvinas confluence region between 57 and 29 °E and northward of 40° S is removed to focus the study on a region with consistent physical drivers theorized to be responsible for the changes in eddy activity (Beech et al., 2022). As a precaution, each dataset was linearly detrended before analysis in Figures 3.1 and 3.3 to avoid artificially increasing the range of the later distributions due to the accelerating climate change signal. Select statistical properties are reported in Supplementary Tables B1, B3 to indicate deviations from normality (D'Agostino & Belanger, 1990; Fisher, 1997) and autocorrelation (Durbin & Watson, 1950). Rather than attempt to manipulate the data to meet certain statistical assumptions, complex statistical tests are avoided and the statistical properties reported can be used to interpret the EKE data in a physical sense. EKE anomalies (Fig. 3.1) were calculated by subtracting the 2016–2020 mean of area-integrated EKE from the 5-day mean values of each period. Normalized EKE was calculated by further dividing EKE anomalies by the standard deviation of EKE during the 2016–2020 period. In Figure 3.4, ensemble agreement is determined by ordering the EKE values within each grid cell from lowest to highest,

plotting the positive values in increasing order from left to right and negative values in decreasing order from left to right.

3.3 Results

3.3.1 Agreement with observations

During the 5-year period of overlap with observations, the SO3 simulation is a drastic improvement on the AWI-CM-1 ensemble in reproducing median observed EKE (Fig. 3.1a,c, note the different y axes); only a slight underrepresentation of EKE remains in the SO3 simulation, although the simulated distribution is somewhat distinct from observations. In comparison, the AWI-CM-1 ensemble, being effectively eddy-permitting in the Southern Ocean, underrepresents observations by approximately 55% (Fig. 3.1a,c, note the different y axes). EKE in SO3 appears more variable than the observations considering its larger range (Fig. 3.1c,e), and in general, the modeled datasets display greater deviations from a normal distribution than the observations (Fig. 3.1a,b,c; Supplementary Table B2). Nonetheless, relative to the AWI-CM-1 model bias and the magnitude of resolved EKE, the ensemble spread within the AWI-CM-1 dataset is small (Fig. 3.3), suggesting that a single ensemble member of 5 years' duration is sufficient to assess how well a model captures the magnitude of overall Southern Ocean EKE (Fig. 3.1c).

From a regional perspective, the SO3 simulation accurately reflects local magnitudes of observed EKE and also generally captures the spatial distribution well (Fig. 3.2). However, there are regional shortcomings, such as between 90 and 145 °E. Grid resolution in this region should be sufficient to resolve eddy activity (Supplementary Fig. B1), indicating that the bias arises from another source. In the AWI-CM-1 ensemble, the regional representation of EKE reinforces a broad underrepresentation relative to observed magnitudes, but the major geographic features of eddy activity are fairly well represented (Fig. 3.2). Once again, the ensemble spread within the AWI-CM-1 simulations reveals remarkable consistency, this time in terms of the spatial pattern and regional magnitudes (Supplementary Fig. B2), reinforcing the conclusion that a single ensemble member of 5 years' duration is sufficient to assess the mean state of EKE in the Southern Ocean. The consistency of the AWI-CM-1 ensemble further suggests that regional shortcomings in eddy activity in the SO3 simulations are not a product of variability within a single realization of Southern Ocean conditions (Supplementary Fig. B2).

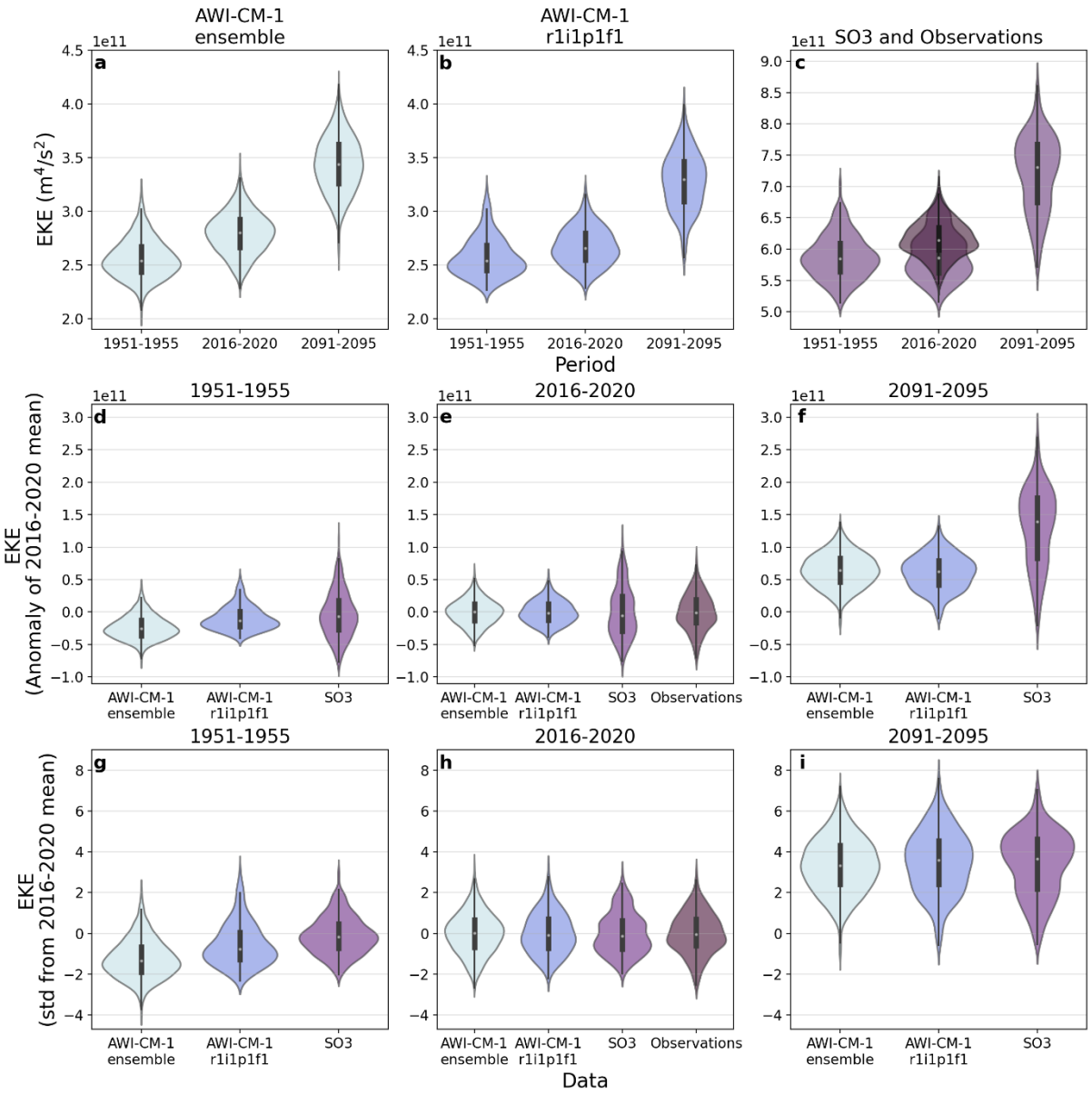

Figure 3.1. Violin plots of area-integrated Southern Ocean EKE in simulations and observations. Central points of each plot indicate the median, thick bars span the first and third quartiles, thin bars span the range, and the violin body is a kernel density estimation of the data. **(a–c)** Magnitudes of area-integrated EKE (note the different y axes). **(a)** The AWI-CM-1 ensemble. **(b)** The first member of the AWI-CM-1 ensemble, from which the SO3 simulations take their atmospheric forcing. **(c)** The SO3 simulations and observations. **(d–f)** Anomalies relative to the 2016–2020 mean of area-integrated EKE for each dataset: **(d)** 1951–1955, **(e)** 2016–2020, and **(f)** 2091–2095. **(g–i)** Normalized values relative to the mean and standard deviation of EKE during the 2016–2020 period for each dataset: **(g)** 1951–1955, **(h)** 2016–2020, and **(i)** 2091–2095.

3.3.2 EKE change and significance

Southern Ocean eddy activity has been shown to have intensified over the recent decades using both satellite altimetry (Martínez-Moreno et al., 2021) and the complete AWI-CM-1-1 dataset from CMIP6 (Beech et al., 2022). Even after reducing the AWI-CM-1 CMIP6 dataset to 5-year periods preceding the apparent change (1951–1955) and at the end of the altimetry era (2016–2020), this intensification is still discernable within the AWI-CM-1 ensemble (Fig. 3.1a). Despite his, the SO3 simulations do not demonstrate any substantial change in EKE magnitude over the same period (Fig. 3.1). Further reducing the ensemble to its individual members (Fig. 3.3), the EKE rise is still relatively robust in each case, including clear separation of the datasets considering the median, mode, and distribution of the data. However, the first ensemble member, from which the atmospheric forcing of SO3 is taken, demonstrates less EKE rise than the ensemble average (Fig. 3.3), suggesting that natural variability in atmospheric conditions may contribute to the disagreement. Further investigation reveals several differences between the SO3 simulations and the AWI-CM-1 ensemble members that may play a role. Mean zonal ocean velocity in SO3 is faster and broader than the AWI-CM-1 ensemble (Supplementary Fig. B3), meaning wind speed intensification may be misaligned with peak ocean velocities in SO3, particularly around 47 to 51 °S. Moreover, considerably less zonal wind stress is imparted to the ocean in SO3 despite identical wind speeds as the first AWI-CM-1 ensemble member (Supplementary Fig. B4), possibly due to the higher ocean surface velocity.

The intensification of EKE becomes clear in both the AWI-CM-1 ensemble (Fig. 3.1a), its members (Fig. 3.3), and the SO3 simulations (Fig. 3.1c) by the end of the 21st century. Over this period, the variability in EKE, indicated by the range of the distribution, also increases for each dataset (Fig. 3.1f,i). EKE rise in SO3 is approximately twice that of the AWI-CM-1 ensemble in absolute terms (Fig. 3.1f), but expressing EKE as a relative value normalized by the mean and standard deviation of each dataset during the observational period (Fig. 3.1g,h,i) reveals greater consistency between the changes until the end of the 21st century. EKE in each dataset appears to increase by approximately 3.5 standard deviations, and the range of EKE distributions increases by approximately 2 to 3 standard deviations (Fig. 3.1h,i). However, the datasets also tend to become more autocorrelated, which can inflate the distribution range (Supplementary Tables B1, B3).

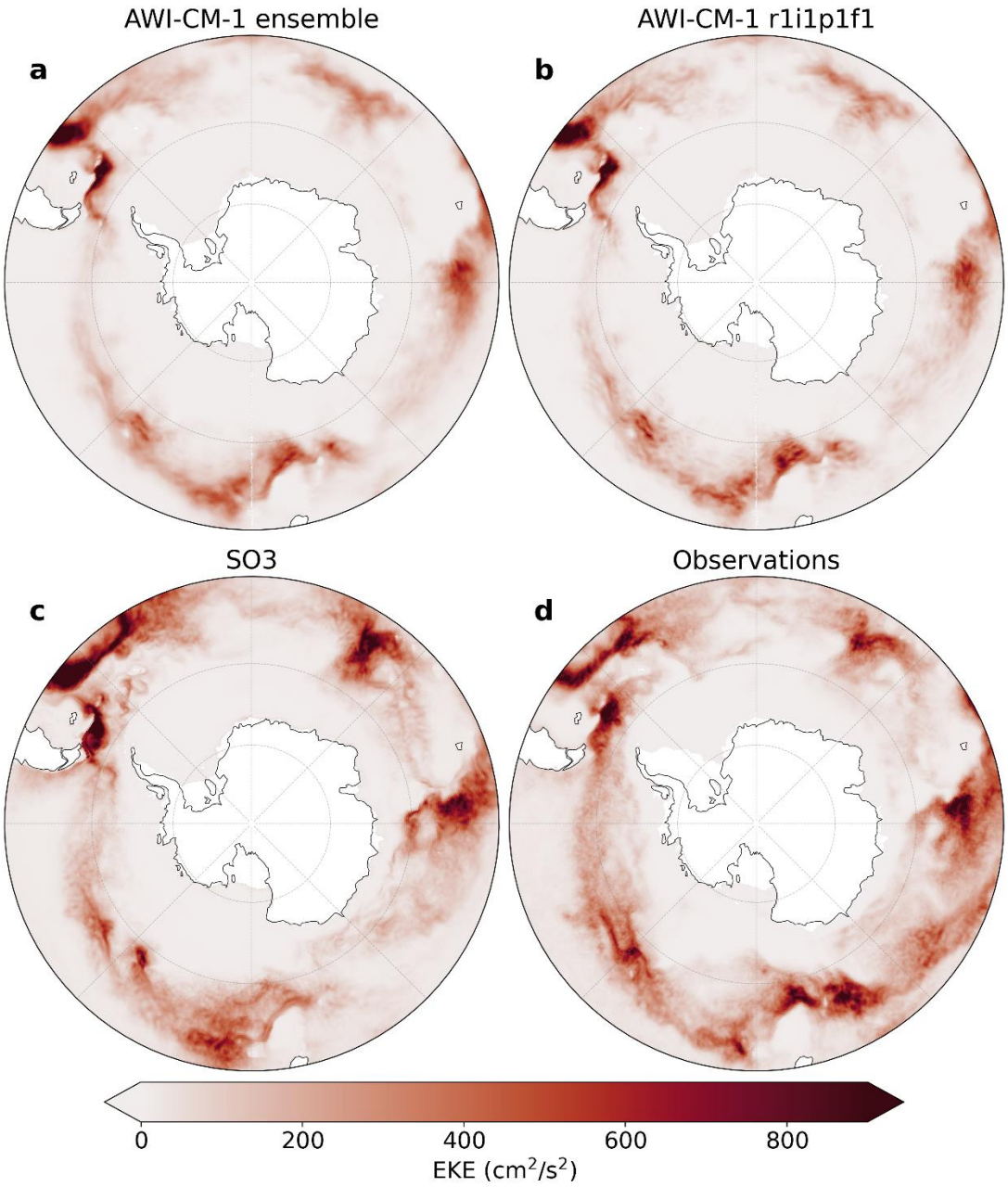

Figure 3.2. Mean eddy kinetic energy between 2016 and 2020. (a) The AWI-CM-1 ensemble. **(b)** The first member of the AWI-CM-1 ensemble. **(c)** The SO3 simulation. **(d)** The gridded satellite altimetry dataset.

Before considering the regional impacts of warming on EKE in the SO3 simulations, it is useful to refer to the ensemble spread within the AWI-CM-1 simulations to approximate the reliability of a single ensemble member in revealing the ensemble-mean change as an analogue to the signal-to-noise ratio. At 1 °C of warming, EKE change in the ensemble is weak, with at least one ensemble member tending to show little or no EKE change in most regions (Fig. 3.4a,c). Only

a few clear patterns of change emerge throughout the ensemble, namely the regions of EKE intensification downstream of the Kerguelen Plateau and the Campbell Plateau, where four to five out of five ensemble members show clear EKE intensification (Fig. 3.4a). It should be noted that even in these regions of relatively high confidence (four to five ensemble members, Fig. 3.4a) EKE rise can be interspersed with lower-confidence (one to two ensemble members, Fig. 3.4c) EKE decline; this is also illustrated by the ensemble mean changes themselves (Supplementary Figs. B5, B6). Despite this, the consistency of EKE rise in these regions, as well as their geographic positions in already EKE-rich regions, suggests that the intensification patterns are robust changes within substantial noise. This level of noise suggests that EKE changes in the SO3 simulations at 1 °C of warming will be difficult to distinguish from natural variability when taken on their own; indeed, in the SO3 simulations, the large variability in both sign and magnitude of change within relatively small spatial scales does not lend confidence to any significant change at 1 °C of warming (Fig. 3.5c). However, building on the changes observed in the AWI-CM-1 ensemble, the intensification of EKE downstream of the Kerguelen and Campbell plateaus seems to be reinforced by the high-resolution simulations.

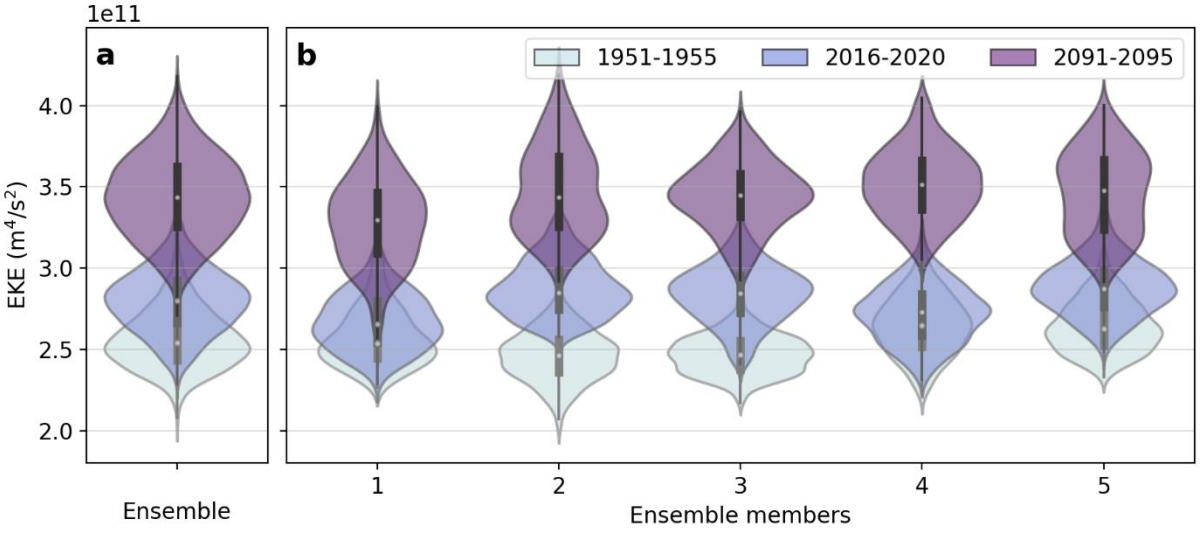

Figure 3.3. Ensemble spread of EKE in AWI-CM-1. (a) Violin plots of area-integrated Southern Ocean EKE in the AWI-CM-1 ensemble. **(b)** Violin plots of mean Southern Ocean EKE in each member of the AWI-CM-1 ensemble. Grey plots represent the period 1951–1955, blue plots represent 2016–2020, and purple plots represent 2091–2095.

At 4 °C of warming, the change in eddy activity becomes clearer; EKE intensification downstream of the Kerguelen and Campbell plateaus is now consistent throughout the entire AWI-CM-1 ensemble, along with additional intensifications south of the Falkland/Malvinas

Plateau, around the Conrad Rise, and along the Antarctic Slope Current at approximately 5° E (Fig. 3.4b). Four-fifths of the ensemble also include a broad increase in EKE throughout the ACC across most longitudes. Interestingly, a consistent pattern of EKE decline also emerges upstream of the Campbell Plateau in the entire ensemble (Fig. 3.4d). The spatial pattern of EKE rise is relatively consistent regardless of confidence, with only the magnitude increasing in the lower confidence composites (Fig. 3.4b). The same tendency is observable between the EKE changes at 1 and 4 °C of warming, where the magnitude of change is greater after further warming but follows the same spatial pattern. Thus, regions of intensification can be identified more reliably than the magnitude of change and tend to be concentrated where flow interacts with topographic features, in already eddy-rich regions (Fig. 3.2). Conversely, low-confidence EKE decline appears nearly throughout the Southern Ocean in at least one ensemble member but only consistently upstream of the Campbell Plateau and, to a far lesser extent, downstream of the Drake Passage and Campbell Plateau (Fig. 3.4d). Changes in negative sign tend to be of lower magnitude at 4 °C of warming than at 1 °C. This suggests that the general EKE response to climate change in the Southern Ocean is that of intensification, and the interspersed signals of decline tend to be the result of natural variability. Yet, small regions of high-confidence EKE decline also appear. Consequently, it would be difficult to confidently separate reliable EKE change from natural variability in simulations without an ensemble to compare with. In the SO3 simulations, EKE rise downstream of the Drake Passage and Kerguelen and Campbell plateaus is substantial (Fig. 3.5f). EKE rise is also projected south of the Falkland/Malvinas Plateau, around the Conrad Rise, and along the Antarctic Slope Current at approximately 5° E, and a slight EKE decline appears upstream of the Campbell Plateau. All of this is comparable to the AWI-CM-1 ensemble, and the interspersed areas of EKE decline within these regions, for example, around the Conrad Rise, are not improbable based on the example set by AWI-CM-1 (Fig. 3.4d). However, considering that some high-confidence EKE decline is present in the AWI-CM-1 ensemble, it is difficult to confidently dismiss regional EKE decline in the SO3 simulations as noise.

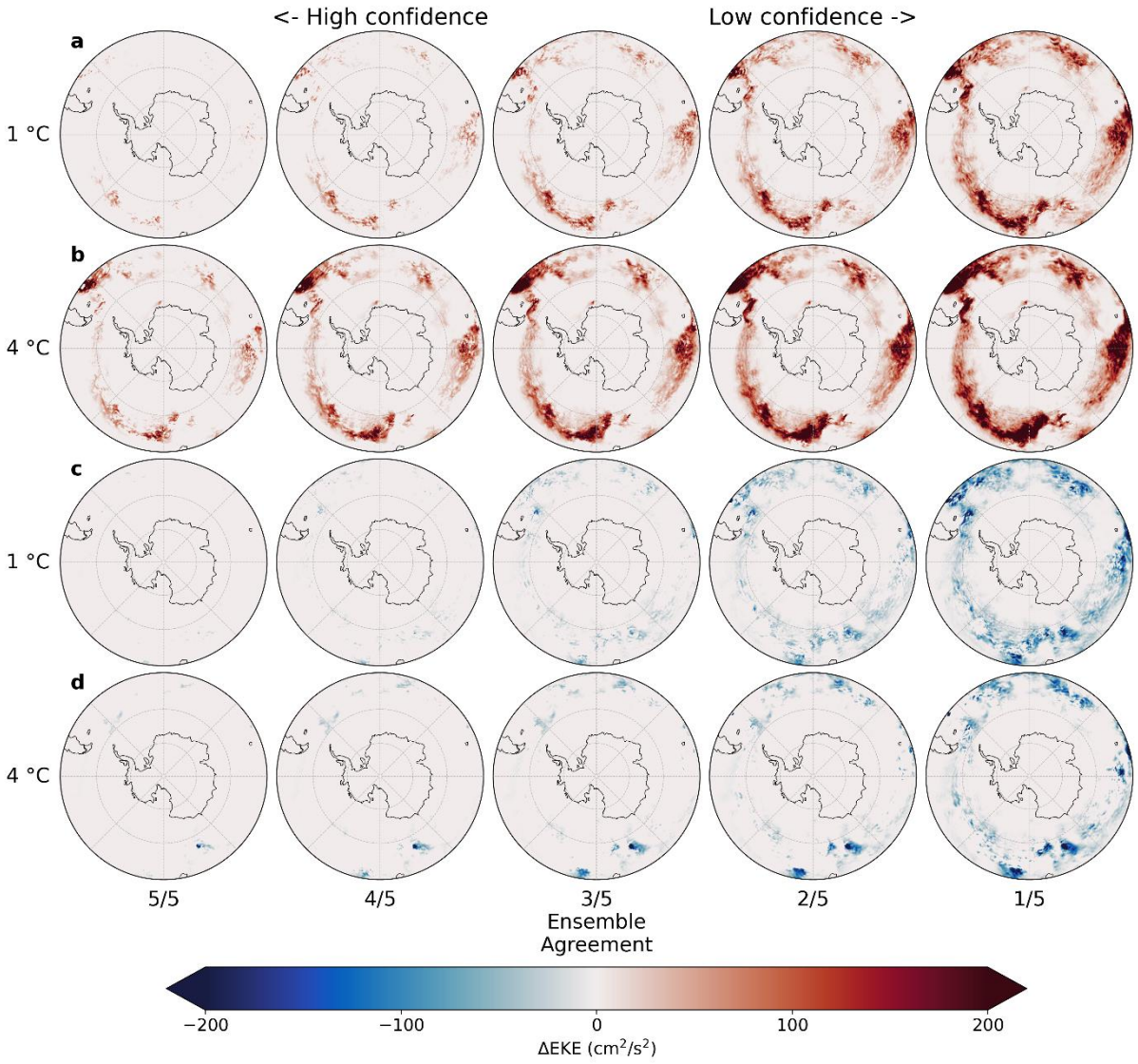

Figure 3.4. Ensemble agreement regarding EKE change. EKE rise **(a,b)** and decline **(c,d)** within the AWI-CM-1 ensemble after 1 **(a,c)** and 4 °C **(b,d)** of warming or between 1951–1955 and 2016–2020 and 2091–2095, respectively, arranged in order of decreasing ensemble agreement regarding change in each grid cell. Ensemble agreement refers to the number of ensemble members that simulate at least the pictured magnitude of mean EKE rise or decline for each grid cell. Mean EKE change is defined as the difference in mean EKE between 1951–1955 and each of the two latter periods, as in Supplementary Figures B5 and B6 but arranged in ascending order of magnitude for each grid cell and for positive and negative signs separately. Rank 5/5 indicates the lowest magnitude of mean EKE rise **(a,b)** or decline **(c,d)** within the ensemble for a given grid cell, meaning the entire ensemble agrees on at least this much change. Rank 1/5 indicates the highest magnitude of EKE rise or decline within the ensemble for each grid cell, representing the upper limit of projected EKE change.

3.4 Discussion

Intensification of eddy activity in the Southern Ocean is now widely accepted as a consequence of anthropogenic climate change (Beech et al., 2022; Hogg et al., 2015; Martínez-Moreno et al., 2021; Patara et al., 2016) and is understood to be caused primarily by stronger westerly winds imparting more energy to the Antarctic Circumpolar Current (Marshall, 2003; Munday et al., 2013). The results presented here reinforce the notion of EKE intensification and further project increased EKE variability as the climate warms (Figs. 3.1, 3.3). By expressing EKE change in terms of ensemble agreement on a cell-by-cell basis, the results presented here are also able to identify regions of reliable and substantial change as those where flow interacts with major bathymetric features and high eddy activity is already known to occur (Fig. 3.4). Analysis of regional changes within the Southern Ocean eddy field has generally been limited to regions defined by oceanic sectors (Atlantic, Indian, Pacific) (Hogg et al., 2015) or incremental longitudinal delimitations (Patara et al., 2016). In future research, regional analyses of the significance, rate, or cause of EKE trends could focus on the bathymetrically defined regions identified in this analysis to produce physically related and consistent results.

The consistency of the AWI-CM-1 ensemble in projecting clear EKE rise in the Southern Ocean as a whole suggests that a single ensemble member of 5-year simulation length should be sufficient to reliably identify change, even after 1 °C of temperature rise. Despite this, the SO3 simulations fail to reproduce the EKE rise that is already observable through observations (Martínez-Moreno et al., 2021). A potential source for this discrepancy is the uncoupled model setup in the SO3 simulations which omits ocean-atmosphere feedbacks. In this regard, the SO3 simulations experience lower wind stress imparted to the ocean surface than the AWI-CM-1 ensemble member one by the same surface winds (Supplementary Fig. B4), as well as a mismatch between peak zonal wind speeds and mean zonal ocean velocities (Fig. 3.3). Confounding the comparison further is the fact that strengthening winds can both increase and dampen eddy activity; as westerlies intensify, the additional energy imparted to the ocean is expected to strengthen eddy activity (Munday et al., 2013; Meredith and Hogg, 2006), but winds are also known to dampen mesoscale activity through eddy killing (Rai et al., 2021), and this impact is greater in uncoupled model configurations (Renault et al., 2016). While the lack of change at 1 °C is difficult to explain, the disagreement is limited to these more subtle changes, and the simulations tend to agree on the strong EKE rise at 4 °C of warming.

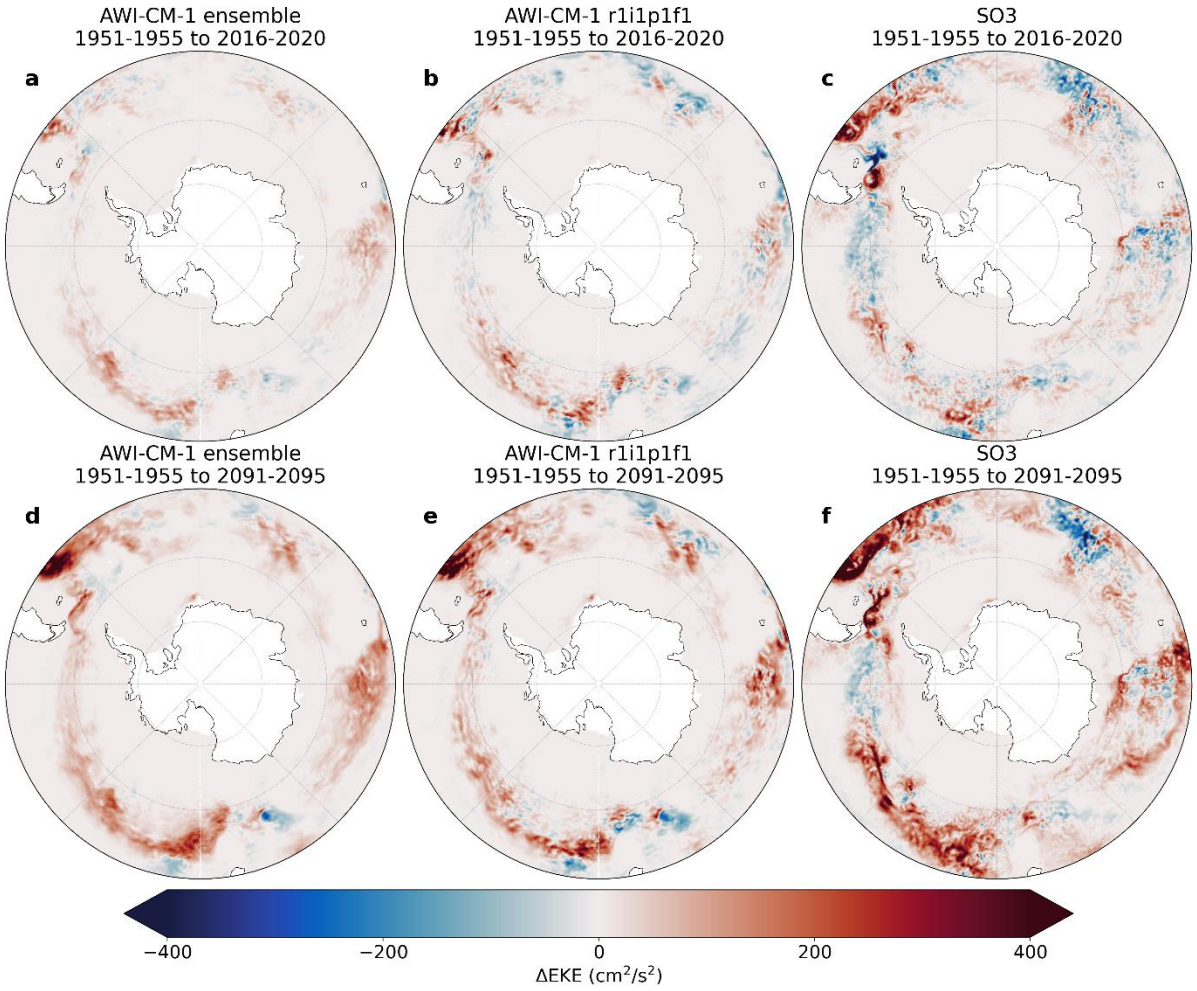

Figure 3.5. EKE change. Spatial representations of the difference in EKE between **(a–c)** 1951–1955 and 2016–2020 and **(d–f)** 1951–1955 and 2091–2095. **(a,d)** The AWI-CM-1 ensemble. **(b,e)** The first member of the AWI-CM-1 ensemble. **(c,f)** The SO3 simulations.

The remaining discrepancies between eddy activity in SO3 and observations are relatively small, but exploring potential sources of disagreement may help in interpreting the simulations and guide future modeling endeavors. Greater skew in the distribution of EKE in the modeled dataset (Supplementary Table B2) could reflect multiple modes of circulation or seasonality. While seasonality of eddy activity in the ACC is low, seasonal ice cover likely affects eddy activity in the modeled dataset and certainly affects the observational dataset by producing gaps in its spatiotemporal coverage. Beyond differences in skew, this could contribute to the greater range of EKE seen in the SO3 simulations by systemically obscuring seasonal conditions from the observational dataset. Regional deficiencies of EKE in SO3 could be explained in terms of grid resolution outside of the study region; resolving the first Rossby radius of deformation

with at least two grid points is not enough to comprehensively reproduce mesoscale activity (Hallberg, 2013; Sein et al., 2017), and grid refinement may need to be expanded to upstream regions that impact eddy dynamics in the Southern Ocean. Other sources of bias may include ocean–atmosphere interactions which are absent or unrealistic within the uncoupled simulations (Byrne et al., 2016; Rai et al., 2021; Renault et al., 2016). In addition, some small-scale, slow-to-equilibrate ocean processes may be resolved in the high-resolution simulations but not be integrated long enough for their effects to impact eddy activity (Rackow et al., 2022; van Westen & Dijkstra, 2021). Finally, the gridded altimetry product itself may be responsible for some disagreement, as the along-track data are known to underrepresent eddy activity at scales less than 150 km and 10 days (Chassignet & Xu, 2017), which will be particularly impactful at high latitudes.

To distinguish a meaningful signal of anthropogenic impacts from natural variability, this analysis relies primarily on consistency among ensemble members (Figs. 3.3, 3.4). This is distinct from more traditional methods like assessment of error relative to observations or ensemble mean, commonly applied to weather forecasting (Ferro et al., 2012), but they can be compared to measurements of ensemble agreement used extensively in the IPCC reports (Fox-Kemper et al., 2021). Performance evaluation relative to observations would undoubtedly point to the high-resolution simulation as being superior due to the drastic underrepresentation of EKE in the eddy-permitting ensemble (Fig. 3.1). Yet, the effects of climate change are still apparent in the AWI-CM-1 ensemble (Figs. 3.1, 3.5), and the AWI-CM-1 dataset has been used to make similar projections of EKE already (Beech et al., 2022). Moreover, the eddy response to forcing seems to be consistent between the model resolutions when expressed in relative (Fig. 3.1g,h,i) rather than absolute terms (Fig. 3.1a,b,c). While more verification of this result is necessary both regionally and with other models, these results suggest that eddy-permitting resolutions can be interpreted with their shortcomings in mind in order to discern the real-world implications, as is often necessary with model data. Thus, based on the test case of the Southern Ocean, the usefulness of the AWI-CM-1 ensemble and the effectiveness of model simulations in identifying physically significant and reproducible impacts of climate change may be greater than would be identified using traditional methods and comes at a much lower cost relative to the eddy-resolving simulations.

This study has focused on EKE as an evaluation metric for the simulations since mesoscale activity is the primary motivation for increasing ocean model resolution. It has stopped short of assessing the improvements that resolving the mesoscale has on climate and ocean dynamics,

many of which are discussed in detail elsewhere (e.g. Hewitt et al., 2017). Rather than repeat an assessment of the benefits of resolving smaller scales, we assume that the accurate reproduction and evolution of eddy activity indicates that these improvements are transferred to broader processes. Certainly, inaccurate simulation of the mesoscale would raise questions regarding the improvements that this mesoscale activity should have on the simulations as a whole. Nonetheless, further evaluation of the modeling approaches employed in this study will be necessary to determine if these methods are appropriate for studying broader elements of the climate system. Since the high-resolution simulations derive their deep-ocean climate primarily from the medium-resolution spin-up simulation, improving the initialization process (Thiria et al., 2023) may be the critical barrier to extending these results from the mixed layer to the deeper ocean.

3.5 Conclusions

Resolving the ocean mesoscale has become a focus for the climate and ocean modeling community as computational capabilities expand and models become increasingly complex. The benefits that explicitly resolved eddy activity can have on climate simulations are clear (Hewitt et al., 2017; Sein et al., 2017) along with the impact that mesoscale variability has on local (Lachkar et al., 2009; Wang et al., 2017) and global environments (Falkowski et al., 1991; Sallée et al., 2012). However, state-of-the-art climate models will be unable to fully resolve the mesoscale for the foreseeable future, particularly in large-scale modeling endeavors such as CMIP (Hewitt et al., 2020). Thus, modelers must make informed choices regarding the explicit processes needed to answer research questions and where resources must be allocated to achieve specific goals. Existing analysis of resource allocation has typically addressed short-term weather forecasting or the ability to reproduce observations with low error (Ferro et al., 2012), but the question of how to best allocate resources for climate change impact assessment remains. This study has applied several cost-efficient modeling approaches to an analysis of the impacts of climate change on a key focus of high-resolution modeling: the mesoscale. Applying these results to broader climate change impact studies should improve the efficiency of resource allocation and focus modeling studies. Resolution can be dynamically adjusted both spatially, by focusing resources in study regions and where they are necessary to resolve local dynamics, and temporally, by allowing lower-resolution workhorse configurations to perform spin-up and transient runs. Limited simulation length and ensemble size can be sufficient for certain research questions and validation, but simulations must ultimately be designed to meet their specific goals.

Where resources are limited, studies may best include a combination of eddy-resolving simulations able to fully capture the local eddy field, as well as eddy-permitting simulations that can attest to the significance of results through consistency and repetition.

This work represents a contribution to the growing wealth of research that points to an intensification of eddy activity in the Southern Ocean (Beech et al., 2022; Hogg et al., 2015; Martínez-Moreno et al., 2021). The further conclusions that EKE variability may increase and that EKE intensification appears concentrated in key regions based on topography can both expand the present state of knowledge and direct future research. The cost-efficient modeling approaches of regional grid refinement, reduced-resolution spin-up and transient runs, and limited simulation lengths distinguished by longer periods of change are demonstrated to be effective at reproducing change within a more traditional eddy-permitting ensemble. When resources are limited and resolution demands are high, these approaches can be adapted to address specific research questions. Where assessing the robustness of change is critical, the complementary eddy-permitting ensemble represents an effective, low-cost supplement to the high-resolution simulation.

4

Eddy activity in the high-latitude Southern Ocean and its response to climate change

This chapter is in preparation for publication and is cited as Beech et al. (in prep.).

4.1 Abstract

Eddy activity in the high-latitude Southern Ocean is linked to critical drivers of the global climate such as Antarctic Bottom Water (AABW) formation, seasonal sea ice cover, and shoreward heat transport. Yet, no comprehensive description of eddy activity poleward of the Antarctic Circumpolar Current (ACC) exists and the mesoscale processes in the region are missing from virtually all major projections of climate change. Using a high-resolution ocean model and cost-reducing simulation design, a detailed dataset of regional mesoscale eddy activity is presented with 3-dimensional spatial coverage, unobstructed winter-season information, and projections of future conditions after prolonged anthropogenic warming. A rich mesoscale field is detected, with eddy activity closely related to largescale circulation features like gyres and the Antarctic Slope Current. Eddy activity peaks during Austral summer at approximately 95–100 m depth and exhibits a strong seasonal cycle in which sea ice growth decreases the eddy population and increases the proportion of anticyclones. Anthropogenic warming is projected to cause a broad intensification in eddy activity, although substantial regional declines also occur. ACC eddy activity is projected to encroach further poleward, Weddell Sea eddy activity reaches further westward, and the seasonal impacts of sea ice on eddy population and rotational direction are reduced.

4.2 Main

Mesoscale eddies are thought to be ubiquitous throughout the global ocean. Indeed, since satellites were first able to produce relatively comprehensive datasets of ocean surface velocity,

eddies have been identified throughout the altimetry-derived fields of surface flow (Chelton et al., 2011). Yet the effective range of altimetry-derived data is limited at the poles, where sea ice obscures the ocean surface and eddies can be smaller than the effective resolution of the altimetry products (Amores et al., 2018; Ballarotta et al., 2019). These gaps in the altimetry-based oceanographic understanding of the mesoscale are typically omitted from studies of ocean eddy activity, yet the relevance of eddy activity to ocean circulation, as well as the critical role of the polar regions in climate and climate change, are widely accepted (Bian et al., 2023; Bronselaer et al., 2018; Frey et al., 2023; Pauling et al., 2017; Thompson et al., 2014; van Westen & Dijkstra, 2021). Therefore, the missing polar mesoscale may be a serious shortcoming in the modern understanding of ocean dynamics. The limitations of satellite altimetry can feasibly be addressed using climate models, however, in the high latitudes, the low local Rossby radius substantially increases the computational cost of simulating the mesoscale. Now, new approaches to ocean modeling have been able to reduce the computational burden of investigating ocean eddy activity (Beech et al., 2022, 2024), presenting an opportunity to integrate the polar ocean mesoscale into the global understanding of ocean dynamics.

While the polar regions are challenging to research across scientific fields, it is undoubtable that the high-latitude Southern Ocean plays a critical role in global ocean circulation and climate. The seas surrounding the Antarctic continent host the formation sites of most of the AABW occupying the deepest portions of the ocean and forming the lower branch of global meridional overturning circulation (MOC; Johnson, 2008; Orsi et al., 1999; Thompson et al., 2014). The region hosts the southern part of the world's sea ice, steering Southern Hemisphere albedo (Frey et al., 2018), transporting freshwater equatorward (Haumann et al., 2016), and representing a feedback mechanism for anthropogenic climate change (Colman, 2003). The Antarctic shelf waters, and particularly the Antarctic Slope Current (ASC), shield the marine-terminating Antarctic glaciers and ice sheets from warmer waters, regulating freshwater flux from meltwater and again, representing a feedback mechanism to anthropogenic warming (Bronselaer et al., 2018; Pauling et al., 2017). Direct connections can be drawn between these globally impactful oceanic processes of the high southern latitudes and regional mesoscale activity; eddy activity introduces the precursors of AABW to the polar gyres (Roach & Speer, 2019; Ryan et al., 2016; Schröder & Fahrbach, 1999), and facilitates shoreward transport of warm mid-depth water onto the continental shelves where it can become denser and sink (Thompson et al., 2014). Seasonal ice melt may be hastened by eddy activity through the disturbance of insulating layers of cold meltwater below retreating ice (Horvat et al., 2016). Mid-depth, cross-

slope heat transport toward the Antarctic continent and ice shelves is attributed mainly to eddy activity, primarily through isopycnal eddy stirring (Nøst et al., 2011; Stewart et al., 2018; Stewart & Thompson, 2015), and eddies have been observed contributing to vertical heat transport in ice shelf cavities (Friedrichs et al., 2022). While not an exhaustive list, these examples of mesoscale impacts on both high-latitude and global ocean circulation demonstrate the importance of high-latitude eddy activity both today and particularly in the context of anthropogenic warming. The absence of high-latitude mesoscale flows from widely referenced climate simulations such as the Coupled Model Intercomparison Project (CMIP) may then explain the consistent poor performance in the region relative to observations (Luo et al., 2023; Wang, Zhang, et al., 2014) and potentially confound projections of global climate change.

Although a comprehensive, pan-Antarctic description of the ocean mesoscale is absent from the literature, there is a patchwork of knowledge to be sourced from in-situ observations, remote sensing, and modeling research. Perhaps most notable, is the altimetry-derived sea surface height dataset of the seasonally ice-covered Southern Ocean, which is similar to the altimetry products typically used to study low-latitude eddy activity, but relies on measurements from sea ice leads (Auger et al., 2022). Eddy tracking has been applied to this dataset, but as the authors acknowledge, the dataset is too coarse to identify typical eddies in the region according to the local Rossby radius (Auger et al., 2023). Moreover, the peak of eddy activity, particularly in ice-covered regions, is likely below the surface and beyond the range of sea surface height-based detection (Frenger et al., 2015; Li et al., 2024). In-situ observations of eddies also exist in the high latitudes (Manley & Hunkins, 1985; Morozov et al., 2020; Sallée et al., 2023; Timmermans et al., 2008; Zhao et al., 2014, 2016), but are more common in the Arctic and, relative to satellite or model-based eddy tracking, the sample size and spatial coverage of observations is low. Finally, a limited range of modeling studies have been performed with resolutions sufficient to resolve eddy activity in the high southern latitudes. One such described the contribution of eddies to shoreward heat transport via Reynolds decomposition (Stewart et al., 2018), but relied on just over a year of data and stopped short of a detailed description of the mesoscale field. Others rely on regional models to investigate various small-scale processes such as tidal or mesoscale contributions to circulation, but these are limited in spatial scope (Huot et al., 2022), often stop short of describing the mesoscale itself (Graham et al., 2016; Robertson, 2005), and can omit important external factors such as the ACC.

The Finite volumE Sea-ice Ocean Model version 2 (FESOM2) is a post-CMIP6 model with multi-scale horizontal resolution capabilities, enabling the concentration of computational

resources in focal regions within global simulations (Danilov et al., 2017; Scholz et al., 2019, 2022). This approach has now been demonstrated in multiple non-idealized use cases to be an effective approach to simulating mesoscale processes that would be computationally prohibitive with traditional model grids (Beech et al., 2022, 2024; Li et al., 2024). In particular, (Beech et al., 2024) employed FESOM2 and a cost-reducing simulation design to simulate the Southern Ocean with fully eddy-resolving conditions nearly until the Antarctic coast, both historically and within a projected climate change scenario. This dataset has been demonstrated to accurately reproduce observed mesoscale activity, as well as the anticipated mesoscale response to climate change in the mid-latitude Southern Ocean (Beech et al., 2024). In this study, the dataset will be applied to the high southern latitudes to reveal the regional mesoscale structure and regional eddy characteristics by exploiting the excellent spatio-temporal resolution, 3-dimensional spatial coverage, and extensive contextual climatic information that the modeled dataset can provide. For the first time, the impacts of anthropogenic climate change on mesoscale activity in the region will be examined and the physical drivers related to the changes will be investigated. In doing so, processes missing from most major global climate simulations can be identified and used to strengthen the modern oceanographic literature, interpret existing modeling studies, and inform future modeling efforts.

4.3 Results

4.3.1 Horizontal eddy distribution and characteristics

On the northern boundary of the study region, eddy activity from the ACC is discernable by its eastward propagation, large eddy size and vorticity amplitude, and general separation from higher latitude activity by low-activity regions (Fig. 4.1, 4.2a,d). Poleward of this, the high-latitude Southern Ocean is host to near-circumpolar eddy activity with distinct westward propagation and interruptions only around the West-Antarctic Peninsula and the Iselin Bank of the Ross Sea (Fig. 4.1). Along the Antarctic continental shelf, bathymetric features that steer the mean flow meridionally produce intense local mesoscale activity (Fig. 4.1). In the Ross Sea, this occurs as the continental shelf at the Iselin Bank steers the ASC northward and in the eastern Weddell Sea, this occurs as the ASC interacts with the Gunnerus Ridge and Astrid Ridge. The Maud Rise also concentrates flow over its northern flank and interactions with the Taylor column above the rise generate high eddy activity downstream (Fig. 4.1, 4.3a,c; Akitomo, 2006; Holland, 2001). In the open ocean, where bathymetric features do not steer largescale circulation, the western Weddell Sea is the largest eddy-rich region poleward of the eastward propagating ACC eddy activity. Here,

eddies which detach from the ASC are able to propagate zonally without being reincorporated into the mean flow, substantially increasing the mean eddy lifespan (Fig. 4.2b). Eddy trajectories tend to follow the closed contours of barotropic stream function associated with the circulation of the Ross and Weddell Gyres (Fig. 4.1, 4.3a). In both gyres, inflow at the northeast corners where ACC waters with distinct properties can be introduced are sites of high eddy activity (Fig. 4.1). The presence of detected eddies is quite consistent with eddy kinetic energy (EKE) from Reynolds decomposition (Fig. 4.3b), with the exception of the Ross Sea continental shelf, where relatively high EKE is either non-coherent or otherwise undetected (Fig. 4.1, 4.3b).

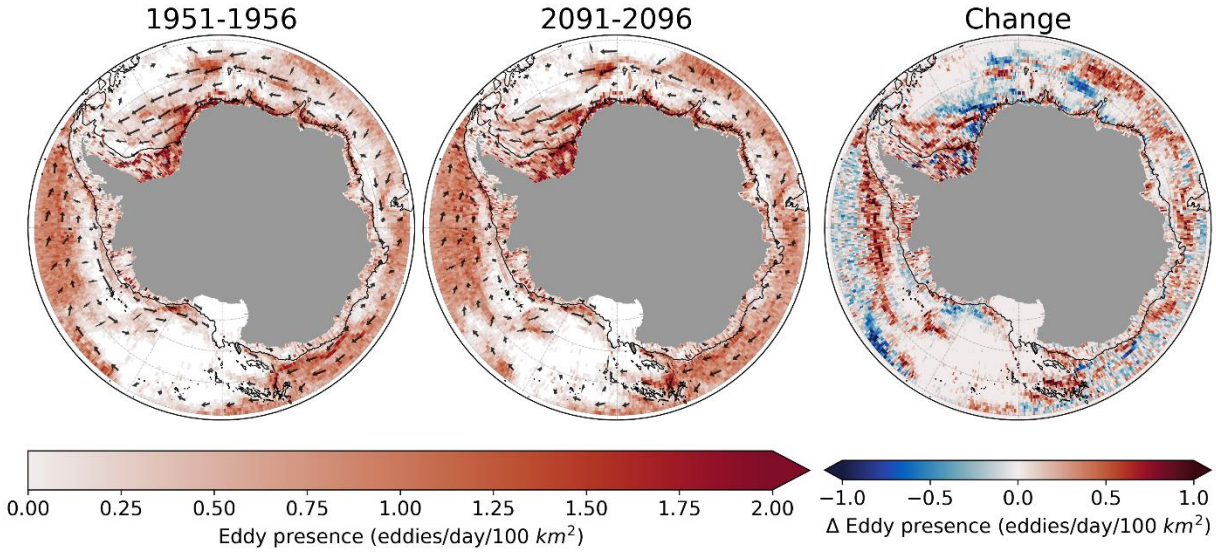

Figure 4.1. Horizontal distribution of high-latitude Southern Ocean mesoscale activity. Eddy presence in 1951–1956 (left) and 2091–2096 (center) and the difference between the two periods (right) grouped in 0.5° by 0.5° bins. Black arrows are the mean eddy trajectories in a 2.5 by 8 deg grid overlaid for regions with a sample size greater than 50. Distances are exaggerated by a factor of 4 for visibility. The black contour is the 2150 m isobath.

Following long, sustained anthropogenic climate change, the large, fast-moving, and eastward propagating ACC eddies in the north of the study region are projected to advance southward, generally occupying space that was previously eddy-poor, such as the northern Bellingshausen and Amundsen seas, and offshore of East Antarctica, north of the ASC (Fig. 4.1, 4.2a,d). This is likely due to the southward encroachment and intensification of westerlies which is widely anticipated to strengthen eddy activity in the ACC (Fig. 4.3d; Marshall, 2003; Munday et al., 2013). Along the ASC, change in eddy presence can be inconsistent (Fig. 4.1), but EKE reveals a clearer picture, with ASC eddy activity intensifying and activity immediately north of the current declining (Fig. 4.3b). This sharp boundary explains the noise within the binned eddy-

presence data and indicates a restriction of the current's northern extent, possibly due to steeper density gradients or the southward shift of westerlies (Fig. 4.3c,d). Eddy activity also advances westward in the Weddell Sea, where it was historically nearly completely absent (Fig. 4.5a), possibly following the reduction of sea ice where it was historically present year-round (Fig. 4.4b). A southwestward shift of the Weddell Gyre and a slightly more southward flow direction appears to be responsible for the southward shift of eddy activity downstream of the Maud Rise (Fig. 4.1, 4.3a). In the Ross Sea, eddy activity associated with ASC-bathymetry interactions appears to shift slightly downstream (Fig. 4.1, 4.3a,c), again, potentially due to sea ice retreat from a historical year-round refuge (Fig. 4.4b). While the Ross gyre does not appear to strengthen, eddy activity associated with recirculation and inflow in the northeast corner does increase.

Mean eddy lifespan tends to be shortest over the shelf, and highest in the gyre interiors, where low background flow is less likely to re-entrain mesoscale features into the larger scale circulation (Fig. 4.2b). Similarly, eddy propagation speed is highest where background circulation is strongest, primarily around the ASC and southern reaches of the ACC, indicating that the main source of eddy propagation is movement with the mean flow (Fig. 4.2c). As expected, eddy size varies relatively consistently with latitude, although the poleward shift of large ACC eddies in the projected period reflects a minor role for eddy propagation (Fig. 4.2d). After sustained warming, eddy size tends to decrease in the gyre interiors where sea ice may have historically had a filtering effect on smaller eddies (Figure 4.2d, 4.4a,b). Few if any clear climate change signals appear in the pattern of eddy lifespan, while eddy propagation speed and vorticity amplitude remain relatively consistent with the distribution of mean and eddy kinetic energy, primarily increasing along the ACC and ASC paths (Fig. 4.2a,c, 4.3c).

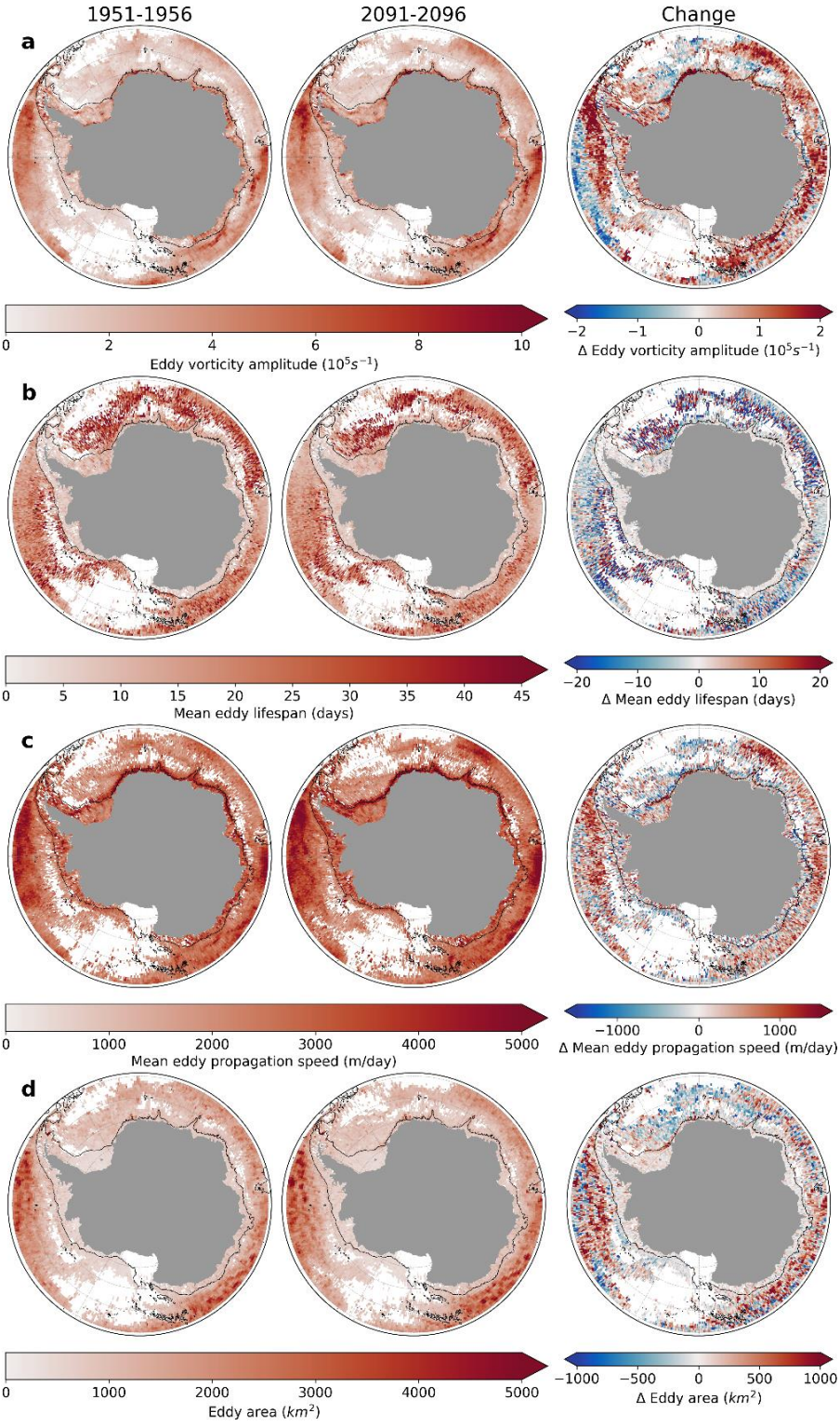

Figure 4.2. Horizontal eddy characteristics. (a) Vorticity amplitude. **(b)** Lifespan. **(c)** Propagation speed. **(d)** Eddy area. Each variable is the average of eddies in 0.5° by 0.5° bins. The left column corresponds to the 1951–1956 period, the middle column corresponds to the 2091–2096 period, and the right column corresponds to the difference between the periods.

4.3.2 Vertical and seasonal eddy characteristics

The historical eddy population exhibits a seasonal peak in the austral summer at approximately 95–100 m depth (Fig. 4.5a). The seasonal minimum population occurs in Austral winter (September–November), at the ocean surface (0–5 m), where the damping effects of sea ice are strongest (Fig. 4.3c). Both the cyclonic and anticyclonic eddy populations exhibit similar seasonal patterns and peaks as a function of depth (Fig. 4.5c,d), but considering the ratio of cyclones to anticyclones, some seasonal differences become apparent; the strongest dominance of one eddy type occurs in Austral winter, when anticyclones reach over 55% of total detected eddies (Fig. 4.5b). The anticyclone majority is concentrated at the surface and occurs just before the seasonal eddy minimum. In Austral summer, cyclones form the majority of eddies at depth, while a slight anticyclonic majority persists near the surface. Mean eddy size peaks at approximately the same time as the population minimum and the anticyclone majority peak (Fig. 4.6a,b) suggesting a filtering of smaller eddies by sea-ice damping, which would favor the typically larger anticyclones. Both eddy types exhibit mean vorticity amplitude maxima around their population maxima (Fig. 4.6c,d), but interestingly, the cyclonic population includes a second vorticity maximum around the population minimum and the anticyclonic majority, again, potentially indicating a sea ice filtering mechanism.

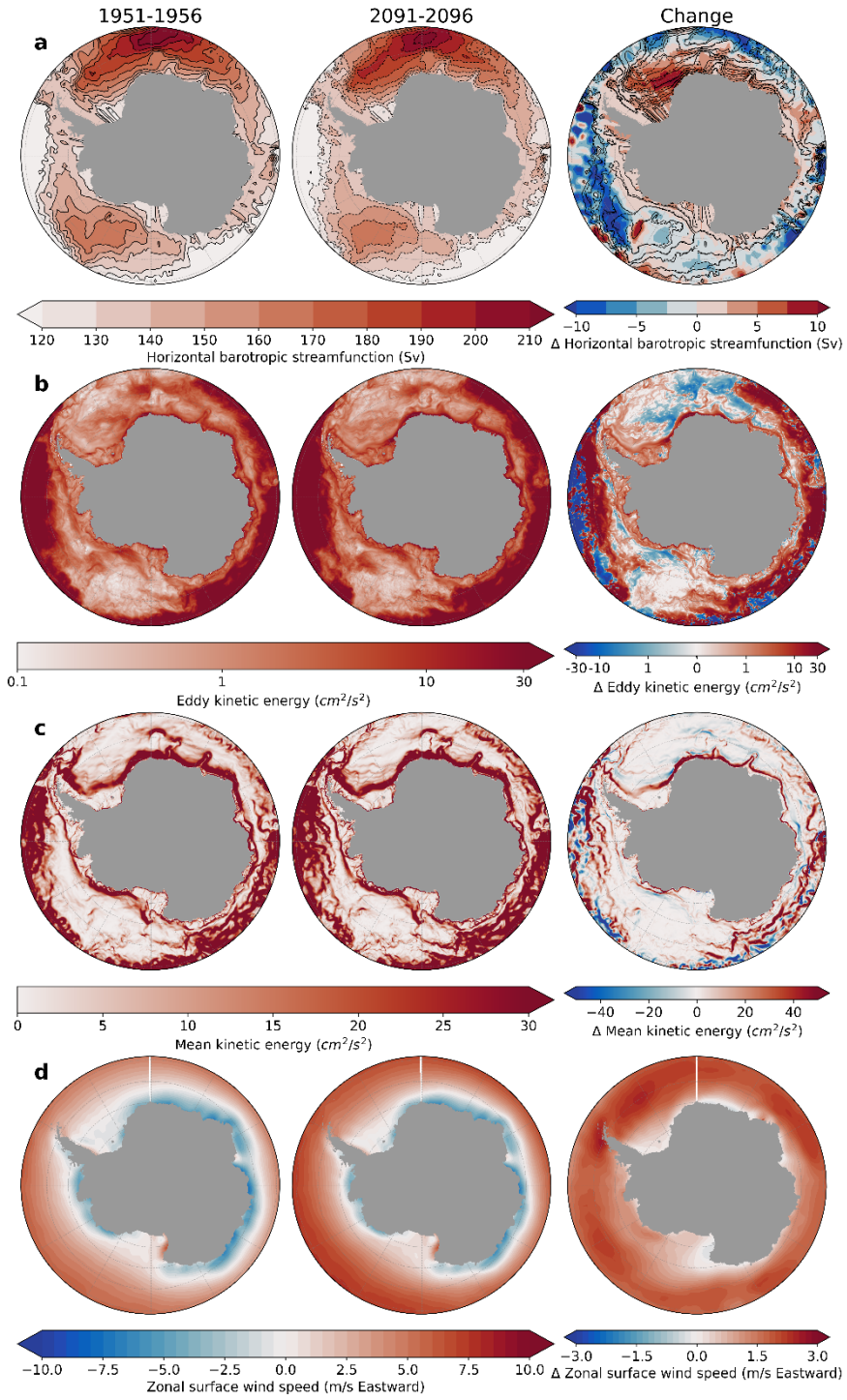

Figure 4.3. Annual mean climate variables. (a) vertically integrated horizontal barotropic stream function. **(b)** Mean eddy kinetic energy at 95–100 m calculated by decomposing the time-varying and time-mean components of kinetic energy. Note the logarithmic scales. **(c)** Mean kinetic energy at 95–100 m depth. **(d)** Mean zonal wind speed. The left column corresponds to the 1951–1956 period, the middle column corresponds to the 2091–2096 period, and the right column corresponds to the difference between the periods.

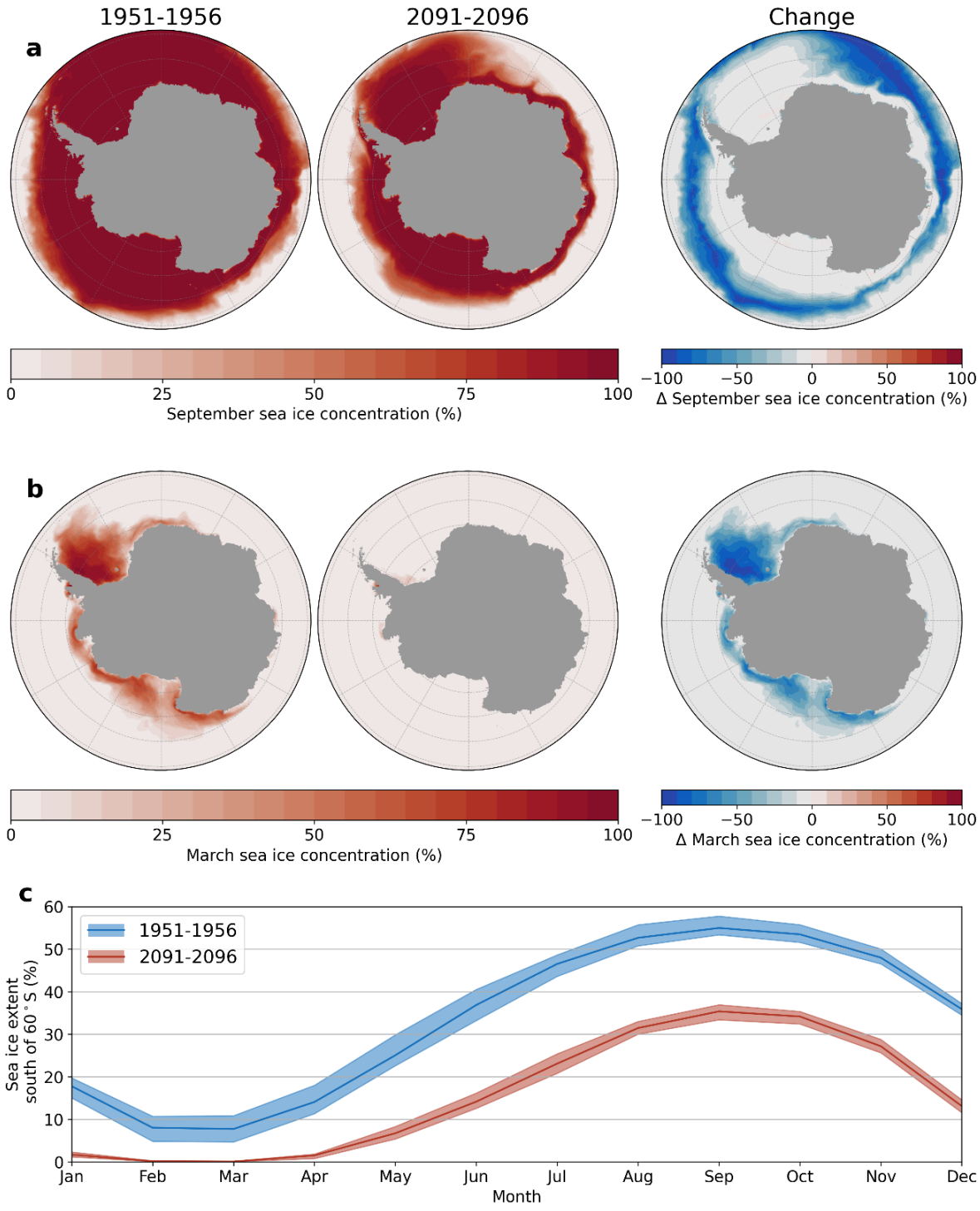

Figure 4.4. Sea ice seasonality and change. (a) September sea ice concentration. **(b)** March sea ice concentration. **(c)** Monthly sea ice concentration south of 60 °S. In panels **(a)** and **(b)**, the left column corresponds to the 1951–1956 period, the middle column corresponds to the 2091–2096 period, and the right column corresponds to the difference between the periods. In panel **(c)**, dark red and blue lines represent the mean climatology and the shaded areas represent the range of sea ice concentration over the six-year periods.

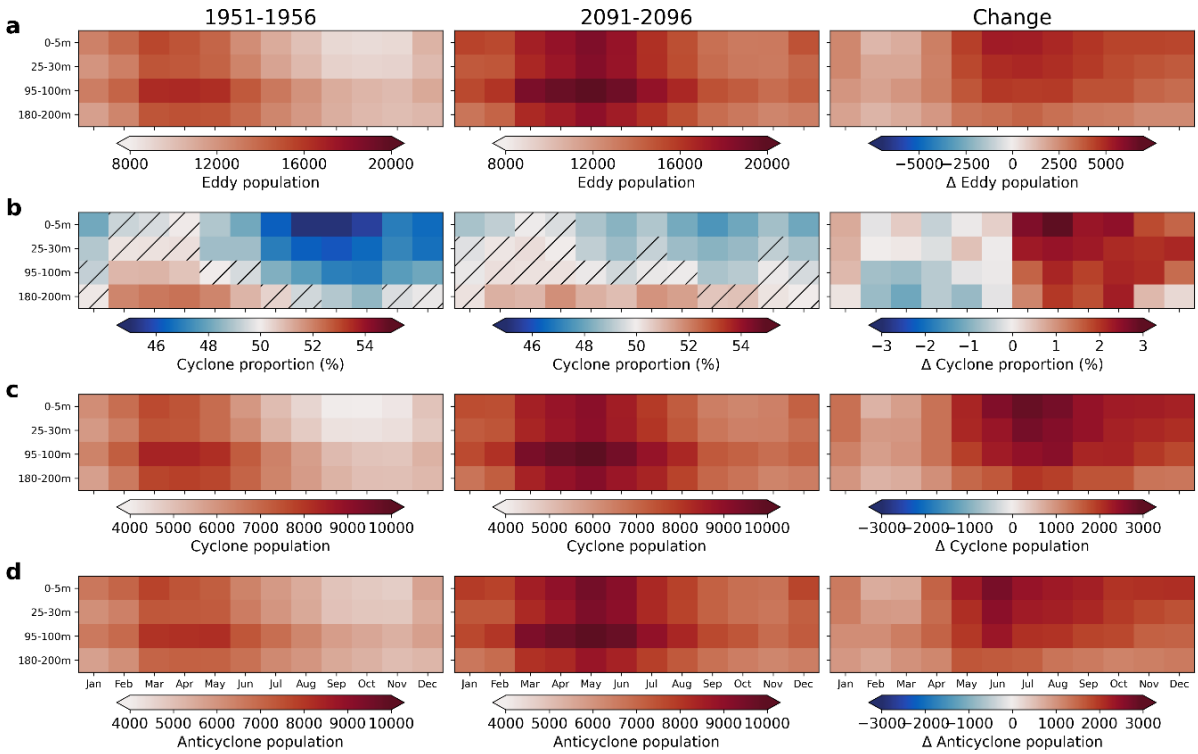

Figure 4.5. Vertical and seasonal eddy populations south of 60 °S. (a) Total eddy population. **(b)** percentage of cyclones in the total eddy population. **(c)** Cyclonic eddy population. **(d)** Anticyclonic eddy population. Left column figures are of the 1951–1956 period, middle column figures are of the 2091–2096 period, right column figures are the difference between the periods. The populations are defined as the sum of the monthly values over the entire six-year periods. Eddies that exist during multiple months are counted once in each month. Insignificant deviations from equal proportions (less than 95% confidence) are hatched.

After four degrees of warming, the eddy population rises by between 1500 and 5000 eddies per month, calculated cumulatively over the six-year period, with the largest increases occurring at the ocean surface in June and July (Fig. 4.5a). The population peak remains at 95–100 m depth, but shifts from March/April to May, reflecting the extended period of low Southern Ocean sea ice (Fig. 4.3c). As in the historical period, both cyclonic and anticyclonic eddy populations exhibit similar seasonal and depth patterns (Fig. 4.5c,d), but vorticity regimes decline; the anticyclone majority is weakened and concentrated closer to the surface, while the cyclone majority at 180–200 m depth becomes weaker in Austral summer and extends further into Austral winter (Fig. 4.5b). This could reflect a shoaling of the winter mixed layer in addition to the decline of selective eddy killing. Change in eddy size is weak at the historical peaks during the population minimum and stronger increases at deeper levels reduce the size gradient over depth (Fig. 4.6a,b). The surface changes are consistent with a reduction in winter-season damping

of small eddies by sea ice, enabling smaller eddies to survive and reduce the mean area, particularly in the ice-dominated gyre interiors (Fig. 4.2d). Meanwhile, the increase in mean eddy area outside of these regions appears dominated by ACC eddy intrusion (Fig. 4.2d). Mean vorticity amplitude rises with a similar pattern to population growth, but the winter-season cyclonic vorticity amplitude peak is greatly diminished, revealing a lesser role for sea ice (Fig. 4.6c,d).

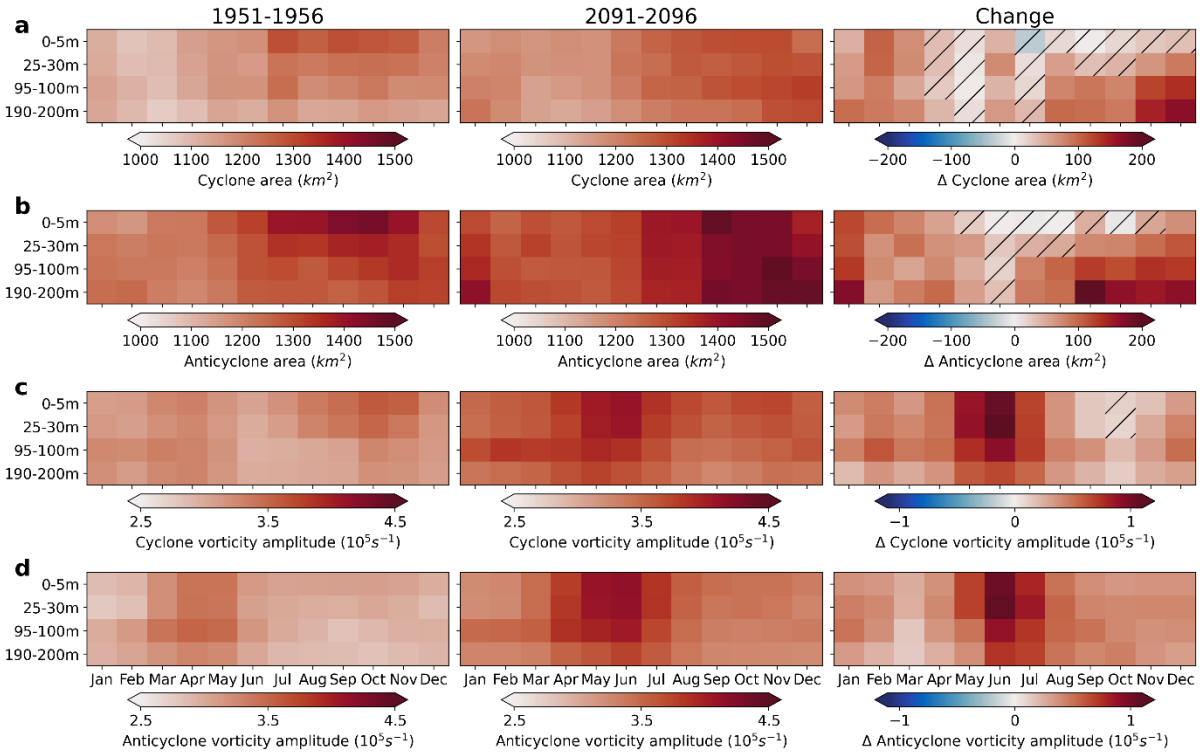

Figure 4.6. Vertical and seasonal eddy characteristics south of 60 °S. (a) Monthly mean area of cyclonic eddies. **(b)** Monthly mean area of anticyclonic eddies. **(c)** Monthly mean vorticity amplitude of cyclonic eddies. **(d)** Monthly mean vorticity amplitude of anticyclonic eddies. Left column figures are of the 1951–1956 period, middle column figures are of the 2091–2096 period, right column figures are the differences between the periods. Insignificance differences of means (less than 95% confidence) are hatched.

4.4 Discussion

The detected ratio of cyclonic and anticyclonic eddies (Fig. 4.5b) stands out in contrast to comparable research in the Arctic Ocean, where studies based on under-ice observations consistently report anticyclonic dominance of up to 95% of the eddy population (Manley & Hunkins, 1985; Timmermans et al., 2008; Zhao et al., 2014, 2016). In these simulations, only a slight anticyclonic majority of up to 55% during winter is found (Fig. 4.5b), but the data sources

and oceanic conditions at the two poles may explain the disagreement; the simulated anticyclonic majority in Fig. 4.5 is a seasonal process, reaching its peak around the sea ice maximum (Fig. 4.3c). Meanwhile, reports of anticyclonic dominance within the Arctic mixed layer eddy population typically come from instruments that rely on sea ice as an observation platform, mainly ice-tethered profilers (Timmermans et al., 2008; Zhao et al., 2014, 2016) or earlier, manned camps (Manley & Hunkins, 1985). The sea ice most suited to ice-based instruments is thick, multiyear ice in regions that are unlikely to melt before multiple seasons of observations (Toole et al., 2011). In these regions, a sea-ice filter may persist over long periods of time, sustaining and further developing the anticyclonic majority. Not only would this selectively observe eddies in more anticyclone-dominated regions of the Arctic, it is also a poor analogue to the high-latitude Southern Ocean, where multi-year ice is far less common. In more seasonally ice-covered regions of the Arctic Ocean, the tendency of vorticity direction may more closely resemble the historical Southern Hemisphere conditions presented here and in the context of climate change, the anticyclonic majority in both hemispheres can be expected to decline. Given the inverted thermal and haline anomalies typically associated with cyclones and anticyclones (Frenger et al., 2013, 2015; Huot et al., 2022), this regime shift could have broader impacts on the polar regions.

Sea ice is theorized to be responsible for both eddy generation and eddy killing (Auger et al., 2023; Giddy et al., 2021; Meneghello et al., 2020), but the seasonal cycle of the eddy population indicates that eddy killing is the dominant impact (Fig. 4.5). The spatial distribution of eddy activity (Fig. 4.1) also suggests a minimal role for sea ice as a generation mechanism; focal points of eddy presence are concentrated around currents, bathymetric features, and gyres, similar to the lower latitudes. Outside of these regions, eddies are relatively scarce. Yet, if ice were a major contributor to eddy generation, eddy activity could be expected to occur relatively consistently throughout the seasonal ice zone. While the seasonal cycle of cyclonic/anticyclonic majorities could indicate a secondary role for sea ice-related eddy generation in producing the excess of anticyclones in winter through brine rejection, a selective filtering mechanism is also possible. For example, Manucharyan & Timmermans (2013) describe a dipolar generation tendency which places cyclones at shallower depths, exposing them to greater sea ice drag. Sea ice also appears to dampen smaller eddies disproportionately, leading to the larger winter mean areas (Fig. 4.6a,b), and cyclonic eddies tend to be smaller than anticyclones (Fig. 4.5e,f). Regardless, eddies generated by any source may still have an impact on sea ice in turn, such as by disturbing

insulating layers of meltwater as proposed by (Horvat et al., 2016). Thus, our description of the mesoscale field may contribute to an understanding of seasonal sea ice cycles.

Eddy activity has the potential to influence both AABW formation and shoreward heat transport in similar ways; first, eddy activity is responsible for a substantial portion of the inflow of relatively warm ACC water into the Ross and Weddell Gyres (Roach & Speer, 2019; Schröder & Fahrbach, 1999). In the Weddell Gyre, warm water entry forms a two-core structure around 20–30 °E, with the northern core comprised of eddies detaching from the ACC as it is bathymetrically steered south, and the southern core flowing with the ASC and southern gyre boundary from further east (Ryan et al., 2016). In both the historical and projected period, this structure is well resolved (Fig. 4.1), but based on both eddy propagation and the paths of gyre circulation, it appears that the southern core is more relevant to coastal processes, while the northern core is steered north of the Maud Rise and into the Weddell Gyre interior (Fig. 4.1, 4.3a). Once warm ACC waters are entrained in the boundaries of both the Ross and Weddell Gyres, cross-slope transport can be facilitated by eddy activity along the slope front (Nøst et al., 2011; Stewart et al., 2018; Stewart & Thompson, 2015; Thompson et al., 2014). High eddy activity is ubiquitous along the ASC path, but the Eastern Weddell and Ross Seas are particularly active, along with parts of East Antarctica and the Bellingshausen Sea (Fig. 4.1, 4.3b). Likewise, eddy activity is projected to rise throughout the ASC as the climate warms, but intensification is concentrated in historically elevated regions. Thus, eddy activity can be expected to accelerate the rate of ice shelf melt due to anthropogenic warming to varying degrees regionally. Similarly, eddy activity before the Larson and Filchner-Ronne Ice Shelves is projected to intensify, potentially facilitating higher AABW production (Thompson et al., 2014), while in the Ross Sea, eddy activity upstream of the shelf may decline and over the shelf, coherent eddies are not detected.

4.5 Conclusion

The high-latitude Southern Ocean mesoscale has been revealed in a consistent, pan-Antarctic framework with unprecedented detail. Close links to currents, gyres, and bathymetry, as well as a sea ice-mediated seasonal cycle have been identified. The results can serve to unify the patchwork of existing knowledge from satellite altimetry, regional and idealized models, and in-situ observations. As anthropogenic climate change progresses, eddy activity can be expected to expand into formerly eddy-poor regions as ACC activity intrudes poleward and sea ice damping declines. This will impact eddy characteristics including lifespan, size, and vorticity direction, as well as the seasonal cycle of the eddy population. The results carry implications for shoreward

heat transport, which is mediated by eddy mixing and may accelerate ice shelf melt as eddy activity intensifies, as well as MOC, which can be facilitated by eddy transport toward crucial AABW formation sites, although diverse responses to climate change are projected regionally. These processes each warrant dedicated studies of their own and high-latitude eddy effects should be considered impactful missing processes in most projections of climate change.

4.6 Methods

4.6.1 Model simulations and data

The simulations analyzed in this study are described extensively in Beech et al. (2024). For the sake of completeness, a brief outline is included here. The model data was produced with the Finite volumE Sea-ice Ocean Model version 2 (FESOM2; Danilov et al., 2017) using a cost-reducing experiment design and a multi-resolution ocean grid with a regional focus on the Southern Ocean (Supplementary Fig. C1). FESOM2 is the successor of the Finite Element Sea-ice Ocean Model version 1.4 (FESOM1.4; Wang, Danilov, et al., 2014) after numerous updates and improvements (Scholz et al., 2019, 2022) which are ongoing. The precise iteration of the model used in this study was FESOM2.5 (Danilov et al., 2024), which, among other things, implemented the ability to initialize sea ice variables from user-defined datasets; an important aspect of these experiments. The most notable feature of both FESOM1.4 and 2.5 is the unstructured horizontal ocean grid which employs a mesh of spherical triangles to enable variable horizontal resolutions throughout the model domain. The sea ice component is unique to FESOM, the Finite Element Sea Ice Model, and employs elastic-viscous-plastic rheology (Danilov et al., 2015).

The simulations with FESOM2.5 consisted of four parts. The first was a transient, ocean-only simulation on a medium-resolution mesh stretching from 1851 to 2100, forced with atmospheric data taken from AWI-CM-1-1-MR's CMIP6 contribution (Semmler et al., 2020) to the historical (Eyring et al., 2016) and ScenarioMIP (O'Neill et al., 2016) simulation frameworks. During the projected period beginning in 2014, shared socioeconomic pathway (SSP) 3-7.0 (Riahi et al., 2017) is simulated, resulting in approximately 4 °C of mean global surface temperature rise as a result of anthropogenic climate change over the course of the simulations. This simulation was initialized from roughly preindustrial conditions after the 500-year spin-up period of AWI-CM-1-1-MR in the preindustrial control framework of CMIP6 (Eyring et al., 2016). The ocean grid used in this simulation was the same one used by AWI-CM-1-1-MR during CMIP6, consisting of approximately 830,000 ocean surface nodes and horizontal resolutions ranging from 10–40 km in the Southern Ocean (Semmler et al., 2020). The three remaining simulations consisted of short

time slices at various points during the progression of anthropogenic climate change, in which the model is reinitialized on a much higher-resolution, regionally focused mesh with the same atmospheric forcing as the medium-resolution transient simulation and initial ocean and sea ice conditions derived from the lower-resolution transient simulation. The high-resolution time slices began in 1950, 2015, and 2090, respectively, and were each run for 6 years. The first year of each simulation was discarded as a true spin-up, leaving 5 years of usable data. Later, the historical and projected period simulations were each extended by one year. The higher resolution mesh consists of 70 vertical layers and approximately 11 million nodes at the ocean surface, with a global resolution of approximately 25 km, gradually increasing to approximately 2.5 km in the Southern Ocean, the Agulhas current, and several narrow straits (Supplementary Fig. C1; Danilov, 2022). This configuration reaches eddy-resolving conditions in the ACC and the bulk of the Southern Hemisphere western boundary currents and maintains a global resolution comparable to high-resolution CMIP6 models. Poleward of the ACC, the grid is still eddy-resolving, as measured by the local Rossby radius of deformation (Hallberg, 2013), nearly to the Antarctic coast and only on the shelves does it become eddy-permitting or worse (Supplementary Fig. C1).

The high-resolution simulations were compared with observations of eddy activity derived from satellite altimetry data (Taburet et al., 2019) during the 2016–2020 period to assess the performance of the model configuration and the experiment design in reproducing observations (Beech et al., 2024). The simulations were also compared with the CMIP6 data from AWI-CM-1-1-MR to assess the impacts of climate change on ocean eddy activity relative to the more traditional simulation design of CMIP6. These comparisons were both primarily confined to the ACC region due to the limitations of the gridded satellite altimetry product in terms of both effective resolution and data availability beneath sea ice, as well as the limitations of the CMIP6 dataset in resolving high-latitude eddy activity. Again, details of these comparisons are outlined extensively by Beech et al. (2024). In short, the model reproduced observed levels of eddy activity remarkably well relative to altimetry-derived values. Between the historical period and the present day, the simulations were able to simulate a response to climate change that is within expected values considering natural variability and the limited dataset of a single ensemble member and a 5-year simulation length. However, without the aid of the ensemble of lower-resolution simulations in interpreting the high-resolution simulations, it would be difficult to distinguish the climate change signal from the noise of natural variability. Between the historical and projected periods, the effects of anthropogenic climate change on eddy activity became clear,

even considering a single ensemble member. Thus, the assessment of higher-latitude eddy activity in the context of climate change is limited to the historical and projected periods which have each been further extended by one year to ensure a sufficient signal-to-noise ratio to assess climate change impacts.

As further validation of the modeled results, numerous relevant variables are presented in Figure 4.5, both to help interpret the distribution and behavior of the detected mesoscale activities and to ensure that the broader climatic features driving eddy activity are themselves accurate. In Supplementary Figure C2, the Antarctic Oscillation Index (AOI; Gong & Wang, 1999) is shown to demonstrate both the state of the dominant atmospheric mode of variability, the Southern Annular Mode (SAM), in the historical and projected periods, as well as the impacts of climate change on the SAM. The SAM has substantial impacts on high-latitude Southern Ocean circulation and is one of the major mechanisms by which anthropogenic climate change will affect the region. Thus, it is important when assessing climate change impacts using short simulation lengths that the state of the SAM be consistent in each period. From Supplementary Figure C2, it is clear that the AOI defined relative to conditions in each simulation period is relatively neutral and not far removed, although of opposite sign. In contrast, the AOI during the projected period defined relative to historic conditions indicates that the SAM is substantially different than its historic state, meaning the climate change signal vastly outweighs potential noise.

4.6.2 Data processing

Daily velocity fields at selected vertical levels were first filtered and interpolated to a high-resolution, rectangular grid before eddy detection and tracking. The spatial filtering was performed using an implicit filter method described in (Danilov et al., 2023), and a band pass filter between length scales of 10 and 100 km was chosen to isolate well-resolved eddies on the model grid (minimum radius twice the local grid spacing) and to help distinguish these features from larger background flow. Of course, since eddies are not always perfectly circular and filtering the velocity field may not fully remove the vorticity signature, smaller features may still be detected. Using linear interpolation, the smoothed data was transferred to a rectangular grid of 0.05° by 0.05° at the equator, with the latitudinal spacing reduced at higher latitudes to maintain approximately square grid cells. At high latitudes, the resulting rectangular grid is much higher resolution than the original grid to reduce any errors introduced through interpolation.

4.6.3 Eddy detection and tracking

Eddy detection based on the Okubo-Weiss parameter was performed using the python-based *eddytools* package (https://github.com/n-beech/eddytoolsnb) after several minor adjustments were introduced to accommodate the interpolated FESOM data. The detection algorithm identifies continuous regions in which the Okubo-Weiss parameter (Okubo, 1970; Weiss, 1991) (Eq. 4.1) is below a threshold, indicating that vorticity is dominant in the region.

(Eq. 4.1) $$w = s^2 + n^2 - \omega^2$$

where w is the Okubo Weiss parameter, s is shear strain, n is normal strain, and ω is relative vorticity.

To be accepted as an eddy, regions must contain an interior minimum, in other words, have increasing vorticity dominance between the perimeter and interior, and fall within a range of acceptable sizes based on the number of grid cells contained within the eddy. The threshold for the Okubo Weiss parameter was defined as one tenth of the temporal mean of the spatial standard deviation over the entire study region during the historical period. This value was calculated separately for each depth, but kept constant during the historical and projected periods to maintain consistent criteria. The minimum number of grid cells to comprise an eddy was defined as 100, which, given the variability of the grid cell sizes, places the minimum radius for a circular detected feature at approximately 6.5 km at the southern end of the study region, and 15.6 km at the northern end. The maximum number of grid cells within an eddy was left arbitrarily large, meaning there was no upper limit defined for eddy size.

Detected eddies were tracked based on similarity of size, vorticity direction, vorticity amplitude, and separation. The minimum and maximum growth thresholds for size and vorticity amplitude were defined as 0.5 and 1.5, meaning an eddy can grow or shrink by a maximum of half of its previous size or vorticity amplitude. The maximum distance between two eddy detections was defined as 12 km per day, which roughly translates to an eddy propagating in a background flow of 0.14 m/s, a relatively high speed along the fastest-moving circulation feature in the focus region, the ASC (Stewart et al., 2019). Finally, eddies with lifespans shorter than three days were removed, and eddies that dissipated after propagating less than 1 km per day from their point of genesis were removed.

The choices of parameters and thresholds in the detection and tracking steps were investigated thoroughly and the details of the effects are too numerous and minute to discuss

entirely. Primarily, lowering the thresholds for detection increases the number of detected eddies, but does not substantially change the spatial or seasonal distributions of the resulting eddy population. While some characteristics of the eddy population could be changed, such as lower average size given lower minimum thresholds, the spatial and seasonal patterns of these characteristics remained similar. Lowering the thresholds during the tracking stage lowered the total number of tracked eddies and increased lifespans, suggesting that several eddies were combined into individual tracks, accurately or not. Other works have performed more extensive evaluation of detection and tracking parameters through comparison with different algorithms and approximations of truth, but this work deserves its own dedicated study.

Eddy detection and tracking was performed at several depths in the upper ocean to produce a three-dimensional description of eddy activity that is necessarily absent from satellite and SSH-based detection methods. Eddy populations and characteristics from each level are presented in Figures 4.5 and 4.6, but spatial details are presented only for the population peak at 95–100 m depth. Other levels produced only minor population differences from the peak depth and relatively consistent spatial distributions. These figures are available in Appendix C, Supplementary Figures C3 to C8.

Eddy presence and characteristics in Figures 4.1 and 4.2 were grouped spatially based on the position of the eddy center within 0.5° by 0.5° bins. In Figures 4.5 and 4.6, eddies are grouped by month and characteristics or population sizes are calculated over the entire study region south of 60 °S. In Figure 4.5b, the statistical significance of the proportion of either eddy type deviating from equality was calculated using a one-proportion z-test (Fleiss et al., 2013), while in Figure 4.6 the difference between population means for each eddy characteristic between the two simulation periods was calculated using a t-test assuming unequal variance (Welch, 1947).

5

Synthesis of results and outlook

5.1 EKE representation

Despite reproducing 51 to 82% of observed EKE in eddy-rich regions, and little EKE at all outside of these regions, the global pattern of eddy activity reproduced in Chapter 2 reflects altimetry-derived values admirably in terms of spatial distribution. Relative to the rest of the CMIP6 ensemble, excluding HighResMIP, this level of representation of eddy activity is already remarkable. Moreover, when compared with a fully eddy-resolving simulation in the Southern Ocean in Chapter 3, the EKE changes projected after prolonged warming in CMIP6 are largely consistent relative to historic values. If the reliability of FESOM's CMIP6 projections translates to other regions, then the resource allocation strategy employed in these simulations can be considered a resounding success. Therefore, validating the projections of each ocean basin included in Chapter 2 with focused, fully eddy-resolving simulations as was done in Chapter 3 would be beneficial for reinforcing both the oceanographic findings and the multiscale approach. Additionally, validation of the results with other multiscale modeling techniques could reduce concerns over reliance on a single model (Biastoch et al., 2018).

In the ACC, where the high-resolution Southern Ocean simulations can be reliably compared with eddy activity from satellite altimetry, the results are also largely positive; in this case, the resolution of the grid suggests that EKE should be very well reproduced, and indeed, major foci of activity and the overall magnitude of EKE in the region are accurate, even considering just 5 years of data. Yet, the high resolution of the grid also raises expectations for the simulation and makes the minor regional shortcomings in reproducing observed EKE stand out. Regarding projected changes, the high-resolution simulations fall within the range of natural variability indicated by FESOM's CMIP6 projections, and therefore, the projections can be considered accurate. However, the CMIP6 projections also demonstrate that natural variability is

high enough to veil the effects of climate change after modest warming. Thus, when the CMIP6 ensemble cannot be used as a comparison, the climate impacts between the historical and present-day periods could be unreliable. This includes the analysis of high-latitude eddy activity, where the CMIP6 data is too coarse to provide a useful reference. In some ways, this result is disappointing, however, defining the limitations of the high-resolution, cost-minimizing approach is also a valuable conclusion that can help guide future work.

5.2 Model fidelity

In Chapter 1, one of the stated motivations for resolving eddy activity in climate models was to improve model fidelity, yet the evaluation in Chapters 2 to 4 is primarily focused on the accurate representation of eddy activity itself. Extensive evaluation of FESOM's CMIP6 simulations was performed by (Semmler et al., 2020) and is therefore not repeated, but these findings can help investigate the effectiveness of the variable resolution grid in faithfully representing the Earth system. Overall, AWI-CM-1-1-MR, in which FESOM in its partially eddy-resolving configuration was the ocean component, performed well relative to its peers in CMIP6. However, it was also not profoundly distinguished from eddy parameterizing models in many broad measures of model skill (Liu et al., 2022). Thus, eddy-resolving models will not make eddy-parameterizing models obsolete, but closer investigation is necessary to determine whether the advantages of eddy-resolving models outlined in section 1.1 can be observed in FESOM's CMIP6 contribution. For example, AWI-CM-1-1-MR was particularly strong in representing ACC strength, as well as its response to wind forcing (Beech et al., 2022; Semmler et al., 2020). This response is understood to be closely linked with eddy activity (Munday et al., 2013), meaning FESOM's performance could be attributed to the local resolution of the ocean mesh. Furthermore, comparing FESOM with unrelated models of varying complexity within the CMIP6 ensemble introduces a great deal of uncertainty in the attribution of model skill to any specific source. It may be more appropriate for an assessment of the impact of eddy activity on model fidelity to compare AWI-CM-1-1-MR to its lower-resolution counterpart, AWI-ESM-1-1-LR.

Considerably less evaluation of the high-resolution Southern Ocean simulations was performed, partially due to the experimental approach to concentrate on upper-ocean mesoscale activity with the caveat that the deep ocean had not been equilibrated. Given this limited use case, a focus on the validation of mesoscale activity against observations and more traditional projections of climate change is reasonable and provides a proof of concept for the simulation design. However, further evaluation with other variables and datasets could drastically expand

the range of applications in which this approach to high-resolution modeling might enable low-cost climate change projections. As a first step, other fast-to-equilibrate upper ocean processes could be evaluated and assessed independently of deep-ocean equilibration. Eventually though, the prospect of effective initialization of the deep ocean using lower-resolution spin-up simulations could present such drastic reductions in overall computational cost that this too becomes an objective for high-resolution modeling.

5.3 Oceanographic findings

The first CMIP-scale projections of climate change with key mesoscale features resolved revealed substantial and diverse changes in ocean eddy activity beyond what the observational record shows (Martínez-Moreno et al., 2021) or what physical relationships and larger-scale projected changes imply (Munday et al., 2013). Of particular importance is the finding that observable trends in EKE cannot necessarily be extrapolated as warming continues (Fig. 2.3, 2.4). In some regions, this alters expectations of change substantially, such as in the Gulf Stream, where observable changes suggest EKE is intensifying, but the long-term projections indicate weakening (Beech et al., 2022). This is also an effective demonstration of the advantages that the modeled dataset has over observations in studying eddy activity; due to the challenges with observing mesoscale features directly, the observational record is primarily limited to the altimetry record, which is approximately 30 years long (Taburet et al., 2019). As a result, the reliability of trends within the observational mesoscale dataset is marginal and improvements will only come over the course of years. Conversely, modeled datasets are able to extend simulations beyond the present day and prior to the observational record and, importantly in Beech et al. (2022), can take advantage of multiple ensemble members, or independent realizations of the same climatic state, to improve reliability further. The advantages of the modeled dataset become even clearer considering the high latitudes, where the observational record is shorter and less reliable. However, these advantages are not necessarily unique to FESOM, and as stated in section 1.2.2, models have their own challenges in resolving the mesoscale. Therefore, the success of Chapter 2, is the effective simulation of mesoscale activity within the robust CMIP6 framework at reduced computational cost using the multiscale methods facilitated by FESOM.

In the high latitudes of the Southern Ocean, the results of the high-resolution simulations outlined in Chapter 4 represent the most comprehensive description of eddy activity in the region that has been released to this date. The simulations not only reveal widespread eddy activity, but deep interconnectivity with regional ocean and climate and a dynamic response to anthropogenic

warming. Model simulations that do not explicitly resolve eddy activity in the high southern latitudes should take these results into account and consider whether the eddy processes relevant to various research goals are well parameterized. Similarly, in the Arctic Ocean, where simulations of eddy activity are also scarce, these findings can be used to contextualize observations, such as the dominance of anticyclonic eddies (Beech et al., in prep.; Timmermans et al., 2008; Zhao et al., 2014, 2016), and improve the understanding of mesoscale activity beneath sea ice. Returning to the prospect of using eddy-resolving models as a digital observation platform presented in Chapter 1, these results are a promising first step; the detected high-latitude Southern Ocean eddy activity is geographically located where it can be expected to impact AABW formation (Thompson et al., 2014), the seasonal cycle of ice melt (Horvat et al., 2016), as well as shoreward heat transport and ice shelf melt (Nøst et al., 2011; Stewart et al., 2018; Stewart & Thompson, 2015). However, this analysis has stopped short of direct study of the eddy processes. In some cases, there is still a shortcoming in the modeled dataset; AABW formation involves physical processes that take place over the continental shelf and within ice shelf cavities, meaning the high-resolution Southern Ocean simulations are insufficient in terms of resolution and coverage to study these processes directly. Instead, this work has indicated the relevance of eddy activity to AABW formation and that future, more focused studies have a promising avenue for climatic relevant research. In other cases, such as shoreward heat transport and sea ice melt, the dataset is likely suitable for direct studies of the role of eddy activity, but more analysis is required. Thus, while work remains to investigate critical high-latitude eddy processes, the potential for FESOM to facilitate these studies at reduced computational cost has been demonstrated.

Author contribution statements

Chapter 2:

Beech, N., Rackow, T., Semmler, T., Danilov, S., Wang, Q., & Jung, T. (2022). Long-term evolution of ocean eddy activity in a warming world. *Nature Climate Change*, *12*(10), 910–917. https://doi.org/10.1038/s41558-022-01478-3

Author contribution statement:

N.B., T.J., T.R. and T.S. conceived the study. N.B. conducted the analysis and drafted the manuscript. Q.W. provided sample code for geostrophic velocity and ocean volume transport calculations. S.D. contributed to the discussion of variable-resolution meshes and their effects on eddies. All authors contributed to the scientific discussion, reviewed and contributed to the text of the manuscript.

Chapter 3:

Beech, N., Rackow, T., Semmler, T., & Jung, T. (2024). Exploring the ocean mesoscale at reduced computational cost with FESOM 2.5: Efficient modeling strategies applied to the Southern Ocean. *Geoscientific Model Development*, *17*(2), 529–543. https://doi.org/10.5194/gmd-17-529-2024

Author contribution statement:

NB, TJ, TR, and TS conceived of the study. NB carried out the simulations, analyzed the data, and drafted the manuscript. All authors reviewed the manuscript.

Chapter 4:

Beech, N., Rackow, T., Semmler, T., & Jung, T. (in prep.). *Eddy activity in the high-latitude Southern Ocean and its response to climate change*.

Author contribution statement:

NB, TR, TS, and TJ conceived of the study. NB performed the simulations and analyzed the data. NB drafted the first copy of the manuscript. All authors contributed to the final version of the manuscript.

References

Akitomo, K. (2006). Thermobaric deep convection, baroclinic instability, and their roles in vertical heat transport around Maud Rise in the Weddell Sea. *Journal of Geophysical Research: Oceans*, *111*(C9). https://doi.org/10.1029/2005JC003284

Allison, L. C., Johnson, H. L., Marshall, D. P., & Munday, D. R. (2010). Where do winds drive the Antarctic Circumpolar Current? *Geophysical Research Letters*, *37*(12). https://doi.org/10.1029/2010GL043355

Amores, A., Jordà, G., Arsouze, T., & Le Sommer, J. (2018). Up to What Extent Can We Characterize Ocean Eddies Using Present-Day Gridded Altimetric Products? *Journal of Geophysical Research: Oceans*, *123*(10), 7220–7236. https://doi.org/10.1029/2018JC014140

An, B., Yu, Y., Hewitt, H., Wu, P., Furtado, K., Liu, H., Lin, P., Luan, Y., & Chen, K. (2023). The benefits of high-resolution models in simulating the Kuroshio Extension and its long-term changes. *Climate Dynamics*, *61*(11), 5407–5427. https://doi.org/10.1007/s00382-023-06862-z

Arz, H. W., Pätzold, J., & Wefer, G. (1999). The deglacial history of the western tropical Atlantic as inferred from high resolution stable isotope records off northeastern Brazil. *Earth and Planetary Science Letters*, *167*(1), 105–117. https://doi.org/10.1016/S0012-821X(99)00025-4

Auger, M., Prandi, P., & Sallée, J.-B. (2022). Southern ocean sea level anomaly in the sea ice-covered sector from multimission satellite observations. *Scientific Data*, *9*(1), Article 1. https://doi.org/10.1038/s41597-022-01166-z

Auger, M., Sallée, J.-B., Thompson, A. F., Pauthenet, E., & Prandi, P. (2023). Southern Ocean Ice-Covered Eddy Properties From Satellite Altimetry. *Journal of Geophysical Research: Oceans*, *128*(4), e2022JC019363. https://doi.org/10.1029/2022JC019363

Backeberg, B. C., Penven, P., & Rouault, M. (2012). Impact of intensified Indian Ocean winds on mesoscale variability in the Agulhas system. *Nature Climate Change*, *2*(8), Article 8. https://doi.org/10.1038/nclimate1587

Bailleul, F., Cotté, C., & Guinet, C. (2010). Mesoscale eddies as foraging area of a deep-diving predator, the southern elephant seal. *Marine Ecology Progress Series*, *408*, 251–264. https://doi.org/10.3354/meps08560

Bakker, P., Schmittner, A., Lenaerts, J. T. M., Abe-Ouchi, A., Bi, D., van den Broeke, M. R., Chan, W.-L., Hu, A., Beadling, R. L., Marsland, S. J., Mernild, S. H., Saenko, O. A., Swingedouw, D., Sullivan, A., & Yin, J. (2016). Fate of the Atlantic Meridional Overturning Circulation: Strong decline under continued warming and Greenland melting. *Geophysical Research Letters*, *43*(23), 12,252-12,260. https://doi.org/10.1002/2016GL070457

Balaji, V., Maisonnave, E., Zadeh, N., Lawrence, B. N., Biercamp, J., Fladrich, U., Aloisio, G., Benson, R., Caubel, A., Durachta, J., Foujols, M.-A., Lister, G., Mocavero, S., Underwood, S., & Wright, G. (2017). CPMIP: Measurements of real computational performance of Earth

system models in CMIP6. *Geoscientific Model Development*, *10*(1), 19–34. https://doi.org/10.5194/gmd-10-19-2017

Ballarotta, M., Ubelmann, C., Pujol, M.-I., Taburet, G., Fournier, F., Legeais, J.-F., Faugère, Y., Delepoulle, A., Chelton, D., Dibarboure, G., & Picot, N. (2019). On the resolutions of ocean altimetry maps. *Ocean Science*, *15*(4), 1091–1109. https://doi.org/10.5194/os-15-1091-2019

Bard, E., & Rickaby, R. E. M. (2009). Migration of the subtropical front as a modulator of glacial climate. *Nature*, *460*(7253), Article 7253. https://doi.org/10.1038/nature08189

Bauer, P., Dueben, P. D., Hoefler, T., Quintino, T., Schulthess, T. C., & Wedi, N. P. (2021). The digital revolution of Earth-system science. *Nature Computational Science*, *1*(2), Article 2. https://doi.org/10.1038/s43588-021-00023-0

Beech, N., Rackow, T., Semmler, T., Danilov, S., Wang, Q., & Jung, T. (2022). Long-term evolution of ocean eddy activity in a warming world. *Nature Climate Change*, *12*(10), 910–917. https://doi.org/10.1038/s41558-022-01478-3

Beech, N., Rackow, T., Semmler, T., & Jung, T. (2024). Exploring the ocean mesoscale at reduced computational cost with FESOM 2.5: Efficient modeling strategies applied to the Southern Ocean. *Geoscientific Model Development*, *17*(2), 529–543. https://doi.org/10.5194/gmd-17-529-2024

Beech, N., Rackow, T., Semmler, T., & Jung, T. (in prep.). *Eddy activity in the high-latitude Southern Ocean and its response to climate change*.

Bian, C., Jing, Z., Wang, H., Wu, L., Chen, Z., Gan, B., & Yang, H. (2023). Oceanic mesoscale eddies as crucial drivers of global marine heatwaves. *Nature Communications*, *14*(1), Article 1. https://doi.org/10.1038/s41467-023-38811-z

Biastoch, A., & Böning, C. W. (2013). Anthropogenic impact on Agulhas leakage. *Geophysical Research Letters*, *40*(6), 1138–1143. https://doi.org/10.1002/grl.50243

Biastoch, A., Böning, C. W., & Lutjeharms, J. R. E. (2008). Agulhas leakage dynamics affects decadal variability in Atlantic overturning circulation. *Nature*, *456*(7221), Article 7221. https://doi.org/10.1038/nature07426

Biastoch, A., Böning, C. W., Schwarzkopf, F. U., & Lutjeharms, J. R. E. (2009). Increase in Agulhas leakage due to poleward shift of Southern Hemisphere westerlies. *Nature*, *462*(7272), Article 7272. https://doi.org/10.1038/nature08519

Biastoch, A., Sein, D., Durgadoo, J. V., Wang, Q., & Danilov, S. (2018). Simulating the Agulhas system in global ocean models – nesting vs. Multi-resolution unstructured meshes. *Ocean Modelling*, *121*, 117–131. https://doi.org/10.1016/j.ocemod.2017.12.002

Bishop, S. P., Gent, P. R., Bryan, F. O., Thompson, A. F., Long, M. C., & Abernathey, R. (2016). Southern Ocean Overturning Compensation in an Eddy-Resolving Climate Simulation. *Journal of Physical Oceanography*, *46*(5), 1575–1592. https://doi.org/10.1175/JPO-D-15-0177.1

Bronselaer, B., Winton, M., Griffies, S. M., Hurlin, W. J., Rodgers, K. B., Sergienko, O. V., Stouffer, R. J., & Russell, J. L. (2018). Change in future climate due to Antarctic meltwater. *Nature*, *564*(7734), Article 7734. https://doi.org/10.1038/s41586-018-0712-z

Byrne, D., Münnich, M., Frenger, I., & Gruber, N. (2016). Mesoscale atmosphere ocean coupling enhances the transfer of wind energy into the ocean. *Nature Communications*, *7*(1), Article 1. https://doi.org/10.1038/ncomms11867

Caesar, L., Rahmstorf, S., Robinson, A., Feulner, G., & Saba, V. (2018). Observed fingerprint of a weakening Atlantic Ocean overturning circulation. *Nature*, *556*(7700), Article 7700. https://doi.org/10.1038/s41586-018-0006-5

Cai, W. (2006). Antarctic ozone depletion causes an intensification of the Southern Ocean super-gyre circulation. *Geophysical Research Letters*, *33*(3). https://doi.org/10.1029/2005GL024911

Chassignet, E. P., & Xu, X. (2017). Impact of Horizontal Resolution (1/12° to 1/50°) on Gulf Stream Separation, Penetration, and Variability. *Journal of Physical Oceanography*, *47*(8), 1999–2021. https://doi.org/10.1175/JPO-D-17-0031.1

Chassignet, E. P., Yeager, S. G., Fox-Kemper, B., Bozec, A., Castruccio, F., Danabasoglu, G., Horvat, C., Kim, W. M., Koldunov, N., Li, Y., Lin, P., Liu, H., Sein, D. V., Sidorenko, D., Wang, Q., & Xu, X. (2020). Impact of horizontal resolution on global ocean–sea ice model simulations based on the experimental protocols of the Ocean Model Intercomparison Project phase 2 (OMIP-2). *Geoscientific Model Development*, *13*(9), 4595–4637. https://doi.org/10.5194/gmd-13-4595-2020

Chelton, D. B., deSzoeke, R. A., Schlax, M. G., Naggar, K. E., & Siwertz, N. (1998). Geographical Variability of the First Baroclinic Rossby Radius of Deformation. *Journal of Physical Oceanography*, *28*(3), 433–460. https://doi.org/10.1175/1520-0485(1998)028<0433:GVOTFB>2.0.CO;2

Chelton, D. B., Schlax, M. G., & Samelson, R. M. (2011). Global observations of nonlinear mesoscale eddies. *Progress in Oceanography*, *91*(2), 167–216. https://doi.org/10.1016/j.pocean.2011.01.002

Chen, C., Wang, G., Xie, S.-P., & Liu, W. (2019). Why Does Global Warming Weaken the Gulf Stream but Intensify the Kuroshio? *Journal of Climate*, *32*(21), 7437–7451. https://doi.org/10.1175/JCLI-D-18-0895.1

Cheney, R. E., Marsh, J. G., & Beckley, B. D. (1983). Global mesoscale variability from collinear tracks of SEASAT altimeter data. *Journal of Geophysical Research: Oceans*, *88*(C7), 4343–4354. https://doi.org/10.1029/JC088iC07p04343

Chi, L., Wolfe, C. L. P., & Hameed, S. (2021). Has the Gulf Stream Slowed or Shifted in the Altimetry Era? *Geophysical Research Letters*, *48*(14). https://doi.org/10.1029/2021GL093113

Chiessi, C. M., Mulitza, S., Groeneveld, J., Silva, J. B., Campos, M. C., & Gurgel, M. H. C. (2014). Variability of the Brazil Current during the late Holocene. *Palaeogeography, Palaeoclimatology, Palaeoecology*, *415*, 28–36. https://doi.org/10.1016/j.palaeo.2013.12.005

Colman, R. (2003). A comparison of climate feedbacks in general circulation models. *Climate Dynamics*, *20*(7), 865–873. https://doi.org/10.1007/s00382-003-0310-z

Combes, V., & Matano, R. P. (2014). Trends in the Brazil/Malvinas Confluence region. *Geophysical Research Letters*, *41*(24), 8971–8977. https://doi.org/10.1002/2014GL062523

Constantinou, N. C., & Hogg, A. McC. (2019). Eddy Saturation of the Southern Ocean: A Baroclinic Versus Barotropic Perspective. *Geophysical Research Letters*, *46*(21), 12202–12212. https://doi.org/10.1029/2019GL084117

Crews, L., Sundfjord, A., Albretsen, J., & Hattermann, T. (2018). Mesoscale Eddy Activity and Transport in the Atlantic Water Inflow Region North of Svalbard. *Journal of Geophysical Research: Oceans*, *123*(1), 201–215. https://doi.org/10.1002/2017JC013198

D'Agostino, R. B., & Belanger, A. (1990). A Suggestion for Using Powerful and Informative Tests of Normality. *The American Statistician*, *44*(4), 316–321. https://doi.org/10.2307/2684359

Danilov, S. (2013). Ocean modeling on unstructured meshes. *Ocean Modelling*, *69*, 195–210. https://doi.org/10.1016/j.ocemod.2013.05.005

Danilov, S. (2022). On the Resolution of Triangular Meshes. *Journal of Advances in Modeling Earth Systems*, *14*(10), e2022MS003177. https://doi.org/10.1029/2022MS003177

Danilov, S., Juricke, S., Nowak, K., Sidorenko, D., & Wang, Q. (2023). *Extracting spatial spectra using coarse-graining based on implicit filters* [Preprint]. Preprints. https://doi.org/10.22541/essoar.169111691.14930425/v1

Danilov, S., Kivman, G., & Schröter, J. (2004). A finite-element ocean model: Principles and evaluation. *Ocean Modelling*, *6*(2), 125–150. https://doi.org/10.1016/S1463-5003(02)00063-X

Danilov, S., Sidorenko, D., Koldunov, N., Scholz, P., Wang, Q., Rackow, T., Helge, G., & Zampieri, L. (2024). *FESOM2.5_SO3* [Computer software]. Zenodo. https://doi.org/10.5281/zenodo.10476072

Danilov, S., Sidorenko, D., Wang, Q., & Jung, T. (2017). The Finite-volumE Sea ice–Ocean Model (FESOM2). *Geoscientific Model Development*, *10*(2), 765–789. https://doi.org/10.5194/gmd-10-765-2017

Danilov, S., Wang, Q., Timmermann, R., Iakovlev, N., Sidorenko, D., Kimmritz, M., Jung, T., & Schröter, J. (2015). Finite-Element Sea Ice Model (FESIM), version 2. *Geoscientific Model Development*, *8*(6), 1747–1761. https://doi.org/10.5194/gmd-8-1747-2015

De Souza, M. M., Mathis, M., & Pohlmann, T. (2019). Driving mechanisms of the variability and long-term trend of the Brazil–Malvinas confluence during the 21st century. *Climate Dynamics*, *53*(9–10), 6453–6468. https://doi.org/10.1007/s00382-019-04942-7

Ding, M., Lin, P., Liu, H., & Chai, F. (2018). Increased Eddy Activity in the Northeastern Pacific during 1993–2011. *Journal of Climate*, *31*(1), 387–399. https://doi.org/10.1175/JCLI-D-17-0309.1

Docquier, D., Grist, J. P., Roberts, M. J., Roberts, C. D., Semmler, T., Ponsoni, L., Massonnet, F., Sidorenko, D., Sein, D. V., Iovino, D., Bellucci, A., & Fichefet, T. (2019). Impact of model resolution on Arctic sea ice and North Atlantic Ocean heat transport. *Climate Dynamics*, *53*(7), 4989–5017. https://doi.org/10.1007/s00382-019-04840-y

Drews, A., Greatbatch, R. J., Ding, H., Latif, M., & Park, W. (2015). The use of a flow field correction technique for alleviating the North Atlantic cold bias with application to the Kiel Climate Model. *Ocean Dynamics*, *65*(8), 1079–1093. https://doi.org/10.1007/s10236-015-0853-7

Drouin, K. L., Lozier, M. S., & Johns, W. E. (2021). Variability and Trends of the South Atlantic Subtropical Gyre. *Journal of Geophysical Research: Oceans*, *126*(1), e2020JC016405. https://doi.org/10.1029/2020JC016405

Durbin, J., & Watson, G. S. (1950). Testing for Serial Correlation in Least Squares Regression. I. *Biometrika*, *37*(3–4), 409–428. https://doi.org/10.1093/biomet/37.3-4.409

Early, J. J., Samelson, R. M., & Chelton, D. B. (2011). The Evolution and Propagation of Quasigeostrophic Ocean Eddies*. *Journal of Physical Oceanography*, *41*(8), 1535–1555. https://doi.org/10.1175/2011JPO4601.1

Endoh, T., & Hibiya, T. (2001). Numerical simulation of the transient response of the Kuroshio leading to the large meander formation south of Japan. *Journal of Geophysical Research: Oceans*, *106*(C11), 26833–26850. https://doi.org/10.1029/2000JC000776

Eyring, V., Bony, S., Meehl, G. A., Senior, C. A., Stevens, B., Stouffer, R. J., & Taylor, K. E. (2016). Overview of the Coupled Model Intercomparison Project Phase 6 (CMIP6) experimental design and organization. *Geoscientific Model Development*, *9*(5), 1937–1958. https://doi.org/10.5194/gmd-9-1937-2016

Falkowski, P. G., Ziemann, D., Kolber, Z., & Bienfang, P. K. (1991). Role of eddy pumping in enhancing primary production in the ocean. *Nature*, *352*(6330), Article 6330. https://doi.org/10.1038/352055a0

Ferrari, R., Griffies, S. M., Nurser, A. J. G., & Vallis, G. K. (2010). A boundary-value problem for the parameterized mesoscale eddy transport. *Ocean Modelling*, *32*(3–4), 143–156. https://doi.org/10.1016/j.ocemod.2010.01.004

Ferro, C. A. T., Jupp, T. E., Lambert, F. H., Huntingford, C., & Cox, P. M. (2012). Model complexity versus ensemble size: Allocating resources for climate prediction. *Philosophical Transactions of the Royal Society A: Mathematical, Physical and Engineering Sciences*, *370*(1962), 1087–1099. https://doi.org/10.1098/rsta.2011.0307

Fisher, R. A. (1997). The moments of the distribution for normal samples of measures of departure from normality. *Proceedings of the Royal Society of London. Series A, Containing Papers of a Mathematical and Physical Character*, *130*(812), 16–28. https://doi.org/10.1098/rspa.1930.0185

Fleiss, J. L., Levin, B., & Paik, M. C. (2013). *Statistical Methods for Rates and Proportions*. John Wiley & Sons.

Ford, D. J., Tilstone, G. H., Shutler, J. D., Kitidis, V., Sheen, K. L., Dall'Olmo, G., & Orselli, I. B. M. (2023). Mesoscale Eddies Enhance the Air-Sea CO2 Sink in the South Atlantic Ocean. *Geophysical Research Letters*, *50*(9), e2022GL102137. https://doi.org/10.1029/2022GL102137

Fox-Kemper, B., H.T. Hewitt, C. Xiao, G. Aðalgeirsdóttir, S.S. Drijfhout, T.L. Edwards, N.R. Golledge, M. Hemer, R.E. Kopp, G. Krinner, A. Mix, D. Notz, S. Nowicki, I.S. Nurhati, L. Ruiz, J.-B. Sallée, A.B.A. Slangen, & Y. Yu. (2021). Ocean, Cryosphere and Sea Level Change. In Climate Change 2021: The Physical Science Basis. Contribution of Working Group I to the Sixth Assessment Report of the Intergovernmental Panel on Climate Change [Masson-Delmotte, V., P. Zhai, A. Pirani, S.L. Connors, C. Péan, S. Berger, N. Caud, Y. Chen, L. Goldfarb, M.I. Gomis, M. Huang, K. Leitzell, E. Lonnoy, J.B.R. Matthews, T.K. Maycock, T. Waterfield, O. Yelekçi, R. Yu, and B. Zhou (eds.)]. *Cambridge University*

Press, Cambridge, United Kingdom and New York, NY, USA, pp. 1211–1362, https://doi.org10.1017/9781009157896.011.

Frenger, I., Gruber, N., Knutti, R., & Münnich, M. (2013). Imprint of Southern Ocean eddies on winds, clouds and rainfall. *Nature Geoscience*, *6*(8), Article 8. https://doi.org/10.1038/ngeo1863

Frenger, I., Münnich, M., Gruber, N., & Knutti, R. (2015). Southern Ocean eddy phenomenology. *Journal of Geophysical Research: Oceans*, *120*(11), 7413–7449. https://doi.org/10.1002/2015JC011047

Frey, D. I., Morozov, E. G., & Smirnova, D. A. (2023). Sea level anomalies affect the ocean circulation at abyssal depths. *Scientific Reports*, *13*(1), Article 1. https://doi.org/10.1038/s41598-023-48074-9

Frey, W. R., Morrison, A. L., Kay, J. E., Guzman, R., & Chepfer, H. (2018). The Combined Influence of Observed Southern Ocean Clouds and Sea Ice on Top-of-Atmosphere Albedo. *Journal of Geophysical Research: Atmospheres*, *123*(9), 4461–4475. https://doi.org/10.1029/2018JD028505

Friedrichs, D. M., McInerney, J. B. T., Oldroyd, H. J., Lee, W. S., Yun, S., Yoon, S.-T., Stevens, C. L., Zappa, C. J., Dow, C. F., Mueller, D., Sepúlveda Steiner, O., & Forrest, A. L. (2022). Observations of submesoscale eddy-driven heat transport at an ice shelf calving front. *Communications Earth & Environment*, *3*(1), Article 1. https://doi.org/10.1038/s43247-022-00460-3

Frölicher, T. L., Sarmiento, J. L., Paynter, D. J., Dunne, J. P., Krasting, J. P., & Winton, M. (2015). Dominance of the Southern Ocean in Anthropogenic Carbon and Heat Uptake in CMIP5 Models. *Journal of Climate*, *28*(2), 862–886. https://doi.org/10.1175/JCLI-D-14-00117.1

Gaube, P., Chelton, D. B., Samelson, R. M., Schlax, M. G., & O'Neill, L. W. (2015). Satellite Observations of Mesoscale Eddy-Induced Ekman Pumping. *Journal of Physical Oceanography*, *45*(1), 104–132. https://doi.org/10.1175/JPO-D-14-0032.1

Gent, P. R. (2011). The Gent–McWilliams parameterization: 20/20 hindsight. *Ocean Modelling*, *39*(1), 2–9. https://doi.org/10.1016/j.ocemod.2010.08.002

Gent, P. R., & McWilliams, J. C. (1990). Isopycnal Mixing in Ocean Circulation Models. *Journal of Physical Oceanography*, *20*(1), 150–155. https://doi.org/10.1175/1520-0485(1990)020<0150:IMIOCM>2.0.CO;2

Georgiou, S., van der Boog, C. G., Brüggemann, N., Ypma, S. L., Pietrzak, J. D., & Katsman, C. A. (2019). On the interplay between downwelling, deep convection and mesoscale eddies in the Labrador Sea. *Ocean Modelling*, *135*, 56–70. https://doi.org/10.1016/j.ocemod.2019.02.004

Giddy, I., Swart, S., du Plessis, M., Thompson, A. F., & Nicholson, S.-A. (2021). Stirring of Sea-Ice Meltwater Enhances Submesoscale Fronts in the Southern Ocean. *Journal of Geophysical Research: Oceans*, *126*(4), e2020JC016814. https://doi.org/10.1029/2020JC016814

Gill, A. E., Green, J. S. A., & Simmons, A. J. (1974). Energy partition in the large-scale ocean circulation and the production of mid-ocean eddies. *Deep Sea Research and Oceanographic Abstracts*, *21*(7), 499–528. https://doi.org/10.1016/0011-7471(74)90010-2

Gong, D., & Wang, S. (1999). Definition of Antarctic Oscillation index. *Geophysical Research Letters*, *26*(4), 459–462. https://doi.org/10.1029/1999GL900003

Goni, G. J., Bringas, F., & DiNezio, P. N. (2011). Observed low frequency variability of the Brazil Current front. *Journal of Geophysical Research: Oceans*, *116*(C10). https://doi.org/10.1029/2011JC007198

Gordon, A. L. (1986). Interocean exchange of thermocline water. *Journal of Geophysical Research: Oceans*, *91*(C4), 5037–5046. https://doi.org/10.1029/JC091iC04p05037

Graham, J. A., Dinniman, M. S., & Klinck, J. M. (2016). Impact of model resolution for on-shelf heat transport along the West Antarctic Peninsula. *Journal of Geophysical Research: Oceans*, *121*(10), 7880–7897. https://doi.org/10.1002/2016JC011875

Griffies, S. M., Winton, M., Anderson, W. G., Benson, R., Delworth, T. L., Dufour, C. O., Dunne, J. P., Goddard, P., Morrison, A. K., Rosati, A., Wittenberg, A. T., Yin, J., & Zhang, R. (2015). Impacts on Ocean Heat from Transient Mesoscale Eddies in a Hierarchy of Climate Models. *Journal of Climate*, *28*(3), 952–977. https://doi.org/10.1175/JCLI-D-14-00353.1

Grist, J. P., Josey, S. A., Sinha, B., Catto, J. L., Roberts, M. J., & Coward, A. C. (2021). Future Evolution of an Eddy Rich Ocean Associated with Enhanced East Atlantic Storminess in a Coupled Model Projection. *Geophysical Research Letters*, *48*(7), e2021GL092719. https://doi.org/10.1029/2021GL092719

Gruber, N., Clement, D., Carter, B. R., Feely, R. A., van Heuven, S., Hoppema, M., Ishii, M., Key, R. M., Kozyr, A., Lauvset, S. K., Lo Monaco, C., Mathis, J. T., Murata, A., Olsen, A., Perez, F. F., Sabine, C. L., Tanhua, T., & Wanninkhof, R. (2019). The oceanic sink for anthropogenic CO2 from 1994 to 2007. *Science*, *363*(6432), 1193–1199. https://doi.org/10.1126/science.aau5153

Gruber, N., Lachkar, Z., Frenzel, H., Marchesiello, P., Münnich, M., McWilliams, J. C., Nagai, T., & Plattner, G.-K. (2011). Eddy-induced reduction of biological production in eastern boundary upwelling systems. *Nature Geoscience*, *4*(11), Article 11. https://doi.org/10.1038/ngeo1273

Haarsma, R. J., Roberts, M. J., Vidale, P. L., Senior, C. A., Bellucci, A., Bao, Q., Chang, P., Corti, S., Fučkar, N. S., Guemas, V., von Hardenberg, J., Hazeleger, W., Kodama, C., Koenigk, T., Leung, L. R., Lu, J., Luo, J.-J., Mao, J., Mizielinski, M. S., … von Storch, J.-S. (2016). High Resolution Model Intercomparison Project (HighResMIP v1.0) for CMIP6. *Geoscientific Model Development*, *9*(11), 4185–4208. https://doi.org/10.5194/gmd-9-4185-2016

Häkkinen, S. (1986). Coupled ice-ocean dynamics in the marginal ice zones: Upwelling/downwelling and eddy generation. *Journal of Geophysical Research: Oceans*, *91*(C1), 819–832. https://doi.org/10.1029/JC091iC01p00819

Hallberg, R. (2013). Using a resolution function to regulate parameterizations of oceanic mesoscale eddy effects. *Ocean Modelling*, *72*, 92–103. https://doi.org/10.1016/j.ocemod.2013.08.007

Hallberg, R., & Gnanadesikan, A. (2006). The Role of Eddies in Determining the Structure and Response of the Wind-Driven Southern Hemisphere Overturning: Results from the Modeling Eddies in the Southern Ocean (MESO) Project. *Journal of Physical Oceanography*, *36*(12), 2232–2252. https://doi.org/10.1175/JPO2980.1

Haumann, F. A., Gruber, N., Münnich, M., Frenger, I., & Kern, S. (2016). Sea-ice transport driving Southern Ocean salinity and its recent trends. *Nature*, *537*(7618), Article 7618. https://doi.org/10.1038/nature19101

Hewitt, H. T., Bell, M. J., Chassignet, E. P., Czaja, A., Ferreira, D., Griffies, S. M., Hyder, P., McClean, J. L., New, A. L., & Roberts, M. J. (2017). Will high-resolution global ocean models benefit coupled predictions on short-range to climate timescales? *Ocean Modelling*, *120*, 120–136. https://doi.org/10.1016/j.ocemod.2017.11.002

Hewitt, H. T., Roberts, M., Mathiot, P., Biastoch, A., Blockley, E., Chassignet, E. P., Fox-Kemper, B., Hyder, P., Marshall, D. P., Popova, E., Treguier, A.-M., Zanna, L., Yool, A., Yu, Y., Beadling, R., Bell, M., Kuhlbrodt, T., Arsouze, T., Bellucci, A., … Zhang, Q. (2020). Resolving and Parameterising the Ocean Mesoscale in Earth System Models. *Current Climate Change Reports*, *6*(4), 137–152. https://doi.org/10.1007/s40641-020-00164-w

Heywood, K. J., & McDonagh, E. L. (1994). Eddy kinetic energy of the North Atlantic subpolar gyre from satellite altimetry. *Journal of Geophysical Research*, *99*(C11), 22525–22539. http://www.scopus.com/inward/record.url?scp=0028555042&partnerID=8YFLogxK

Hobday, A. J., & Hartog, J. R. (2014). Derived Ocean Features for Dynamic Ocean Management. *Oceanography*, *27*(4), 134–145. https://www.jstor.org/stable/24862218

Hogg, A. McC., Meredith, M. P., Chambers, D. P., Abrahamsen, E. P., Hughes, C. W., & Morrison, A. K. (2015). Recent trends in the Southern Ocean eddy field. *Journal of Geophysical Research: Oceans*, *120*(1), 257–267. https://doi.org/10.1002/2014JC010470

Holland, D. M. (2001). Explaining the Weddell Polynya—A Large Ocean Eddy Shed at Maud Rise. *Science*, *292*(5522), 1697–1700. https://doi.org/10.1126/science.1059322

Horvat, C., Tziperman, E., & Campin, J.-M. (2016). Interaction of sea ice floe size, ocean eddies, and sea ice melting. *Geophysical Research Letters*, *43*(15), 8083–8090. https://doi.org/10.1002/2016GL069742

Hsu, A. C., Boustany, A. M., Roberts, J. J., Chang, J.-H., & Halpin, P. N. (2015). Tuna and swordfish catch in the U.S. northwest Atlantic longline fishery in relation to mesoscale eddies. *Fisheries Oceanography*, *24*(6), 508–520. https://doi.org/10.1111/fog.12125

Huot, P.-V., Kittel, C., Fichefet, T., Jourdain, N. C., & Fettweis, X. (2022). Effects of ocean mesoscale eddies on atmosphere–sea ice–ocean interactions off Adélie Land, East Antarctica. *Climate Dynamics*, *59*(1), 41–60. https://doi.org/10.1007/s00382-021-06115-x

Hurlburt, H. E., & Hogan, P. J. (2008). The Gulf Stream pathway and the impacts of the eddy-driven abyssal circulation and the Deep Western Boundary Current. *Dynamics of Atmospheres and Oceans*, *45*(3), 71–101. https://doi.org/10.1016/j.dynatmoce.2008.06.002

Irving, D., Hobbs, W., Church, J., & Zika, J. (2021). A Mass and Energy Conservation Analysis of Drift in the CMIP6 Ensemble. *Journal of Climate*, *34*(8), 3157–3170. https://doi.org/10.1175/JCLI-D-20-0281.1

Johnson, G. C. (2008). Quantifying Antarctic Bottom Water and North Atlantic Deep Water volumes. *Journal of Geophysical Research: Oceans*, *113*(C5). https://doi.org/10.1029/2007JC004477

Jungclaus, J. H., Lorenz, S. J., Schmidt, H., Brovkin, V., Brüggemann, N., Chegini, F., Crüger, T., De-Vrese, P., Gayler, V., Giorgetta, M. A., Gutjahr, O., Haak, H., Hagemann, S., Hanke, M., Ilyina, T., Korn, P., Kröger, J., Linardakis, L., Mehlmann, C., … Claussen, M. (2022). The ICON Earth System Model Version 1.0. *Journal of Advances in Modeling Earth Systems*, *14*(4), e2021MS002813. https://doi.org/10.1029/2021MS002813

Kawabe, M. (1995). Variations of Current Path, Velocity, and Volume Transport of the Kuroshio in Relation with the Large Meander. *Journal of Physical Oceanography*, *25*(12), 3103–3117. https://doi.org/10.1175/1520-0485(1995)025<3103:VOCPVA>2.0.CO;2

Khan, H. N., Hounshell, D. A., & Fuchs, E. R. H. (2018). Science and research policy at the end of Moore's law. *Nature Electronics*, *1*(1), Article 1. https://doi.org/10.1038/s41928-017-0005-9

Knorr, G., & Lohmann, G. (2003). Southern Ocean origin for the resumption of Atlantic thermohaline circulation during deglaciation. *Nature*, *424*(6948), Article 6948. https://doi.org/10.1038/nature01855

Koldunov, N. V., Aizinger, V., Rakowsky, N., Scholz, P., Sidorenko, D., Danilov, S., & Jung, T. (2019). Scalability and some optimization of the Finite-volumE Sea ice–Ocean Model, Version 2.0 (FESOM2). *Geoscientific Model Development*, *12*(9), 3991–4012. https://doi.org/10.5194/gmd-12-3991-2019

Kozlov, I. E., Artamonova, A. V., Manucharyan, G. E., & Kubryakov, A. A. (2019). Eddies in the Western Arctic Ocean From Spaceborne SAR Observations Over Open Ocean and Marginal Ice Zones. *Journal of Geophysical Research: Oceans*, *124*(9), 6601–6616. https://doi.org/10.1029/2019JC015113

Lachkar, Z., Orr, J. C., Dutay, J. C., & Delecluse, P. (2009). On the role of mesoscale eddies in the ventilation of Antarctic intermediate water. *Deep-Sea Research Part I: Oceanographic Research Papers*, *56*(6), 909–925. https://doi.org/10.1016/j.dsr.2009.01.013

Lagerloef, G. S. E., Mitchum, G. T., Lukas, R. B., & Niiler, P. P. (1999). Tropical Pacific near-surface currents estimated from altimeter, wind, and drifter data. *Journal of Geophysical Research: Oceans*, *104*(C10), 23313–23326. https://doi.org/10.1029/1999JC900197

Landschützer, P., Gruber, N., Haumann, F. A., Rödenbeck, C., Bakker, D. C. E., van Heuven, S., Hoppema, M., Metzl, N., Sweeney, C., Takahashi, T., Tilbrook, B., & Wanninkhof, R. (2015). The reinvigoration of the Southern Ocean carbon sink. *Science*, *349*(6253), 1221–1224. https://doi.org/10.1126/science.aab2620

Large, W. G., McWilliams, J. C., & Doney, S. C. (1994). Oceanic vertical mixing: A review and a model with a nonlocal boundary layer parameterization. *Reviews of Geophysics*, *32*(4), 363–403. https://doi.org/10.1029/94RG01872

Li, S., Zhang, F., Wang, S., Wang, Y., & Yang, S. (2020). Constructing the three-dimensional structure of an anticyclonic eddy with the optimal configuration of an underwater glider network. *Applied Ocean Research*, *95*, 101893. https://doi.org/10.1016/j.apor.2019.101893

Li, X., Wang, Q., Danilov, S., Koldunov, N., Liu, C., Müller, V., Sidorenko, D., & Jung, T. (2024). Eddy activity in the Arctic Ocean projected to surge in a warming world. *Nature Climate Change*, 1–7. https://doi.org/10.1038/s41558-023-01908-w

Liu, H., Song, Z., Wang, X., & Misra, V. (2022). An ocean perspective on CMIP6 climate model evaluations. *Deep Sea Research Part II: Topical Studies in Oceanography*, *201*, 105120. https://doi.org/10.1016/j.dsr2.2022.105120

Lumpkin, R., & Garzoli, S. (2011). Interannual to decadal changes in the western South Atlantic's surface circulation. *Journal of Geophysical Research: Oceans*, *116*(C1). https://doi.org/10.1029/2010JC006285

Luo, F., Ying, J., Liu, T., & Chen, D. (2023). Origins of Southern Ocean warm sea surface temperature bias in CMIP6 models. *Npj Climate and Atmospheric Science*, *6*(1), Article 1. https://doi.org/10.1038/s41612-023-00456-6

Lutjeharms, J. R. E., & Ballegooyen, R. C. V. (1988). The Retroflection of the Agulhas Current. *Journal of Physical Oceanography*, *18*(11), 1570–1583. https://doi.org/10.1175/1520-0485(1988)018<1570:TROTAC>2.0.CO;2

MacGilchrist, G. A., Marshall, D. P., Johnson, H. L., Lique, C., & Thomas, M. (2017). Characterizing the chaotic nature of ocean ventilation. *Journal of Geophysical Research: Oceans*, *122*(9), 7577–7594. https://doi.org/10.1002/2017JC012875

Mahadevan, A., Thomas, L., & Tandon, A. (2008). Comment on "Eddy/Wind Interactions Stimulate Extraordinary Mid-Ocean Plankton Blooms". *Science (New York, N.Y.)*, *320*, 448; author reply 448. https://doi.org/10.1126/science.1152111

Malan, N., Archer, M., Roughan, M., Cetina-Heredia, P., Hemming, M., Rocha, C., Schaeffer, A., Suthers, I., & Queiroz, E. (2020). Eddy-Driven Cross-Shelf Transport in the East Australian Current Separation Zone. *Journal of Geophysical Research: Oceans*, *125*(2), e2019JC015613. https://doi.org/10.1029/2019JC015613

Manley, T. O., & Hunkins, K. (1985). Mesoscale eddies of the Arctic Ocean. *Journal of Geophysical Research: Oceans*, *90*(C3), 4911–4930. https://doi.org/10.1029/JC090iC03p04911

Manucharyan, G. E., & Thompson, A. F. (2022). Heavy footprints of upper-ocean eddies on weakened Arctic sea ice in marginal ice zones. *Nature Communications*, *13*(1), Article 1. https://doi.org/10.1038/s41467-022-29663-0

Manucharyan, G. E., & Timmermans, M.-L. (2013). Generation and Separation of Mesoscale Eddies from Surface Ocean Fronts. *Journal of Physical Oceanography*, *43*(12), 2545–2562. https://doi.org/10.1175/JPO-D-13-094.1

Marshall, G. J. (2003). Trends in the Southern Annular Mode from Observations and Reanalyses. *Journal of Climate*, *16*(24), 4134–4143. https://doi.org/10.1175/1520-0442(2003)016<4134:TITSAM>2.0.CO;2

Martínez-Moreno, J., Hogg, A. McC., England, M. H., Constantinou, N. C., Kiss, A. E., & Morrison, A. K. (2021). Global changes in oceanic mesoscale currents over the satellite altimetry record. *Nature Climate Change*, *11*(5), 397–403. https://doi.org/10.1038/s41558-021-01006-9

Martínez-Moreno, J., Hogg, A. McC., Kiss, A. E., Constantinou, N. C., & Morrison, A. K. (2019). Kinetic Energy of Eddy-Like Features From Sea Surface Altimetry. *Journal of Advances in Modeling Earth Systems*, *11*(10), 3090–3105. https://doi.org/10.1029/2019MS001769

Marzocchi, A., Hirschi, J. J.-M., Holliday, N. P., Cunningham, S. A., Blaker, A. T., & Coward, A. C. (2015). The North Atlantic subpolar circulation in an eddy-resolving global ocean

model. *Journal of Marine Systems*, *142*, 126–143. https://doi.org/10.1016/j.jmarsys.2014.10.007

Masson-Delmotte, V., Zhai, P., Pirani, A., Connors, S. L., Péan, C., Berger, S., Caud, N., Chen, Y., Goldfarb, L., Gomis, M. I., Huang, M., Leitzell, K., Lonnoy, E., Matthews, J. B. R., Maycock, T. K., Waterfield, T., Yelekçi, Ö., Yu, R., & Zhou, B. (Eds.). (2021). Summary for policymakers. In *Climate Change 2021: The Physical Science Basis. Contribution of Working Group I to the Sixth Assessment Report of the Intergovernmental Panel on Climate Change* (pp. 3–32). Cambridge University Press. https://doi.org/10.1017/9781009157896.001

McGuffie, K., & Henderson-Sellers, A. (2001). Forty years of numerical climate modelling. *International Journal of Climatology*, *21*(9), 1067–1109. https://doi.org/10.1002/joc.632

Meier, K. J. F., Bahr, A., Chiessi, C. M., Albuquerque, A. L., Raddatz, J., & Friedrich, O. (2021). Role of the Tropical Atlantic for the Interhemispheric Heat Transport During the Last Deglaciation. *Paleoceanography and Paleoclimatology*, *36*(5), e2020PA004107. https://doi.org/10.1029/2020PA004107

Menard, Y. (1983). Observations of eddy fields in the northwest Atlantic and northwest Pacific by SEASAT altimeter data. *Journal of Geophysical Research: Oceans*, *88*(C3), 1853–1866. https://doi.org/10.1029/JC088iC03p01853

Meneghello, G., Marshall, J., Lique, C., Isachsen, P. E., Doddridge, E., Campin, J.-M., Regan, H., & Talandier, C. (2020). Genesis and Decay of Mesoscale Baroclinic Eddies in the Seasonally Ice-Covered Interior Arctic Ocean. *Journal of Physical Oceanography*, *51*(1), 115–129. https://doi.org/10.1175/JPO-D-20-0054.1

Moreton, S. M., Ferreira, D., Roberts, M. J., & Hewitt, H. T. (2020). Evaluating surface eddy properties in coupled climate simulations with 'eddy-present' and 'eddy-rich' ocean resolution. *Ocean Modelling*, *147*, 101567. https://doi.org/10.1016/j.ocemod.2020.101567

Morozov, E. G., Frey, D. I., Polukhin, A. A., Krechik, V. A., Artemiev, V. A., Gavrikov, A. V., Kasian, V. V., Sapozhnikov, F. V., Gordeeva, N. V., & Kobylyansky, S. G. (2020). Mesoscale Variability of the Ocean in the Northern Part of the Weddell Sea. *Oceanology*, *60*(5), 573–588. https://doi.org/10.1134/S0001437020050173

Moss, R. H., Edmonds, J. A., Hibbard, K. A., Manning, M. R., Rose, S. K., van Vuuren, D. P., Carter, T. R., Emori, S., Kainuma, M., Kram, T., Meehl, G. A., Mitchell, J. F. B., Nakicenovic, N., Riahi, K., Smith, S. J., Stouffer, R. J., Thomson, A. M., Weyant, J. P., & Wilbanks, T. J. (2010). The next generation of scenarios for climate change research and assessment. *Nature*, *463*(7282), Article 7282. https://doi.org/10.1038/nature08823

Munday, D. R., Johnson, H. L., & Marshall, D. P. (2013). Eddy Saturation of Equilibrated Circumpolar Currents. *Journal of Physical Oceanography*, *43*(3), 507–532. https://doi.org/10.1175/JPO-D-12-095.1

Nakano, H., Tsujino, H., & Sakamoto, K. (2013). Tracer transport in cold-core rings pinched off from the Kuroshio Extension in an eddy-resolving ocean general circulation model. *Journal of Geophysical Research: Oceans*, *118*(10), 5461–5488. https://doi.org/10.1002/jgrc.20375

Nøst, O. A., Biuw, M., Tverberg, V., Lydersen, C., Hattermann, T., Zhou, Q., Smedsrud, L. H., & Kovacs, K. M. (2011). Eddy overturning of the Antarctic Slope Front controls glacial melting in the Eastern Weddell Sea. *Journal of Geophysical Research: Oceans*, *116*(C11). https://doi.org/10.1029/2011JC006965

Ogata, T., & Masumoto, Y. (2011). Interannual modulation and its dynamics of the mesoscale eddy variability in the southeastern tropical Indian Ocean. *Journal of Geophysical Research: Oceans*, *116*(C5). https://doi.org/10.1029/2010JC006490

Okubo, A. (1970). Horizontal dispersion of floatable particles in the vicinity of velocity singularities such as convergences. *Deep Sea Research and Oceanographic Abstracts*, *17*(3), 445–454. https://doi.org/10.1016/0011-7471(70)90059-8

Olson, D. B., & Evans, R. H. (1986). Rings of the Agulhas current. *Deep Sea Research Part A. Oceanographic Research Papers*, *33*(1), 27–42. https://doi.org/10.1016/0198-0149(86)90106-8

O'Neill, B. C., Kriegler, E., Ebi, K. L., Kemp-Benedict, E., Riahi, K., Rothman, D. S., van Ruijven, B. J., van Vuuren, D. P., Birkmann, J., Kok, K., Levy, M., & Solecki, W. (2017). The roads ahead: Narratives for shared socioeconomic pathways describing world futures in the 21st century. *Global Environmental Change*, *42*, 169–180. https://doi.org/10.1016/j.gloenvcha.2015.01.004

O'Neill, B. C., Tebaldi, C., van Vuuren, D. P., Eyring, V., Friedlingstein, P., Hurtt, G., Knutti, R., Kriegler, E., Lamarque, J.-F., Lowe, J., Meehl, G. A., Moss, R., Riahi, K., & Sanderson, B. M. (2016). The Scenario Model Intercomparison Project (ScenarioMIP) for CMIP6. *Geoscientific Model Development*, *9*(9), 3461–3482. https://doi.org/10.5194/gmd-9-3461-2016

Orsi, A. H., Johnson, G. C., & Bullister, J. L. (1999). Circulation, mixing, and production of Antarctic Bottom Water. *Progress in Oceanography*, *43*(1), 55–109. https://doi.org/10.1016/S0079-6611(99)00004-X

Oschlies, A. (2002). Can eddies make ocean deserts bloom? *Global Biogeochemical Cycles*, *16*(4), 53-1-53–11. https://doi.org/10.1029/2001GB001830

Oschlies, A., & Garçon, V. (1998). Eddy-induced enhancement of primary production in a model of the North Atlantic Ocean. *Nature*, *394*(6690), Article 6690. https://doi.org/10.1038/28373

Patara, L., Böning, C. W., & Biastoch, A. (2016). Variability and trends in Southern Ocean eddy activity in 1/12° ocean model simulations. *Geophysical Research Letters*, *43*(9), 4517–4523. https://doi.org/10.1002/2016GL069026

Pauling, A. G., Smith, I. J., Langhorne, P. J., & Bitz, C. M. (2017). Time-Dependent Freshwater Input From Ice Shelves: Impacts on Antarctic Sea Ice and the Southern Ocean in an Earth System Model. *Geophysical Research Letters*, *44*(20), 10,454-10,461. https://doi.org/10.1002/2017GL075017

Peeters, F. J. C., Acheson, R., Brummer, G.-J. A., de Ruijter, W. P. M., Schneider, R. R., Ganssen, G. M., Ufkes, E., & Kroon, D. (2004). Vigorous exchange between the Indian and Atlantic oceans at the end of the past five glacial periods. *Nature*, *430*(7000), Article 7000. https://doi.org/10.1038/nature02785

Penduff, T., Juza, M., Barnier, B., Zika, J., Dewar, W. K., Treguier, A.-M., Molines, J.-M., & Audiffren, N. (2011). Sea Level Expression of Intrinsic and Forced Ocean Variabilities at Interannual Time Scales. *Journal of Climate*, *24*(21), 5652–5670. https://doi.org/10.1175/JCLI-D-11-00077.1

Petersen, M. R., Williams, S. J., Maltrud, M. E., Hecht, M. W., & Hamann, B. (2013). A three-dimensional eddy census of a high-resolution global ocean simulation. *Journal of Geophysical Research: Oceans*, *118*(4), 1759–1774. https://doi.org/10.1002/jgrc.20155

Price, J. F., Weller, R. A., & Schudlich, R. R. (1987). Wind-Driven Ocean Currents and Ekman Transport. *Science*, *238*(4833), 1534–1538. https://doi.org/10.1126/science.238.4833.1534

Rackow, T., Danilov, S., Goessling, H. F., Hellmer, H. H., Sein, D. V., Semmler, T., Sidorenko, D., & Jung, T. (2022). Delayed Antarctic sea-ice decline in high-resolution climate change simulations. *Nature Communications*, *13*(1), Article 1. https://doi.org/10.1038/s41467-022-28259-y

Rackow, T., Goessling, H. F., Jung, T., Sidorenko, D., Semmler, T., Barbi, D., & Handorf, D. (2018). Towards multi-resolution global climate modeling with ECHAM6-FESOM. Part II: Climate variability. *Climate Dynamics*, *50*(7), 2369–2394. https://doi.org/10.1007/s00382-016-3192-6

Rai, S., Hecht, M., Maltrud, M., & Aluie, H. (2021). Scale of oceanic eddy killing by wind from global satellite observations. *Science Advances*, *7*(28), eabf4920. https://doi.org/10.1126/sciadv.abf4920

Regan, H., Lique, C., Talandier, C., & Meneghello, G. (2020). Response of Total and Eddy Kinetic Energy to the Recent Spinup of the Beaufort Gyre. *Journal of Physical Oceanography*, *50*(3), 575–594. https://doi.org/10.1175/JPO-D-19-0234.1

Renault, L., Molemaker, M. J., McWilliams, J. C., Shchepetkin, A. F., Lemarié, F., Chelton, D., Illig, S., & Hall, A. (2016). Modulation of Wind Work by Oceanic Current Interaction with the Atmosphere. *Journal of Physical Oceanography*, *46*(6), 1685–1704. https://doi.org/10.1175/JPO-D-15-0232.1

Riahi, K., van Vuuren, D. P., Kriegler, E., Edmonds, J., O'Neill, B. C., Fujimori, S., Bauer, N., Calvin, K., Dellink, R., Fricko, O., Lutz, W., Popp, A., Cuaresma, J. C., Kc, S., Leimbach, M., Jiang, L., Kram, T., Rao, S., Emmerling, J., … Tavoni, M. (2017). The Shared Socioeconomic Pathways and their energy, land use, and greenhouse gas emissions implications: An overview. *Global Environmental Change*, *42*, 153–168. https://doi.org/10.1016/j.gloenvcha.2016.05.009

Ringler, T., Petersen, M., Higdon, R. L., Jacobsen, D., Jones, P. W., & Maltrud, M. (2013). A multi-resolution approach to global ocean modeling. *Ocean Modelling*, *69*, 211–232. https://doi.org/10.1016/j.ocemod.2013.04.010

Roach, C. J., & Speer, K. (2019). Exchange of Water Between the Ross Gyre and ACC Assessed by Lagrangian Particle Tracking. *Journal of Geophysical Research: Oceans*, *124*(7), 4631–4643. https://doi.org/10.1029/2018JC014845

Robertson, R. (2005). Baroclinic and barotropic tides in the Weddell Sea. *Antarctic Science*, *17*(3), 461–474. https://doi.org/10.1017/S0954102005002890

Rouault, M., Penven, P., & Pohl, B. (2009). Warming in the Agulhas Current system since the 1980's. *Geophysical Research Letters*, *36*(12). https://doi.org/10.1029/2009GL037987

Ryan, S., Schröder, M., Huhn, O., & Timmermann, R. (2016). On the warm inflow at the eastern boundary of the Weddell Gyre. *Deep Sea Research Part I: Oceanographic Research Papers*, *107*, 70–81. https://doi.org/10.1016/j.dsr.2015.11.002

Sabine, C. L., Feely, R. A., Gruber, N., Key, R. M., Lee, K., Bullister, J. L., Wanninkhof, R., Wong, C. S., Wallace, D. W. R., Tilbrook, B., Millero, F. J., Peng, T.-H., Kozyr, A., Ono, T., & Rios, A. F. (2004). The Oceanic Sink for Anthropogenic CO2. *Science*, *305*(5682), 367–371. https://doi.org/10.1126/science.1097403

Sallée, J.-B., Matear, R. J., Rintoul, S. R., & Lenton, A. (2012). Localized subduction of anthropogenic carbon dioxide in the Southern Hemisphere oceans. *Nature Geoscience*, *5*(8), Article 8. https://doi.org/10.1038/ngeo1523

Sallée, J.-B., Vignes, L., Minière, A., Steiger, N., Pauthenet, E., Lourenco, A., Speer, K., Lazarevich, P., & Nicholls, K. (2023). Subsurface floats in the Filchner Trough provide first direct under-ice tracks of eddies and circulation on shelf. *EGUsphere*, 1–27. https://doi.org/10.5194/egusphere-2023-2952

Sánchez-Benítez, A., Goessling, H., Pithan, F., Semmler, T., & Jung, T. (2022). The July 2019 European Heat Wave in a Warmer Climate: Storyline Scenarios with a Coupled Model Using Spectral Nudging. *Journal of Climate*, *35*(8), 2373–2390. https://doi.org/10.1175/JCLI-D-21-0573.1

Scholz, P., Sidorenko, D., Danilov, S., Wang, Q., Koldunov, N., Sein, D., & Jung, T. (2022). Assessment of the Finite-VolumE Sea ice–Ocean Model (FESOM2.0) – Part 2: Partial bottom cells, embedded sea ice and vertical mixing library CVMix. *Geoscientific Model Development*, *15*, 335–363. https://doi.org/10.5194/gmd-15-335-2022

Scholz, P., Sidorenko, D., Gurses, O., Danilov, S., Koldunov, N., Wang, Q., Sein, D., Smolentseva, M., Rakowsky, N., & Jung, T. (2019). Assessment of the Finite-volumE Sea ice-Ocean Model (FESOM2.0) – Part 1: Description of selected key model elements and comparison to its predecessor version. *Geoscientific Model Development*, *12*(11), 4875–4899. https://doi.org/10.5194/gmd-12-4875-2019

Schröder, M., & Fahrbach, E. (1999). On the structure and the transport of the eastern Weddell Gyre. *Deep Sea Research Part II: Topical Studies in Oceanography*, *46*(1), 501–527. https://doi.org/10.1016/S0967-0645(98)00112-X

Schwarzkopf, F. U., Biastoch, A., Böning, C. W., Chanut, J., Durgadoo, J. V., Getzlaff, K., Harlaß, J., Rieck, J. K., Roth, C., Scheinert, M. M., & Schubert, R. (2019). The INALT family – a set of high-resolution nests for the Agulhas Current system within global NEMO ocean/sea-ice configurations. *Geoscientific Model Development*, *12*(7), 3329–3355. https://doi.org/10.5194/gmd-12-3329-2019

Sein, D. V., Danilov, S., Biastoch, A., Durgadoo, J. V., Sidorenko, D., Harig, S., & Wang, Q. (2016). Designing variable ocean model resolution based on the observed ocean variability. *Journal of Advances in Modeling Earth Systems*, *8*(2), 904–916. https://doi.org/10.1002/2016MS000650

Sein, D. V., Koldunov, N. V., Danilov, S., Wang, Q., Sidorenko, D., Fast, I., Rackow, T., Cabos, W., & Jung, T. (2017). Ocean Modeling on a Mesh With Resolution Following the Local Rossby

Radius. *Journal of Advances in Modeling Earth Systems*, *9*(7), 2601–2614. https://doi.org/10.1002/2017MS001099

Semmler, T., Danilov, S., Gierz, P., Goessling, H. F., Hegewald, J., Hinrichs, C., Koldunov, N., Khosravi, N., Mu, L., Rackow, T., Sein, D. V., Sidorenko, D., Wang, Q., & Jung, T. (2020). Simulations for CMIP6 With the AWI Climate Model AWI-CM-1-1. *Journal of Advances in Modeling Earth Systems*, *12*(9), e2019MS002009. https://doi.org/10.1029/2019MS002009

Semmler, T., Danilov, S., Rackow, T., Sidorenko, D., Barbi, D., Hegewald, J., Sein, D., Wang, Q., & Jung, T. (2018). *AWI AWI-CM1.1MR model output prepared for CMIP6 CMIP* [dataset]. Earth System Grid Federation. https://doi.org/10.22033/ESGF/CMIP6.359

Semmler, T., Danilov, S., Rackow, T., Sidorenko, D., Barbi, D., Hegewald, J., Sein, D., Wang, Q., & Jung, T. (2022a). *CMIP6_supplemental CMIP AWI AWI-CM-1-1-MR* [dataset]. World Data Center for Climate (WDCC) at DKRZ. https://doi.org/10.26050/WDCC/C6sCMAWAWM

Semmler, T., Danilov, S., Rackow, T., Sidorenko, D., Barbi, D., Hegewald, J., Sein, D., Wang, Q., & Jung, T. (2022b). *CMIP6_supplemental ScenarioMIP AWI AWI-CM-1-1-MR* [dataset]. World Data Center for Climate (WDCC) at DKRZ. https://doi.org/10.26050/WDCC/C6sSPAWAWM

Sidorenko, D., Rackow, T., Jung, T., Semmler, T., Barbi, D., Danilov, S., Dethloff, K., Dorn, W., Fieg, K., Goessling, H. F., Handorf, D., Harig, S., Hiller, W., Juricke, S., Losch, M., Schröter, J., Sein, D. V., & Wang, Q. (2015). Towards multi-resolution global climate modeling with ECHAM6–FESOM. Part I: Model formulation and mean climate. *Climate Dynamics*, *44*(3), 757–780. https://doi.org/10.1007/s00382-014-2290-6

Stewart, A. L., Klocker, A., & Menemenlis, D. (2018). Circum-Antarctic Shoreward Heat Transport Derived From an Eddy- and Tide-Resolving Simulation. *Geophysical Research Letters*, *45*(2), 834–845. https://doi.org/10.1002/2017GL075677

Stewart, A. L., Klocker, A., & Menemenlis, D. (2019). Acceleration and Overturning of the Antarctic Slope Current by Winds, Eddies, and Tides. *Journal of Physical Oceanography*, *49*(8), 2043–2074. https://doi.org/10.1175/JPO-D-18-0221.1

Stewart, A. L., & Thompson, A. F. (2015). Eddy-mediated transport of warm Circumpolar Deep Water across the Antarctic Shelf Break. *Geophysical Research Letters*, *42*(2), 432–440. https://doi.org/10.1002/2014GL062281

Taburet, G., Sanchez-Roman, A., Ballarotta, M., Pujol, M.-I., Legeais, J.-F., Fournier, F., Faugere, Y., & Dibarboure, G. (2019). DUACS DT2018: 25 years of reprocessed sea level altimetry products. *Ocean Science*, *15*(5), 1207–1224. https://doi.org/10.5194/os-15-1207-2019

Thiria, S., Sorror, C., Archambault, T., Charantonis, A., Bereziat, D., Mejia, C., Molines, J.-M., & Crépon, M. (2023). Downscaling of ocean fields by fusion of heterogeneous observations using Deep Learning algorithms. *Ocean Modelling*, *182*, 102174. https://doi.org/10.1016/j.ocemod.2023.102174

Thompson, A. F., Heywood, K. J., Schmidtko, S., & Stewart, A. L. (2014). Eddy transport as a key component of the Antarctic overturning circulation. *Nature Geoscience*, *7*(12), Article 12. https://doi.org/10.1038/ngeo2289

Timmermans, M.-L., Toole, J., Proshutinsky, A., Krishfield, R., & Plueddemann, A. (2008). Eddies in the Canada Basin, Arctic Ocean, Observed from Ice-Tethered Profilers. *Journal of Physical Oceanography*, *38*(1), 133–145. https://doi.org/10.1175/2007JPO3782.1

Toole, J. M., Krishfield, R. A., Timmermans, M.-L., & Proshutinsky, A. (2011). The Ice-Tethered Profiler: Argo of the Arctic. *Oceanography*, *24*(3), 126–135. https://www.jstor.org/stable/24861307

van Sebille, E., Biastoch, A., van Leeuwen, P. J., & de Ruijter, W. P. M. (2009). A weaker Agulhas Current leads to more Agulhas leakage. *Geophysical Research Letters*, *36*(3). https://doi.org/10.1029/2008GL036614

van Westen, R. M., & Dijkstra, H. A. (2021). Ocean eddies strongly affect global mean sea-level projections. *Science Advances*, *7*(15), eabf1674. https://doi.org/10.1126/sciadv.abf1674

von Storch, J.-S., Eden, C., Fast, I., Haak, H., Hernández-Deckers, D., Maier-Reimer, E., Marotzke, J., & Stammer, D. (2012). An Estimate of the Lorenz Energy Cycle for the World Ocean Based on the STORM/NCEP Simulation. *Journal of Physical Oceanography*, *42*(12), 2185–2205. https://doi.org/10.1175/JPO-D-12-079.1

von Storch, J.-S., Haak, H., Hertwig, E., & Fast, I. (2016). Vertical heat and salt fluxes due to resolved and parameterized meso-scale Eddies. *Ocean Modelling*, *108*, 1–19. https://doi.org/10.1016/j.ocemod.2016.10.001

Wallace, L. O., van Wijk, E. M., Rintoul, S. R., & Hally, B. (2020). Bathymetry-Constrained Navigation of Argo Floats Under Sea Ice on the Antarctic Continental Shelf. *Geophysical Research Letters*, *47*(11), e2020GL087019. https://doi.org/10.1029/2020GL087019

Wang, C., Zhang, L., Lee, S.-K., Wu, L., & Mechoso, C. R. (2014). A global perspective on CMIP5 climate model biases. *Nature Climate Change*, *4*(3), Article 3. https://doi.org/10.1038/nclimate2118

Wang, Q., Danilov, S., Sidorenko, D., Timmermann, R., Wekerle, C., Wang, X., Jung, T., & Schröter, J. (2014). The Finite Element Sea Ice-Ocean Model (FESOM) v.1.4: Formulation of an ocean general circulation model. *Geoscientific Model Development*, *7*(2), 663–693. https://doi.org/10.5194/gmd-7-663-2014

Wang, Q., Koldunov, N. V., Danilov, S., Sidorenko, D., Wekerle, C., Scholz, P., Bashmachnikov, I. L., & Jung, T. (2020). Eddy Kinetic Energy in the Arctic Ocean From a Global Simulation With a 1-km Arctic. *Geophysical Research Letters*, *47*(14), e2020GL088550. https://doi.org/10.1029/2020GL088550

Wang, Y., Claus, M., Greatbatch, R. J., & Sheng, J. (2017). Decomposition of the Mean Barotropic Transport in a High-Resolution Model of the North Atlantic Ocean. *Geophysical Research Letters*, *44*(22), 11,537-11,546. https://doi.org/10.1002/2017GL074825

Weijer, W., Cheng, W., Garuba, O. A., Hu, A., & Nadiga, B. T. (2020). CMIP6 Models Predict Significant 21st Century Decline of the Atlantic Meridional Overturning Circulation. *Geophysical Research Letters*, *47*(12), e2019GL086075. https://doi.org/10.1029/2019GL086075

Weijer, W., Ruijter, W. P. M. de, Dijkstra, H. A., & Leeuwen, P. J. van. (1999). Impact of Interbasin Exchange on the Atlantic Overturning Circulation. *Journal of Physical Oceanography*, *29*(9), 2266–2284. https://doi.org/10.1175/1520-0485(1999)029<2266:IOIEOT>2.0.CO;2

Weiss, J. (1991). The dynamics of enstrophy transfer in two-dimensional hydrodynamics. *Physica D: Nonlinear Phenomena*, *48*(2), 273–294. https://doi.org/10.1016/0167-2789(91)90088-Q

Wekerle, C., Wang, Q., von Appen, W.-J., Danilov, S., Schourup-Kristensen, V., & Jung, T. (2017). Eddy-Resolving Simulation of the Atlantic Water Circulation in the Fram Strait With Focus on the Seasonal Cycle. *Journal of Geophysical Research: Oceans*, *122*(11), 8385–8405. https://doi.org/10.1002/2017JC012974

Welch, B. L. (1947). The Generalization of 'Student's' Problem when Several Different Population Variances are Involved. *Biometrika*, *34*(1–2), 28–35. https://doi.org/10.1093/biomet/34.1-2.28

Weller, R. A., Baker, D. J., Glackin, M. M., Roberts, S. J., Schmitt, R. W., Twigg, E. S., & Vimont, D. J. (2019). The Challenge of Sustaining Ocean Observations. *Frontiers in Marine Science*, *6*. https://www.frontiersin.org/articles/10.3389/fmars.2019.00105

White, W. B., & McCreary, J. P. (1976). On the formation of the Kuroshio meander and its relationship to the large-scale ocean circulation. *Deep Sea Research and Oceanographic Abstracts*, *23*(1), 33–47. https://doi.org/10.1016/0011-7471(76)90806-8

Wu, B., Lin, X., & Yu, L. (2021). Poleward Shift of the Kuroshio Extension Front and Its Impact on the North Pacific Subtropical Mode Water in the Recent Decades. *Journal of Physical Oceanography*, *51*(2), 457–474. https://doi.org/10.1175/JPO-D-20-0088.1

Wu, L., Cai, W., Zhang, L., Nakamura, H., Timmermann, A., Joyce, T., McPhaden, M. J., Alexander, M., Qiu, B., Visbeck, M., Chang, P., & Giese, B. (2012). Enhanced warming over the global subtropical western boundary currents. *Nature Climate Change*, *2*(3), Article 3. https://doi.org/10.1038/nclimate1353

Yang, G., Wang, F., Li, Y., & Lin, P. (2013). Mesoscale eddies in the northwestern subtropical Pacific Ocean: Statistical characteristics and three-dimensional structures. *Journal of Geophysical Research: Oceans*, *118*(4), 1906–1925. https://doi.org/10.1002/jgrc.20164

Yang, H., Lohmann, G., Krebs-Kanzow, U., Ionita, M., Shi, X., Sidorenko, D., Gong, X., Chen, X., & Gowan, E. J. (2020). Poleward Shift of the Major Ocean Gyres Detected in a Warming Climate. *Geophysical Research Letters*, *47*(5), e2019GL085868. https://doi.org/10.1029/2019GL085868

Yang, H., Lohmann, G., Wei, W., Dima, M., Ionita, M., & Liu, J. (2016). Intensification and poleward shift of subtropical western boundary currents in a warming climate. *Journal of Geophysical Research: Oceans*, *121*(7), 4928–4945. https://doi.org/10.1002/2015JC011513

Yu, X., Ponte, A. L., Lahaye, N., Caspar-Cohen, Z., & Menemenlis, D. (2021). Geostrophy Assessment and Momentum Balance of the Global Oceans in a Tide- and Eddy-Resolving Model. *Journal of Geophysical Research: Oceans*, *126*(10), e2021JC017422. https://doi.org/10.1029/2021JC017422

Zhang, X., Wang, Q., & Mu, M. (2017). The impact of global warming on Kuroshio Extension and its southern recirculation using CMIP5 experiments with a high-resolution climate model MIROC4h. *Theoretical and Applied Climatology*, *127*(3–4), 815–827. https://doi.org/10.1007/s00704-015-1672-y

Zhang, Y., Zhang, Z., Chen, D., Qiu, B., & Wang, W. (2020). Strengthening of the Kuroshio current by intensifying tropical cyclones. *Science*, *368*(6494), 988–993. https://doi.org/10.1126/science.aax5758

Zhang, Z., Tian, J., Qiu, B., Zhao, W., Chang, P., Wu, D., & Wan, X. (2016). Observed 3D Structure, Generation, and Dissipation of Oceanic Mesoscale Eddies in the South China Sea. *Scientific Reports*, *6*(1), Article 1. https://doi.org/10.1038/srep24349

Zhao, M., Timmermans, M.-L., Cole, S., Krishfield, R., Proshutinsky, A., & Toole, J. (2014). Characterizing the eddy field in the Arctic Ocean halocline. *Journal of Geophysical Research: Oceans*, *119*(12), 8800–8817. https://doi.org/10.1002/2014JC010488

Zhao, M., Timmermans, M.-L., Cole, S., Krishfield, R., & Toole, J. (2016). Evolution of the eddy field in the Arctic Ocean's Canada Basin, 2005–2015. *Geophysical Research Letters*, *43*(15), 8106–8114. https://doi.org/10.1002/2016GL069671

Zhu, C., & Liu, Z. (2020). Weakening Atlantic overturning circulation causes South Atlantic salinity pile-up. *Nature Climate Change*, *10*(11), Article 11. https://doi.org/10.1038/s41558-020-0897-7

Appendix A. Supplementary information for Chapter 2

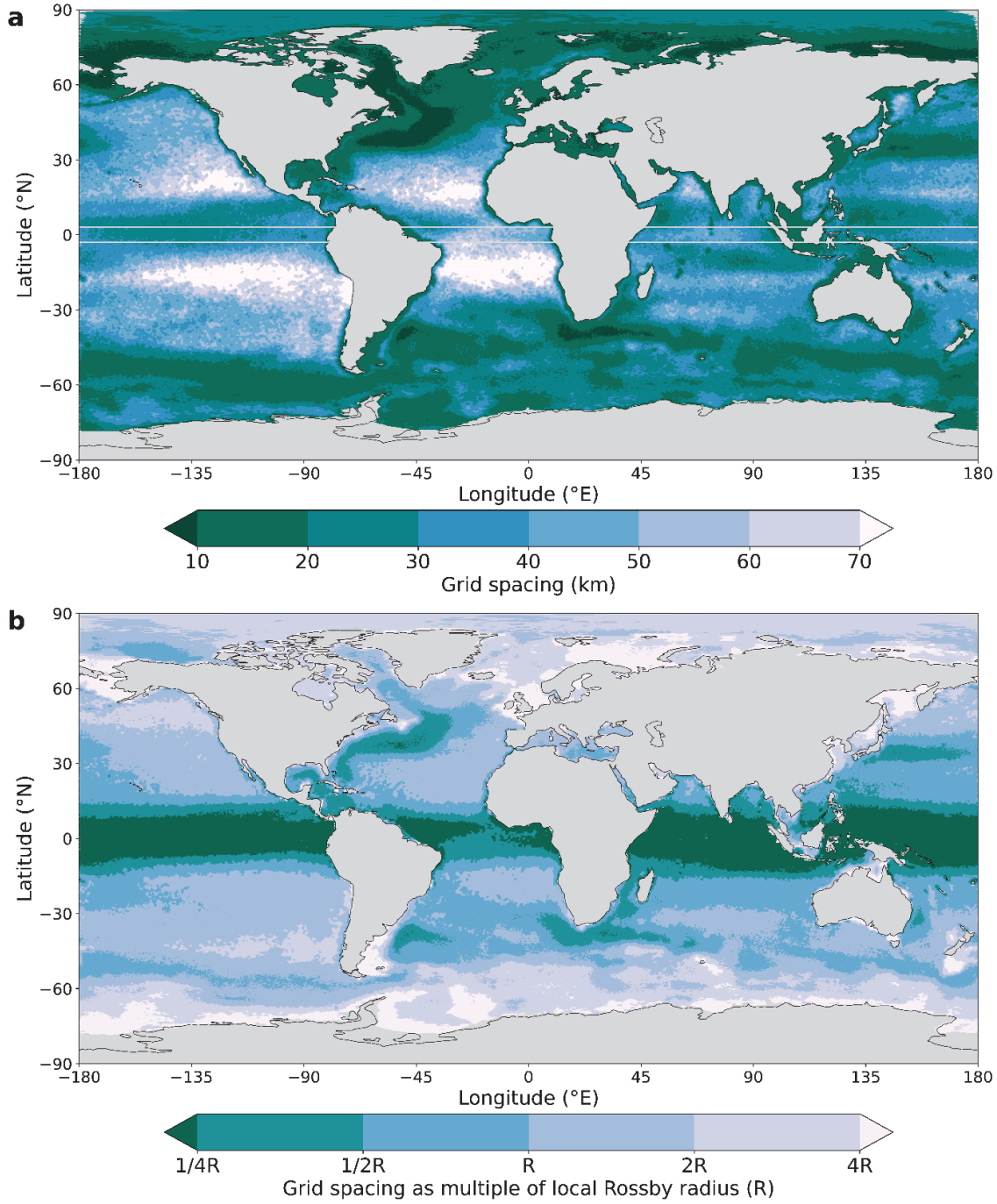

Supplementary Figure A1. Ocean grid resolution in AWI-CM-1-1-MR. Ocean grid resolution in AWI-CM-1-1-MR. **(a)** Grid resolution in units of kilometers. **(b)** Grid resolution relative to the local Rossby radius of deformation.

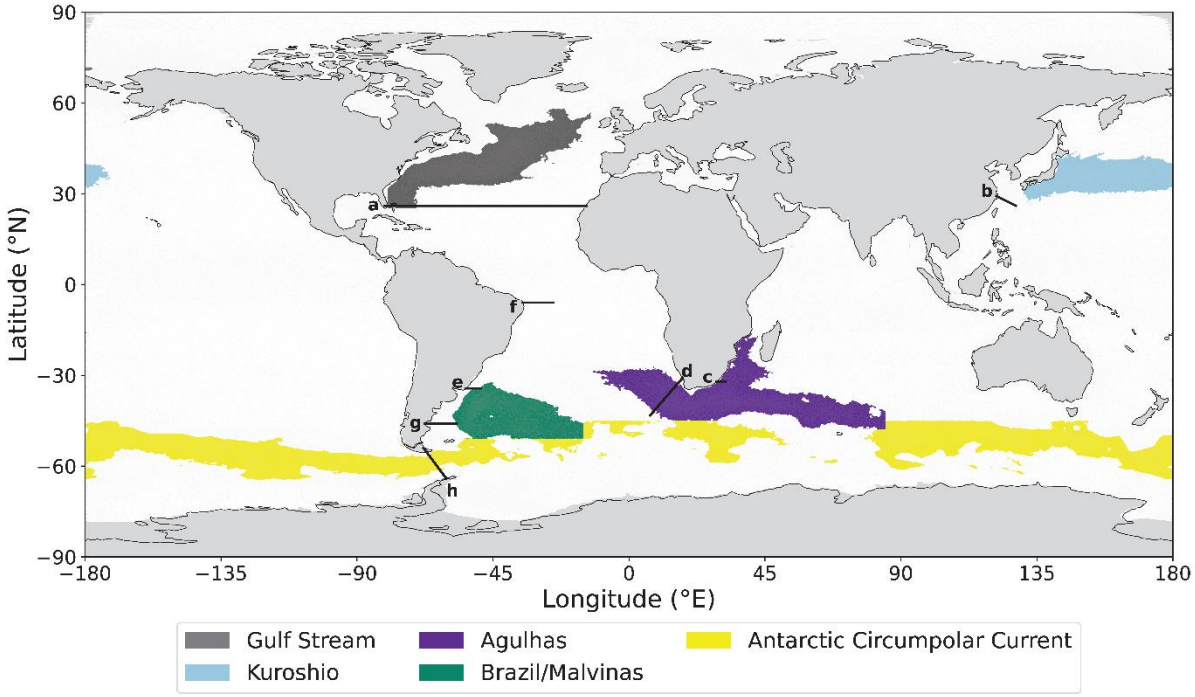

Supplementary Figure A2. Delimitations of ocean basins and transects. Delimitations of ocean basins and transects. The selected ocean basins used for analysis of area-integrated eddy kinetic energy are outlined in color. The transects over which ocean volume transport and AMOC are calculated are defined by black lines. More details regarding transects are available in Supplementary Table A4. **(a)** AMOC. **(b)** Kuroshio Current volume transport. **(c)** Agulhas Current volume transport. **(d)** Agulhas Leakage. **(e)** Brazil Current volume transport. **(f)** North Brazil Current volume transport. **(g)** Malvinas Current volume transport. **(h)** Drake Passage throughflow.

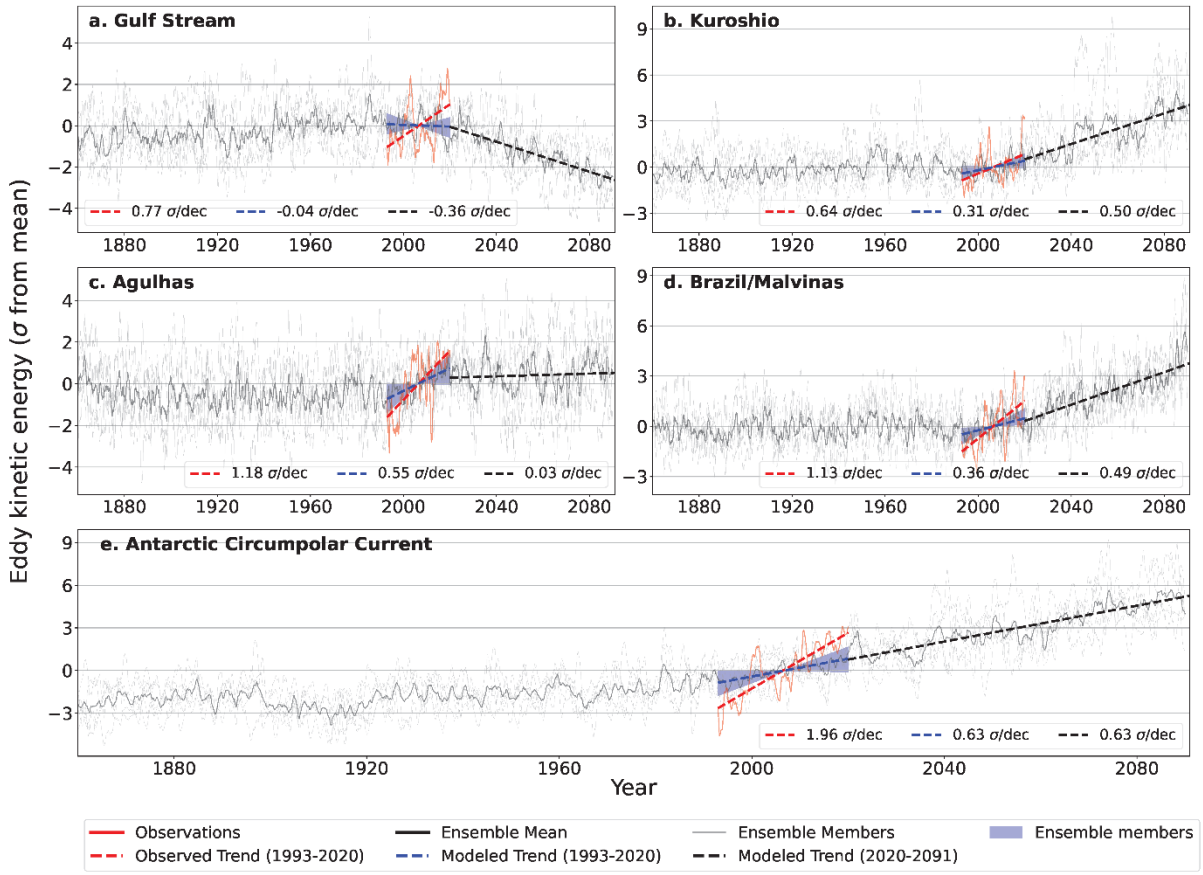

Supplementary Figure A3. Observed and simulated area-integrated regional eddy kinetic energy anomalies and trends. Observed and simulated area-integrated regional eddy kinetic energy anomalies and trends. Eddy kinetic energy anomalies are normalized relative to conditions during the observational period (1993–2020). Overlaid trends show the observed and simulated trends during the observational period (1993–2020), ensemble range of simulated trends during the observational period (1993–2020), and ensemble mean trend after the observational period (2021–2090). **(a)** The Gulf Stream. **(b)** The Kuroshio Current. **(c)** The Agulhas Current. **(d)** The Brazil and Malvinas Currents. **(e)** The Antarctic Circumpolar Current.

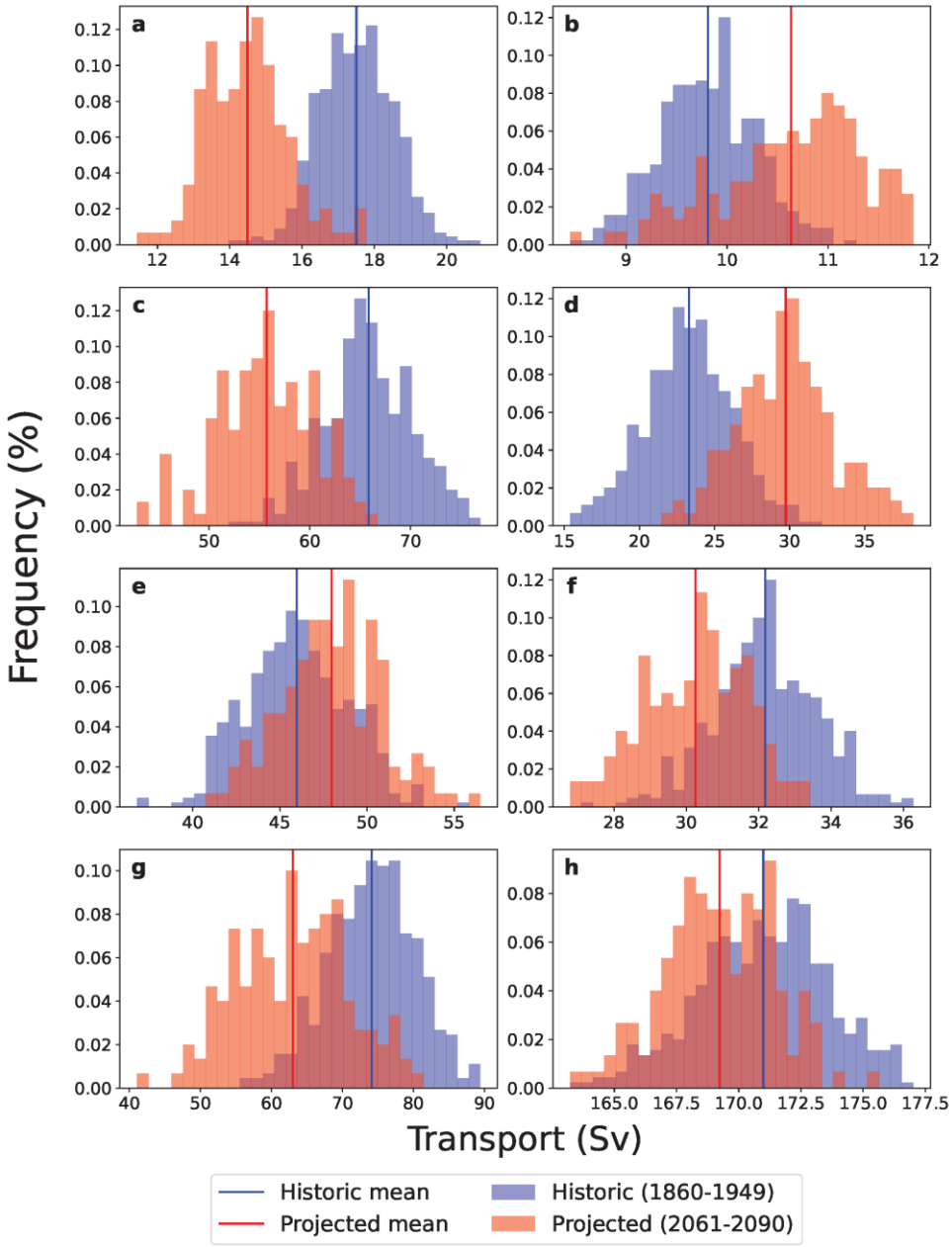

Supplementary Figure A4. Simulated distributions of volume transport and Atlantic meridional overturning circulation. Simulated distributions of volume transport and Atlantic meridional overturning circulation. Distribution of simulated annual volume transport through select ocean currents and Atlantic meridional overturning circulation during historical (1860–1949) and projected (2061–2090) periods. **(a)** Atlantic meridional overturning circulation. **(b)** Kuroshio Current Volume transport. **(c)** Agulhas Current volume transport. **(d)** Agulhas leakage. **(e)** Brazil Current volume transport. **(f)** North Brazil Current volume transport. **(g)** Malvinas Current volume transport. Drake Passage throughflow. Details on the transects used to calculate volume transport can be found in Supplementary Table A4.

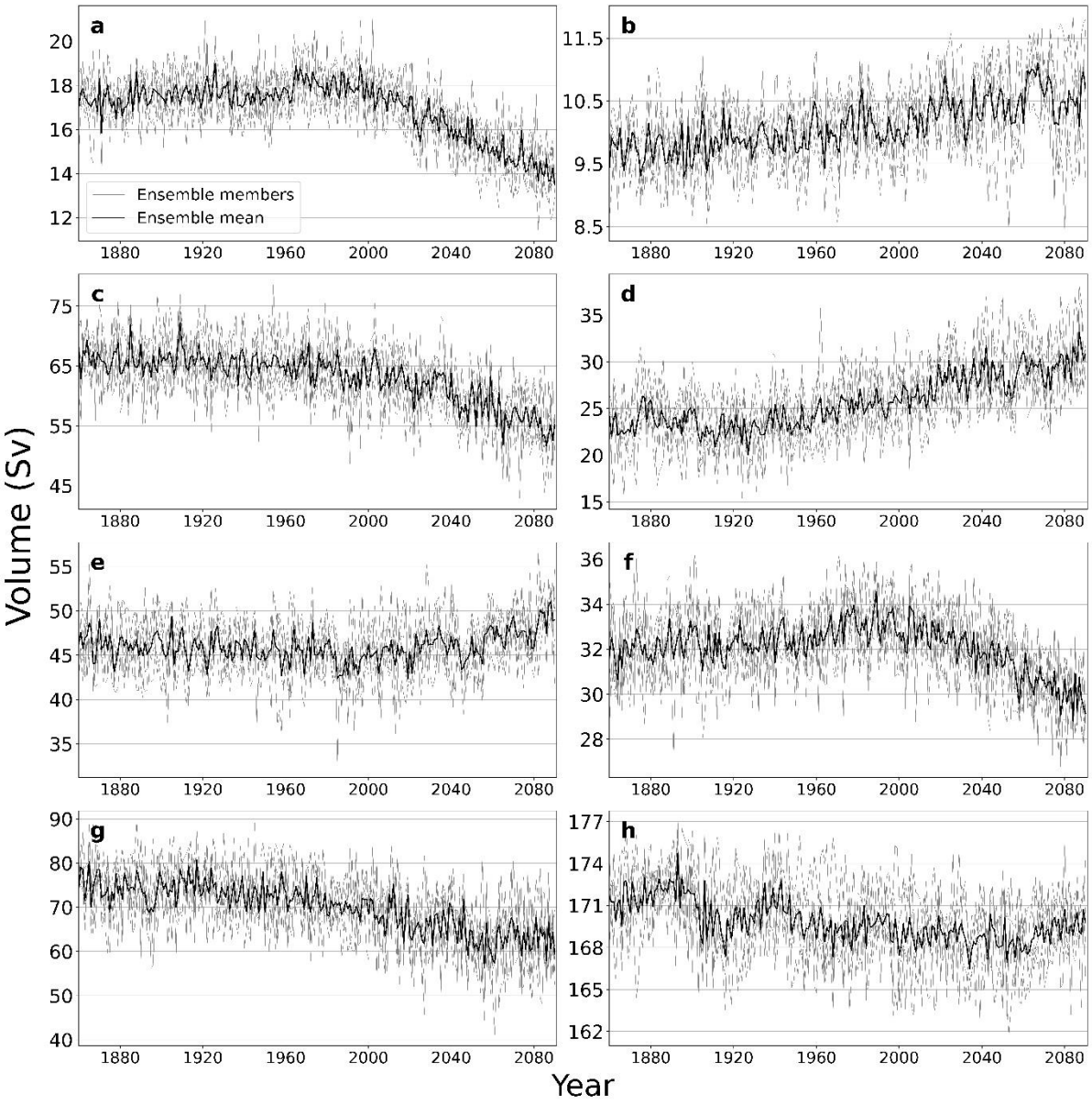

Supplementary Figure A5. Simulated annual volume transport through select ocean currents and Atlantic meridional overturning circulation. Simulated annual volume transport through select ocean currents and Atlantic meridional overturning circulation. **(a)** Atlantic meridional overturning circulation. **(b)** Kuroshio Current Volume transport. **(c)** Agulhas Current volume transport. **(d)** Agulhas leakage. **(e)** Brazil Current volume transport. **(f)** North Brazil Current volume transport. **(g)** Malvinas Current volume transport. Drake Passage throughflow. Details on the transects used, integrated depths, and the definition of Atlantic meridional overturning circulation streamflow can be found in Supplementary Table A4.

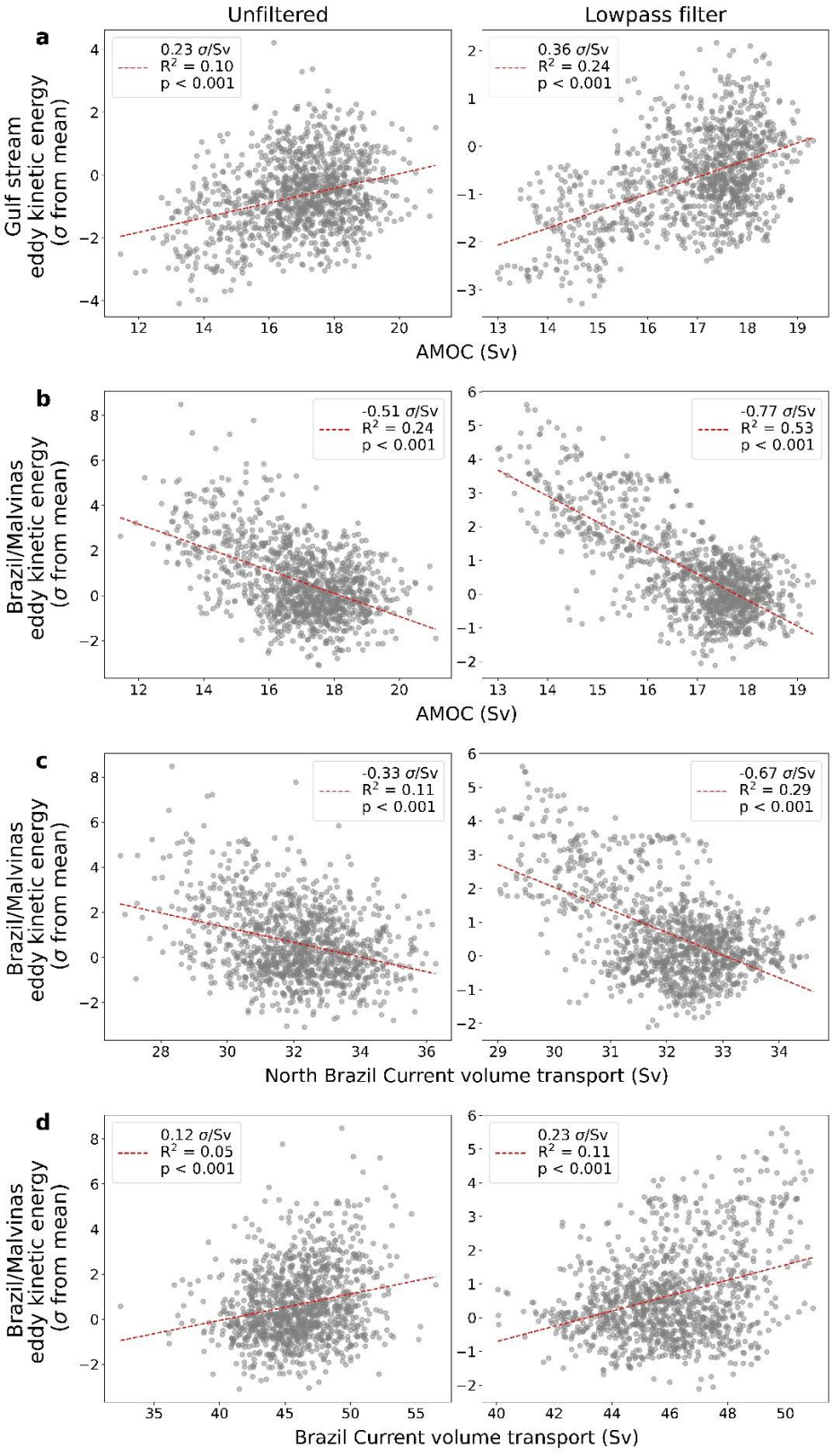

Supplementary Figure A6. See next page for figure caption.

Supplementary Figure A6. Correlation between simulated area-integrated eddy kinetic energy in selected ocean basins and Atlantic meridional overturning circulation or simulated mean annual volume transport. Correlation between simulated area-integrated eddy kinetic energy in selected ocean basins and Atlantic meridional overturning circulation or simulated mean annual volume transport. Correlations are calculated with unfiltered data and with data filtered to remove high-frequency variability with a threshold of 10 years. **(a)** Gulf stream eddy kinetic energy and Atlantic meridional overturning circulation. **(b)** Brazil/Malvinas Current eddy kinetic energy and Atlantic meridional overturning circulation. **(c)** Brazil/Malvinas Current eddy kinetic energy and North Brazil Current volume transport. **(d)** Brazil/Malvinas Current eddy kinetic energy and Brazil Current volume transport.

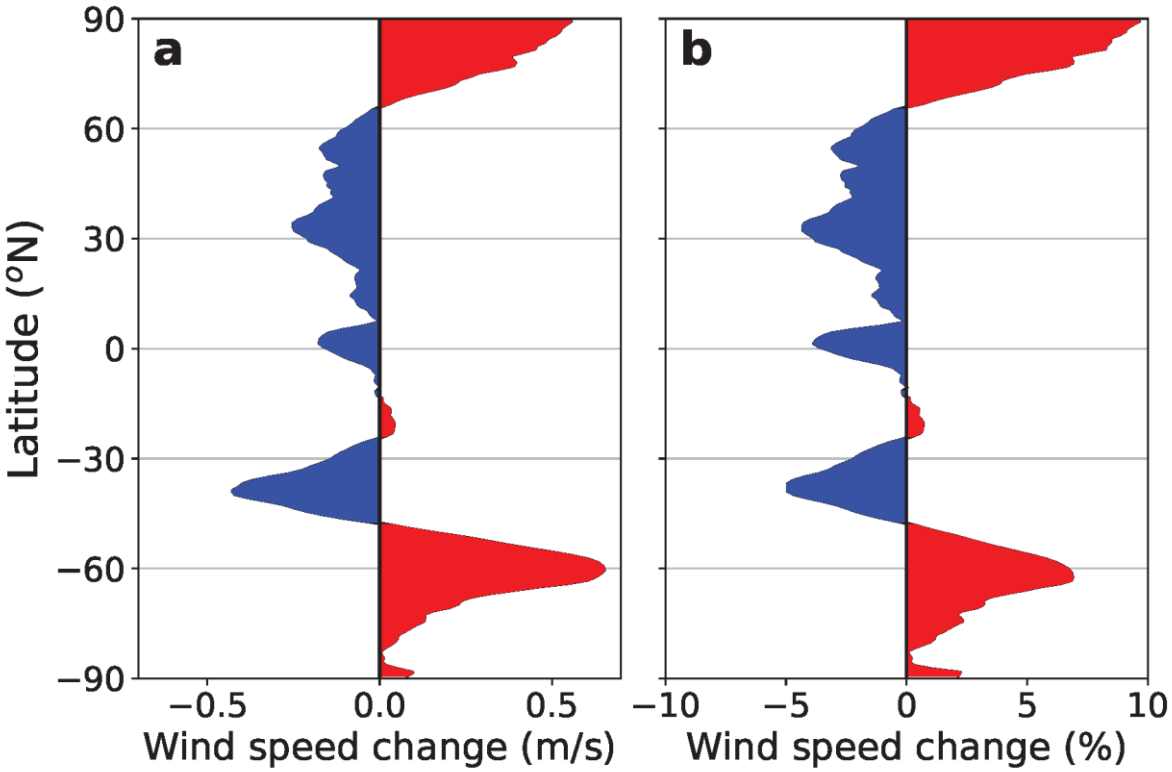

Supplementary Figure A7. Change in simulated zonally averaged global surface wind speed between historical (1860–1949) and projected (2061–2090) periods. Change in simulated zonally averaged global surface wind speed between historical (1860–1949) and projected (2061–2090) periods. **(a)** Wind speed change in meters per second. **(b)** Wind speed change expressed as a percentage of the historical mean.

Supplementary Notes for Chapter 2

1. Atmospheric component configuration and coupling

The atmospheric component of AWI-CM-1-1-MR, ECHAM6.3.04p1 (Stevens et al., 2013), uses a horizontal grid resolution based on spectral truncation at total wavenumber 127, or approximately 100 km horizontal resolution in the tropics and gradually finer resolution towards the poles (Semmler et al., 2020). The different resolutions employed by the atmospheric and oceanic model components result in a loss of spatial detail during coupling between the higher and lower-resolution grids. In the case of AWI-CM-1-1-MR, air-sea fluxes are calculated on the atmospheric grid, as is common practice in CMIP-type models. This effectively results in smoothed fields being passed from the ocean component to the atmospheric component. The damping effects of smoothed coupled fields are a common challenge in coupled climate models with high ocean-to-atmosphere resolution ratio and can affect ocean-atmosphere feedbacks relevant to mesoscale eddy activity (Ma et al., 2016; Jullien et al., 2020). Furthermore, in AWI-CM-1-1-MR absolute wind stress is coupled rather than relative wind stress. The absence of ocean surface currents in the computation can be particularly impactful in the tropics, where ocean surface velocity can be of similar order to the atmospheric velocity. Both of these challenges in coupling may have compensatory effects, and coupling schemes to improve the representation of sub-grid scale variability which is passed to the coarser grid component have been proposed (Rackow & Juricke, 2020). Nonetheless, these are issues that should be acknowledged as systematic model shortcomings in reproducing realistic eddy activity in our simulations.

2. Spin-up information

The AWI-CM-1-1-MR simulations stem from an initial ten-year ocean-only spin-up, followed by a 500-year coupled spin-up, and a pre-industrial control spin-up from which the five ensemble members were branched off at 25-year intervals beginning after 250 model-years. Each ensemble member was then run for a historic period from 1850 to 2014 using prescribed greenhouse gas forcing based on observations before beginning emissions scenario projections for the years 2015–2100.

3. Model inter-comparison

Considering the diversity of the CMIP6 ensemble, it would be advantageous to consider simulations from multiple models when projecting changes in EKE. With this in mind, the CMIP6 ensemble was searched for complementary simulations with comparable resolution and data availability. Most of the CMIP6 ScenarioMIP ensemble (Eyring et al., 2016) relies on

parameterizations of eddy activity, and the highest nominal resolutions in the ScenarioMIP ensemble (25 km) can only be considered eddy-present (Hewitt et al., 2020). Moreover, most simulations do not record, or make publicly available, daily ocean surface velocity or SSH data and many rely on single-member ensembles for each emissions scenario. In particular, high resolution simulations such as HighresMIP (Haarsma et al., 2016) which produce larger datasets as grid resolution increases, tend to be single-member ensembles and record or make publicly available fewer variables at coarser temporal resolution. These datasets do not meet the basic requirements for applying the methods described here, and consequently, this analysis relies exclusively on simulations from AWI-CM-1-1-MR.

4. Data processing

Methodological information regarding the data processing steps performed by Copernicus, including approximation of gridded data from along-track observations and the computation of geostrophic velocity anomalies from sea surface height are publicly available from the Copernicus Marine Environment Monitoring Service (Legeais & Taburet, 2018). In the modeled dataset, the equatorial region between 3 °S and 3 °N, where geostrophic balance breaks down (Lagerloef et al., 1999), is represented by monthly mean data linearly interpolated to 5-day means. In both the modeled and observed datasets, February 29th was removed from the dataset to create a year evenly divisible into five-day means. The observational dataset was remapped to the FESOM grid using bilinear interpolation for a direct comparison of data, and coastal mesh nodes, those adjacent to land, were ignored to avoid boundary issues.

5. Eddy kinetic energy calculation considerations

Typically, the time varying component of ocean flow is separated from mean conditions via Reynolds decomposition: subtracting the mean conditions during a reference period from the larger dataset and interpreting the resulting anomalies as the time varying component. In many applications of time series analysis, such as assessing changes in mean conditions, a reference period is appropriate to represent the historic mean state of a variable. However, if anomalies are intended to represent variability from a mean state and that mean state is changing, the reference period approach fails when mean conditions change to the point that the reference period mean is no longer representative of typical conditions. In the context of climate change, the potential for the mean state of ocean flow to shift must be considered; ocean gyres are expected to shift poleward as warming continues (Wu et al., 2012; Yang et al., 2016; 2020), AMOC decline has been theorized and predicted by many studies (Latif et al., 2004; Rahmstorf et al., 2015; Lique et al.,

2018; Boers, 2021), and global ocean circulation appears to be accelerating in general (Hu et al., 2019). Therefore, changes in the mean flow of the ocean must be accounted for when producing anomalies for EKE calculation, prompting the use of a running mean to represent the mean state of ocean flow, rather than a reference period mean.

The ensemble mean of 21-year running means from each ensemble member represents 105 data-points of reference surface velocity data intended to represent the mean state of surface flow while only losing ten years of data at the beginning and end of each time series. Due to internal variability, the ensemble members may differ slightly in their simulation of mean flow, but these differences are expected to be smaller than those stemming from seasonality or the effects of climate change, making an ensemble mean preferable for characterizing mean flow.

6. Methodological challenges

Long climate change projections of EKE bring with them new methodological challenges such as distinguishing ocean velocity anomalies form a shifting mean state, and characterizing EKE change that varies throughout the global ocean and may have non-linear or contradictory responses to multiple driving mechanisms. These challenges have been addressed using appropriately tailored methodology: a running-mean approach to allow for meaningful anomaly calculations and a difference-of-means approach to quantifying long-term change. However, weaknesses within these methods persist where mean conditions are not unimodal, such as the Kuroshio LM/NLM path, but comparison with observations indicates that the same issues likely affect observational studies and do not appear to be prominently addressed in the existing literature. The challenges identified with distinguishing EKE from bimodal mean conditions likely apply to many patterns of oscillation, and should be considered in a variety of contexts.

Supplementary Videos for Chapter 2 are available in the online version of Beech et al. (2022). The video captions are included here.

Supplementary Video A1. Eddy kinetic energy in the Kuroshio Current extension simulated by AWI-CM-1-1-MR (2040–2049) and calculated as in (Eq. 2.4).

Supplementary Video A2. Eddy kinetic energy in the Kuroshio Current extension observed via satellite altimetry (2017–2020). Eddy kinetic energy is calculated using geostrophic velocity anomalies relative to a 1993–2012 reference period.

Supplementary Video A3. Five-day mean magnitude of geostrophic ocean surface velocities calculated as in (Eq. 2.1) and (Eq 2.2) from sea surface heights simulated by AWI-CM-1-1-MR for CMIP6 historical simulations (1860–1861). The equatorial region (3° S to 3° N) is replaced with monthly mean velocity after linear interpolation to five-day mean time steps. Background image: NASA Earth Observatory.

	Basin	Modeled EKE (1993-2020) (km^4/s^2)	Observed EKE (1993-2020) (km^4/s^2)	Percentage Resolved (%)
a	Gulf Stream	0.228	0.393	58
b	Kuroshio Current	0.284	0.345	82.45
c	Agulhas Current	0.433	0.615	70.39
d	Brazil/Malvinas Current	0.120	0.195	61.43
e	Antarctic Circumpolar Current	0.247	0.489	50.52

Supplementary Table A1.

	Basin	σ Modeled EKE (1993–2020) (km^4/s^2)	σ Observed EKE (1993–2020) (km^4/s^2)	Percentage Resolved (%)
a	Gulf Stream	0.016	0.029	56.21
b	Kuroshio Current	0.033	0.031	107.4
c	Agulhas Current	0.022	0.021	105.71
d	Brazil/Malvinas Current	0.009	0.013	74.02
e	Antarctic Circumpolar Current	0.013	0.017	76.05

Supplementary Table A2.

	Basin	Historic EKE (1860–1949) (km^4/s^2)	Projected EKE (2061–2090) (km^4/s^2)	Percentage Change (%)
a	Gulf Stream	0.223	0.199	-10.43
b	Kuroshio Current	0.278	0.380	36.82
c	Agulhas Current	0.426	0.445	4.46
d	Brazil/Malvinas Current	0.119	0.147	23.03
e	Antarctic Circumpolar Current	0.227	0.298	31.51

Supplementary Table A3.

	Name	Historic mean (Sv)	Projected mean (Sv)	Mean difference (Sv)	Percentage difference (%)	T statistic	p(T)	Information
a	AMOC	17.504	14.490	-3.014	-17.216	30.456	1.02E-123	Zonal transect of the Atlantic at 26 °N and 1040 m depth
b	Kuroshio Current Transport	9.810	10.633	0.823	8.389	-16.093	1.12E-48	Lat/lon coordinates: (29.2 °N, 121.6 °E) to (26 °N, 128 °E), 0-150 m depth
c	Agulhas Current Transport	65.833	55.731	-10.101	-15.344	23.959	1.95E-89	Lat/lon coordinates: (-32 °N, 29 °E) to (-32 °N, 32 °E)
d	Agulas Leakage	23.297	29.743	6.446	27.670	-22.811	2.46E-83	Lat/lon coordinates: (-30.83 °N, 17.8 °E) to (-43.17 °N, 7.06 °E), 0-1200 m depth
e	Brazil Current Transport	45.975	47.967	1.992	4.333	-7.316	8.23E-13	Lat/lon coordinates: (-34.3 °N, -54 °E) to (-34.3 °N, -49 °E)
f	North Brazil Current Transport	32.178	30.258	-1.921	-5.969	14.454	7.91E-41	Lat/lon coordinates: (-6 °N, -35.3 °E) to (-6°N, -25 °E), 0–1200 m depth
g	Malvinas Current Transport	74.120	63.020	-11.100	-14.975	17.855	1.79E-57	Lat/lon coordinates: (-46 °N, -67.6 °E) to (-46 °N, -57 °E)
h	Drake Passage Throughflow	170.988	169.225	-1.763	-1.031	7.479	2.68E-13	Lat/lon coordinates: (-64.17 °N, -60.4 °E) to (-54 °N, -68 °E)

Supplementary Table A4.

References for Appendix A

Boers, N. (2021). Observation-based early-warning signals for a collapse of the Atlantic Meridional Overturning Circulation. *Nature Climate Change*, 11, 680–688. https://doi.org/10.1038/s41558-021-01097-4

Eyring, V., Bony, S., Meehl, G. A., Senior, C. A., Stevens, B., Stouffer, R. J., & Taylor, K. E. (2016). Overview of the Coupled Model Intercomparison Project Phase 6 (CMIP6) experimental design and organization. *Geoscientific Model Development*, 9(5), 1937–1958. https://doi.org/10.5194/gmd-9-1937-2016

Haarsma, R. J., Roberts, M. J., Vidale, P. L., Senior, C. A., Bellucci, A., Bao, Q., Chang, P., Corti, S., Fučkar, N. S., Guemas, V., von Hardenberg, J., Hazeleger, W., Kodama, C., Koenigk, T., Leung, L. R., Lu, J., Luo, J.-J., Mao, J., Mizielinski, M. S., Mizuta, R., Nobre, P., Satoh, M., Scoccimarro, E., Semmler, T., Small, J., & von Storch, J.-S. (2016). High Resolution Model Intercomparison Project (HighResMIP v1.0) for CMIP6, *Geoscientific Model Development*, 9, 4185–4208, https://doi.org/10.5194/gmd-9-4185-2016

Hewitt, H. T., Roberts, M., Mathiot, P. et al. (2020). Resolving and Parameterising the Ocean Mesoscale in Earth System Models. *Current Climate Change Reports*, 6, 137–152. https://doi.org/10.1007/s40641-020-00164-w

Hu, S., Sprintall, J., Guan, C., McPhaden, M. J., Wang, F., Hu, D., & Cai, W. (2020). Deep-reaching acceleration of global mean ocean circulation over the past two decades. *Science Advances*, 6(6). https://doi.org/10.1126/sciadv.aax7727

Jullien, S., Masson, S., Oerder, V., Samson, G., Colas, F., & Renault, L. (2020). Impact of Ocean–Atmosphere Current Feedback on Ocean Mesoscale Activity: Regional Variations and Sensitivity to Model Resolution. *Journal of Climate*, 33(7), 2585-2602. https://doi.org/10.1175/JCLI-D-19-0484.1

Lagerloef, G. S., Mitchum, G. T., Lukas, R. B., & Niiler, P. P. (1999). Tropical Pacific near-surface currents estimated from altimeter, wind, and drifter data. *Journal of Geophysical Research: Oceans*, 104(C10), 23313-23326. https://dx.doi.org/10.1029/1999jc900197

Latif, M., Roeckner, E., Botzet, M., Esch, M., Haak, H., Hagemann, S., Jungclaus, J., Legutke, S., Marsland, S., Mikolajewicz, U., & Mitchell, J. (2004). Reconstructing, Monitoring, and Predicting Multidecadal-Scale Changes in the North Atlantic Thermohaline Circulation with Sea Surface Temperature. *Journal of Climate*, 17(7), 1605-1614. https://doi.org/10.1175/1520-0442(2004)017<1605:RMAPMC>2.0.CO;2

Legeais, J., & Taburet, G. (2018). Algorithm Theoretical Basis Document Sea Level. Retrieved October 19, 2021, from https://datastore.copernicus-climate.eu/documents/satellite-sea-level/C3S_D312a_Lot2.2.1.2-v2_ATBD.pdf

Lique, C., & Thomas, M. D. (2018). Latitudinal shift of the Atlantic Meridional Overturning Circulation source regions under a warming climate. *Nature Climate Change*, 8, 1013–1020. https://doi.org/10.1038/s41558-018-0316-5

Ma, X., Jing, Z., Chang, P., Liu, X., Montuoro, R., Small, R. J., Bryan, F. O., Greatbatch, R. J., Brandt, P., Wu, D., Lin, X. & Wu, L. (2016). Western boundary currents regulated by interaction between

ocean eddies and the atmosphere. *Nature*, 535(7613), 533-537. https://doi.org/10.1038/nature18640

Rackow, T., & Juricke, S. (2020). Flow-dependent stochastic coupling for climate models with high ocean-to-atmosphere resolution ratio. *Quarterly Journal of the Royal Meteorological Society*, 146(726), 284–300. https://doi.org/10.1002/qj.3674

Rahmstorf, S., Box, J., Feulner, G., Mann, M. E., Robinson, A., Rutherford,S., & Schaffernicht, E. J., (2015). Exceptional twentieth-century slowdown in Atlantic Ocean overturning circulation. *Nature Climate Change*, 5, 475–480. https://doi.org/10.1038/nclimate2554

Semmler, T., Danilov, S., Gierz, P., Goessling, H. F., Hegewald, J., Hinrichs, C., et al. (2020). Simulations for CMIP6 with the AWI climate model AWI-CM-1-1. *Journal of Advances in Modeling Earth Systems*, 12, e2019MS002009. https://doi.org/10.1029/2019MS002009

Stevens, B., Giorgetta, M., Esch, M., Mauritsen, T., Crueger, T., Rast, S., et al. (2013). Atmospheric component of the MPI-M earth system model: ECHAM6. *Journal of Advances in Modeling Earth Systems*, 5, 146–172. https://doi.org/10.1002/jame.20015

Wu, B., Lin, X., & Yu, L. (2021). Poleward Shift of the Kuroshio Extension Front and Its Impact on the North Pacific Subtropical Mode Water in the Recent Decades. *Journal of Physical Oceanography*, 51(2), 457-474. https://doi.org/10.1175/JPO-D-20-0088.1

Yang, H., Lohmann, G., Krebs-Kanzow, U., Ionita, M., Shi, X., Sidorenko, D., et al. (2020). Poleward shift of the major ocean gyres detected in a warming climate. *Geophysical Research Letters*, 47. https://doi.org/10.1029/2019GL085868

Yang, H., Lohmann, G., Wei, W., Dima, M., Ionita, M., and Liu, J. (2016). Intensification and poleward shift of subtropical western boundary currents in a warming climate, *Journal of Geophysical Research: Oceans*, 121, 4928– 4945. https://doi.org/10.1002/2015JC011513

Appendix B. Supplementary information for Chapter 3

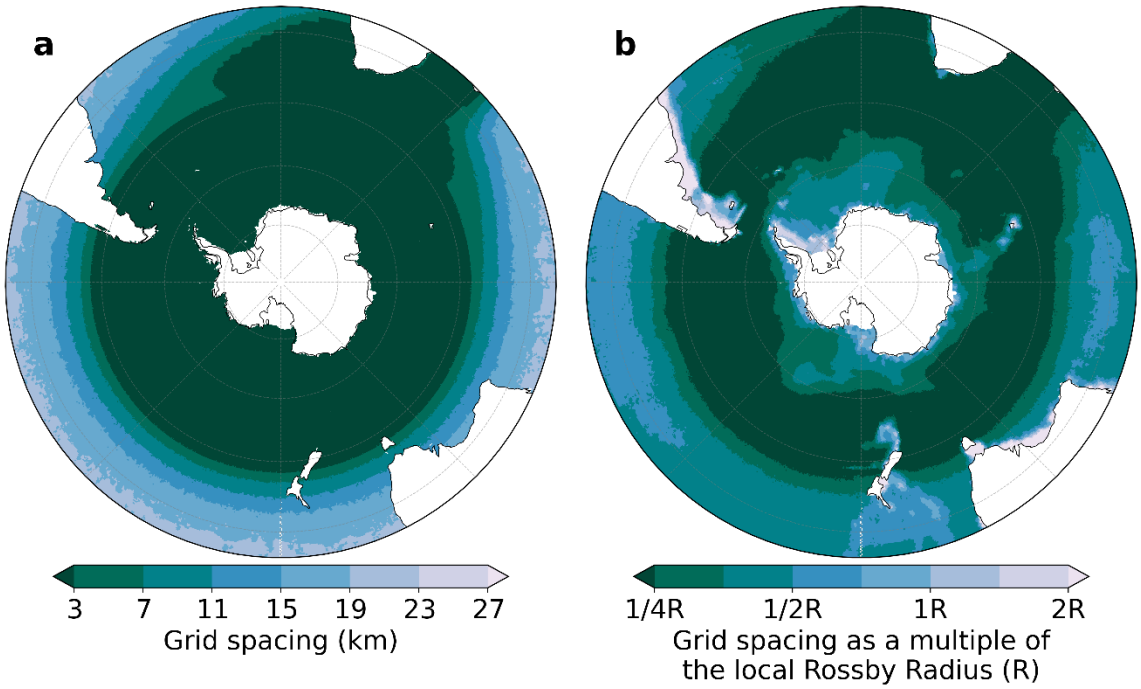

Supplementary Figure B1. Grid resolution of the SO3 mesh. (a) grid resolution expressed as approximate element height following Danilov (2022). **(b)** Grid resolution expressed as a multiple of the local Rossby radius.

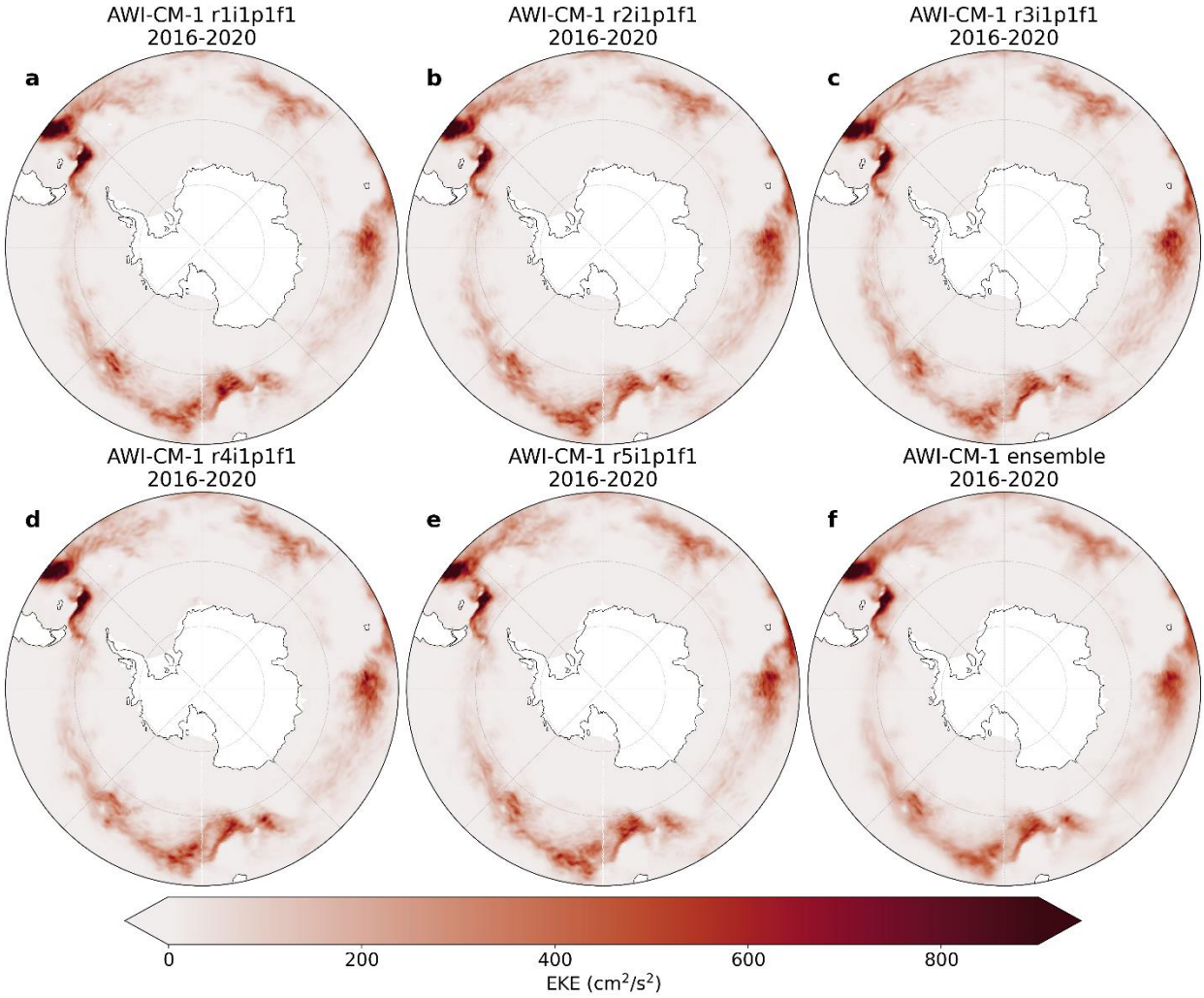

Supplementary Figure B2. Ensemble spread of mean EKE. Mean EKE during 2016–2020 in **(a–e)** each member of the AWI-CM-1 ensemble and **(f)** the ensemble mean.

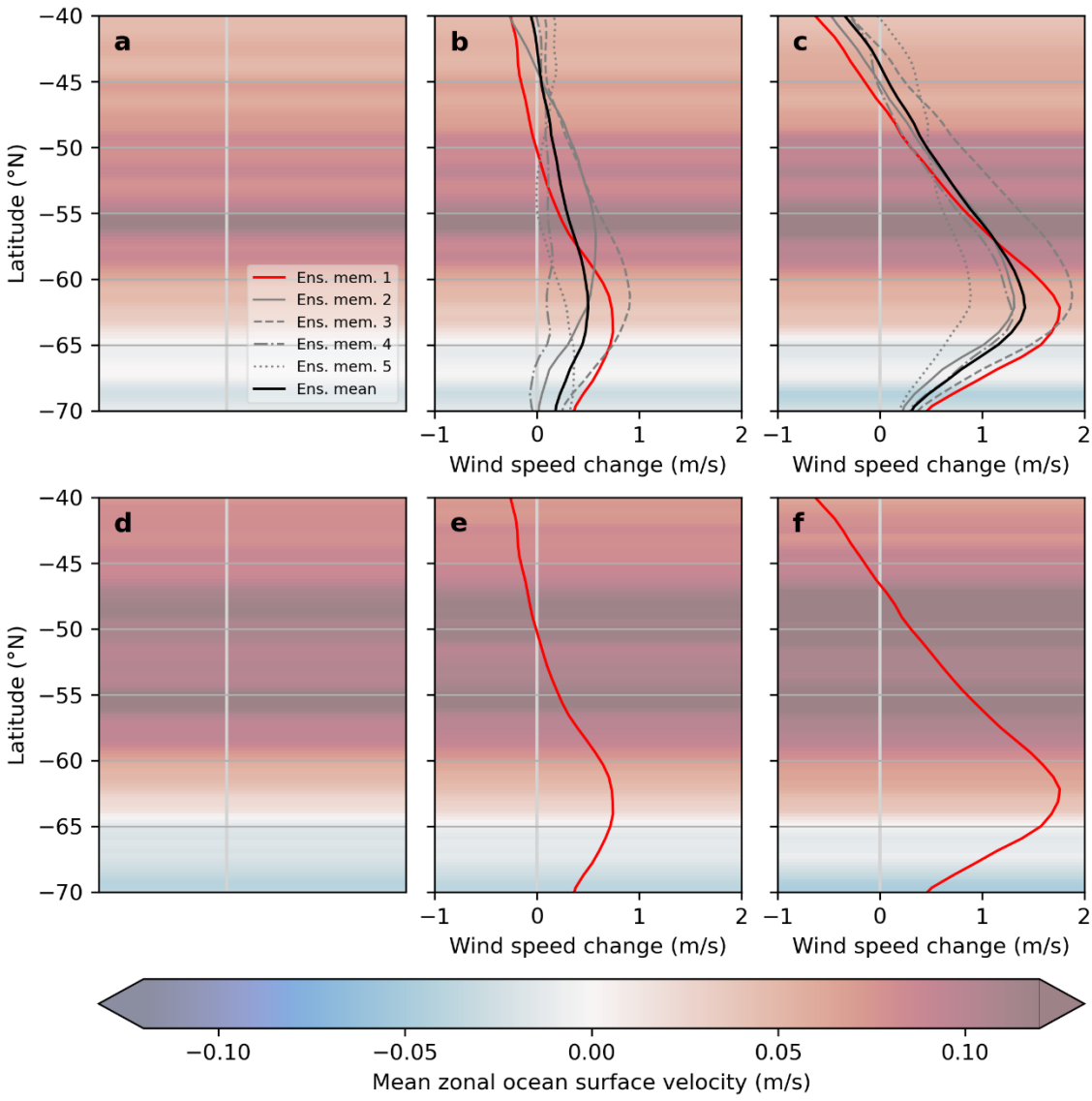

Supplementary Figure B3. Zonal mean wind speed and surface velocities. Mean zonal surface velocities during the 1951–1955 **(a,d)**, 2016–2020 **(b,e)**, and 2091–2095 **(c,f)** periods in the AWI-CM-1 ensemble **(a–c)** and the SO3 simulations **(d–f)**. Changes in mean zonal wind speeds relative to the 1951–1955 mean are overlaid.

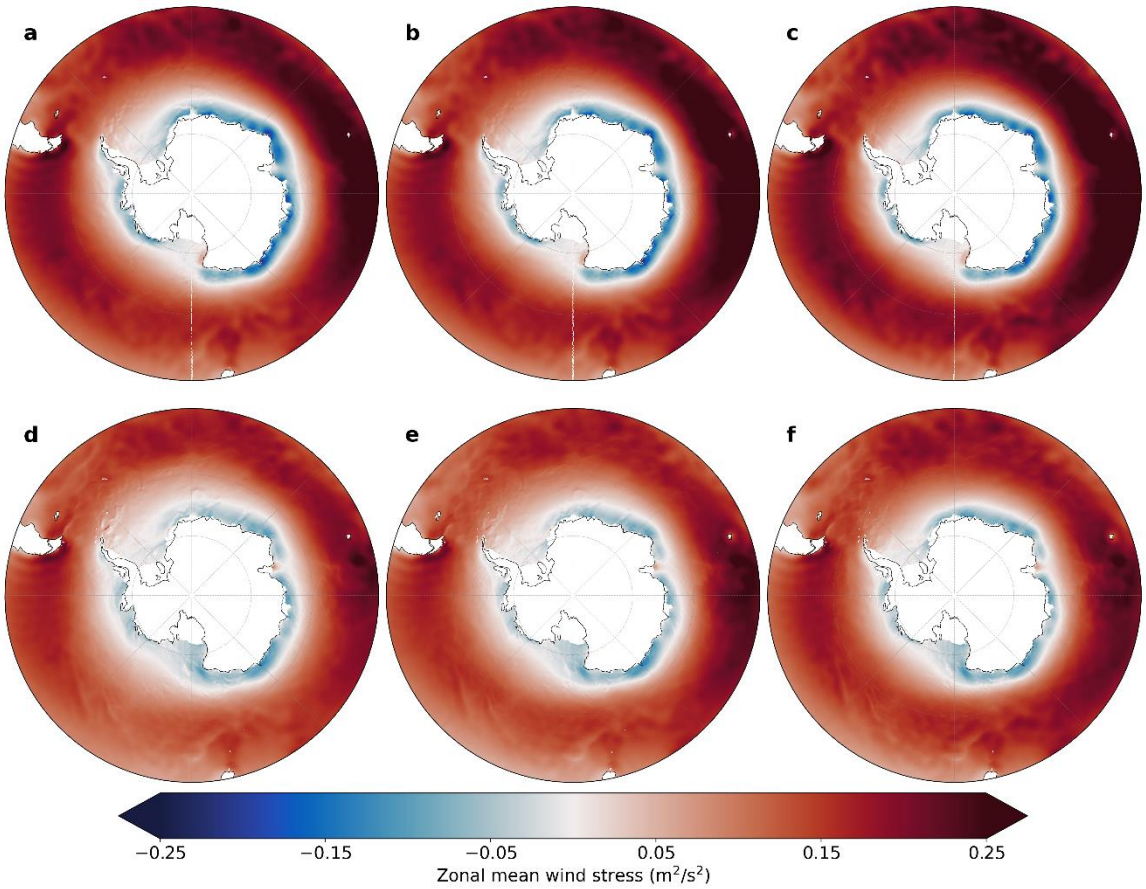

Supplementary Figure B4. Zonal mean wind stress. Zonal mean wind stress to the ocean surface in AWI-CM-1 ensemble member 1 **(a–c)** and the SO3 simulations **(d–f)** during the periods 1951–1955 **(a,d)**, 2016–2020 **(b,e)** and 2091–2095 **(c,f)**. Positive values indicate an eastward direction.

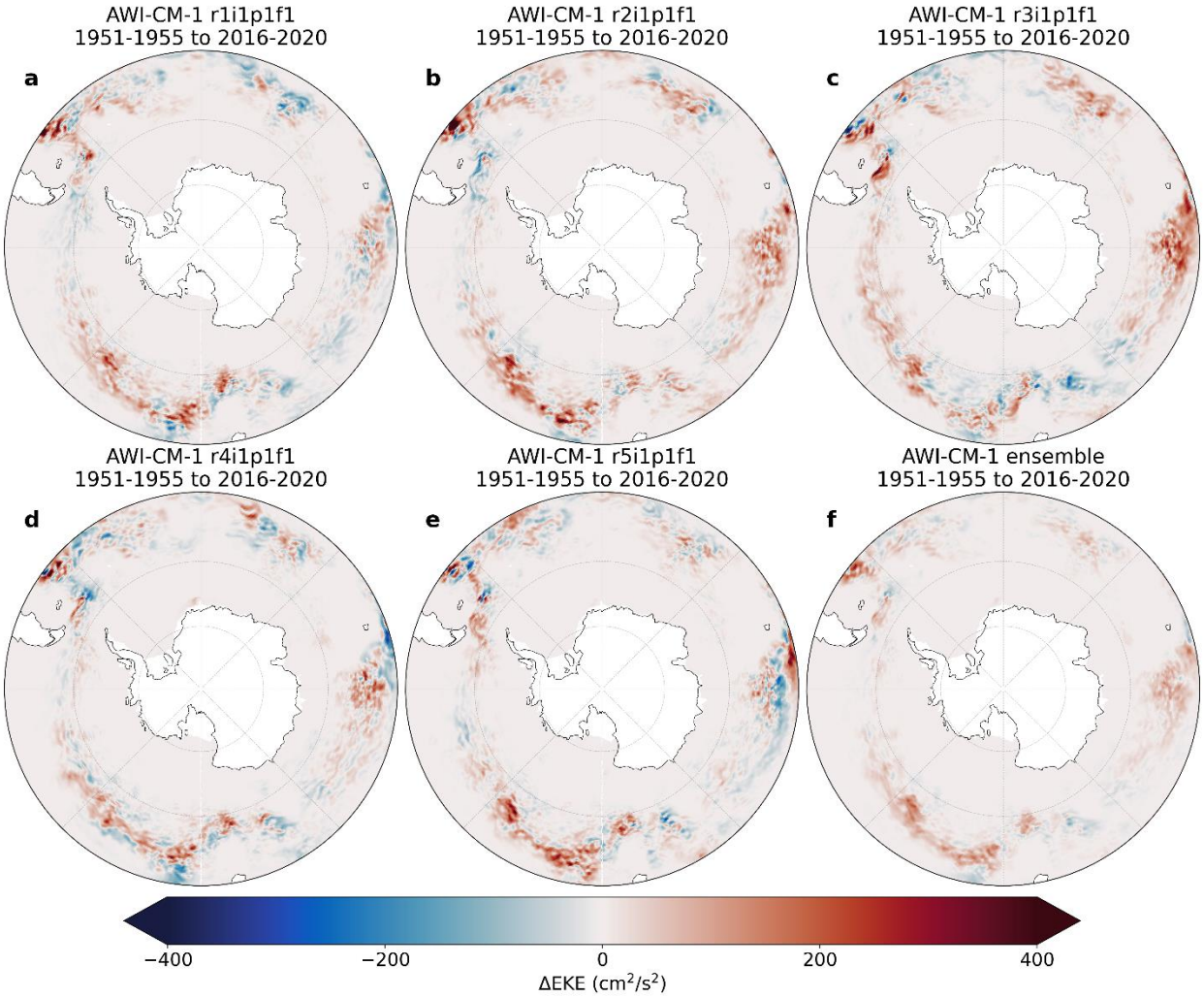

Supplementary Figure B5. Ensemble spread of EKE change between 1951–1955 and 2016–2020. EKE change in **(a–e)** each member of the AWI-CM-1 ensemble and **(f)** the ensemble mean.

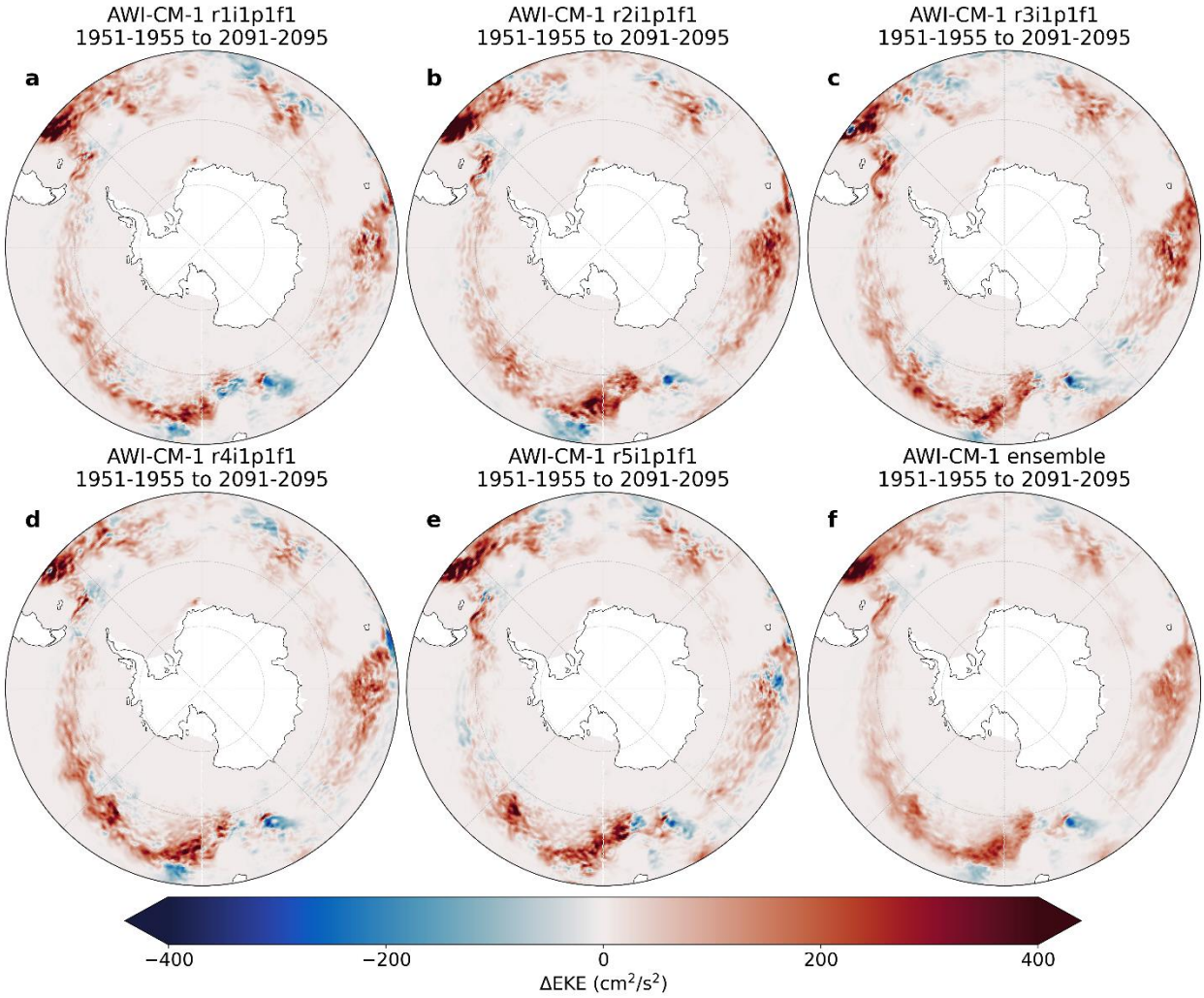

Supplementary Figure B6. Ensemble spread of EKE change between 1951–1955 and 2091–2095. EKE change in **(a–e)** each member of the AWI-CM-1 ensemble and **(f)** the ensemble mean.

Data	Durbin-Watson	Skew	p(Skew)	Kurtosis	p(Kurt)
Ens. 1	0.169	0.867	p<0.001	0.536	0.056
Ens. 2	0.232	-0.075	0.549	-0.156	0.623
Ens. 3	0.283	0.198	0.119	-0.270	0.289
Ens. 4	0.179	0.176	0.165	-0.220	0.423
Ens. 5	0.214	0.400	0.002	-0.439	0.040
Ensemble	0.206	0.381	p<0.001	0.237	0.052
SO3	0.44	0.432	0.001	0.013	0.813

Supplementary Table B1. EKE statistics for the 1951–1955 period. Statistical properties reported are autocorrelation (Durbin & Watson, 1950), skewness (D'Agostino & Belanger, 1990), and kurtosis (Fisher, 1997). Statistics are calculated using 5-day mean EKE data with linear trends removed as in Figures 3.1a,b,c and Figure 3.3.

Data	Durbin-Watson	Skew	p(Skew)	Kurtosis	p(Kurt)
Ens. 1	0.226	0.295	0.021	-0.335	0.157
Ens. 2	0.255	0.451	0.001	-0.454	0.031
Ens. 3	0.245	-0.175	0.167	-0.220	0.425
Ens. 4	0.216	0.022	0.860	-0.480	0.020
Ens. 5	0.267	0.339	0.009	0.164	0.427
Ensemble	0.251	0.179	0.002	-0.263	0.010
SO3	0.387	0.417	0.001	-0.509	0.011
Obs.	0.499	0.032	0.801	-0.146	0.658

Supplementary Table B2. EKE statistics for the 2016–2020 period. Statistical properties reported are autocorrelation (Durbin & Watson, 1950), skewness (D'Agostino & Belanger, 1990), and kurtosis (Fisher, 1997). Statistics are calculated using 5-day mean EKE data with linear trends removed as in Figures 3.1a,b,c and Figure 3.3.

Data	Durbin-Watson	Skew	p(Skew)	Kurtosis	p(Kurt)
Ens. 1	0.14	-0.085	0.502	-0.329	0.167
Ens. 2	0.15	0.331	0.010	-0.698	p<0.001
Ens. 3	0.264	-0.150	0.235	-0.27	0.289
Ens. 4	0.199	0.134	0.289	-0.472	0.023
Ens. 5	0.133	-0.031	0.806	-0.981	p<0.001
Ensemble	0.168	0.067	0.244	-0.476	p<0.001
SO3	0.219	-0.345	0.008	-0.484	0.018

Supplementary Table B3. EKE statistics for the 2091–2095 period. Statistical properties reported are autocorrelation (Durbin & Watson, 1950), skewness (D'Agostino & Belanger, 1990), and kurtosis (Fisher, 1997). Statistics are calculated using 5-day mean EKE data with linear trends removed as in Figures 3.1a,b,c and Figure 3.3.

References for Appendix B

D'Agostino, R. B., & Belanger, A. (1990). A Suggestion for Using Powerful and Informative Tests of Normality. *The American Statistician*, 44(4), 316–321. https://doi.org/10.2307/2684359

Danilov, S. (2022). On the Resolution of Triangular Meshes. *Journal of Advances in Modeling Earth Systems*, 14(10), e2022MS003177. https://doi.org/10.1029/2022MS003177

Durbin, J., & Watson, G. S. (1950). Testing for Serial Correlation in Least Squares Regression. I. *Biometrika*, 37(3–4), 409–428. https://doi.org/10.1093/biomet/37.3-4.409

Fisher, R. A. (1997). The moments of the distribution for normal samples of measures of departure from normality. *Proceedings of the Royal Society of London. Series A, Containing Papers of a Mathematical and Physical Character*, 130(812), 16–28. https://doi.org/10.1098/rspa.1930.0185

Appendix C. Supplementary information for Chapter 4

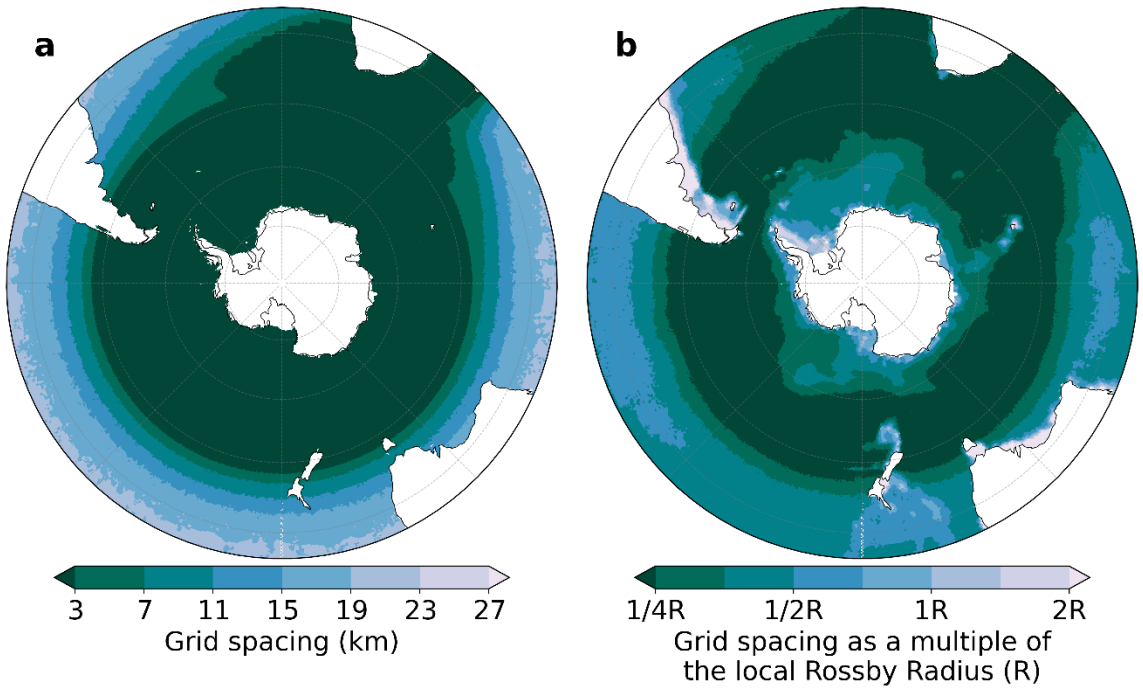

Supplementary Figure C1. Model grid resolution. (a) Grid resolution expressed as approximate element height following Danilov (2022). **(b)** Grid resolution expressed as a multiple of the local Rossby radius.

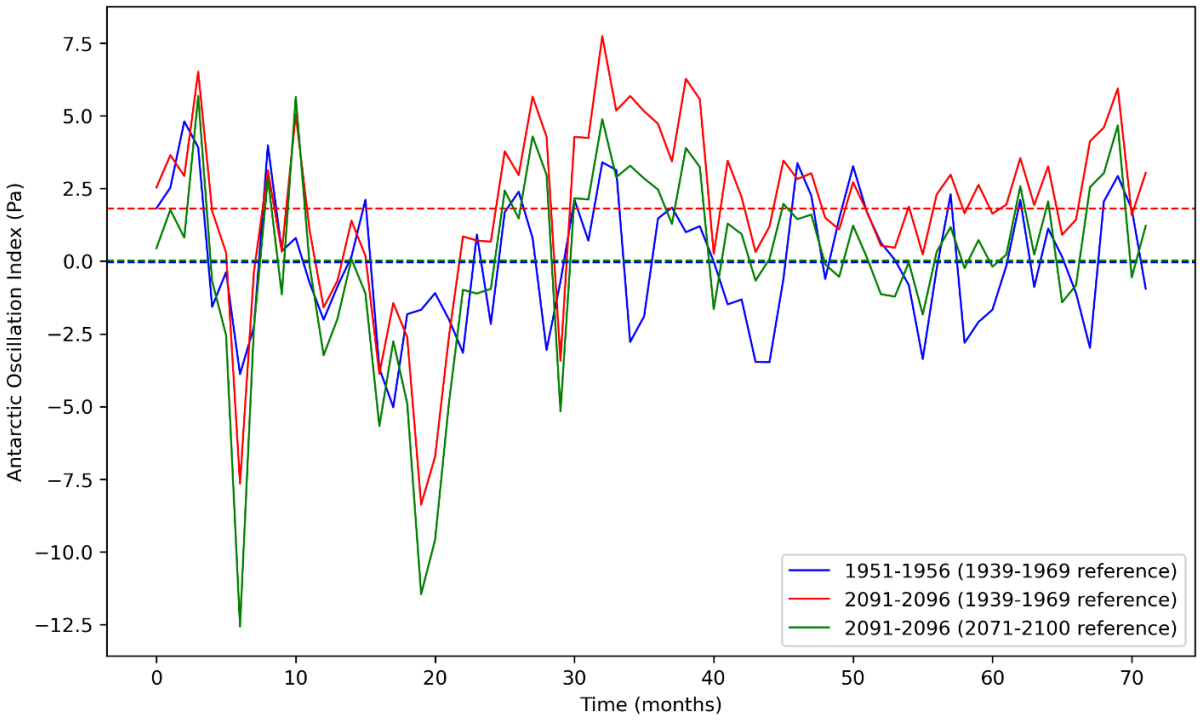

Supplementary Figure C2. Antarctic Oscillation Index. A measure of the state of the Southern Annular Mode calculated for conditions in 1951–1956 (blue) and 2091–2096 (red) relative to historic 30-year (1939–1969) average simulated conditions and for 2091–2096 (green) relative to projected (2071–2100) average simulated conditions. Average AOI values are plotted as dashed lines.

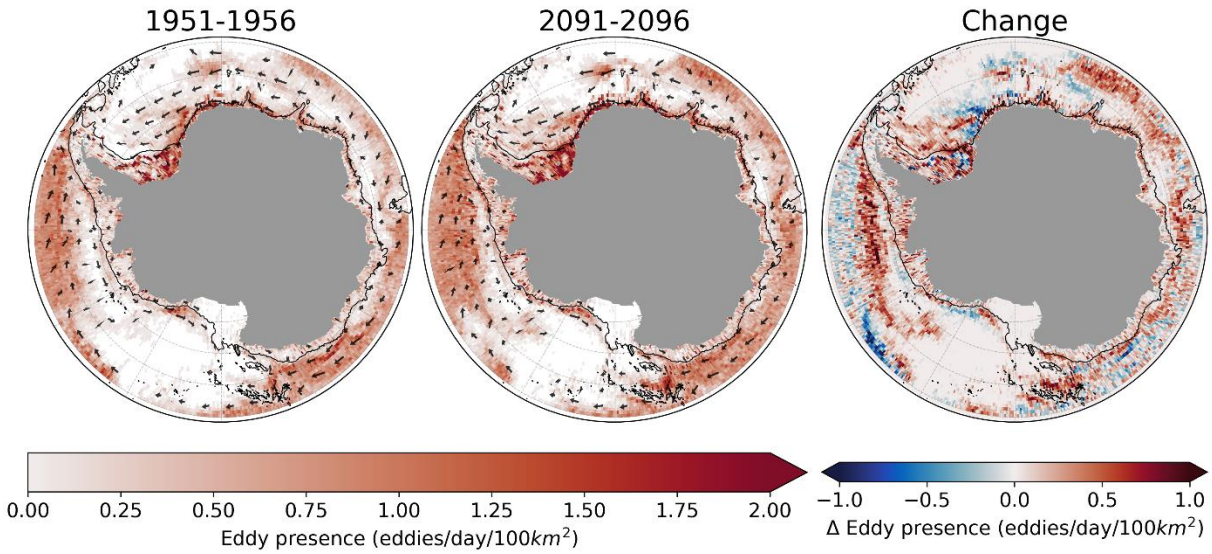

Supplementary Figure C3. Same as Figure 4.1 but for 0–5 m depth.

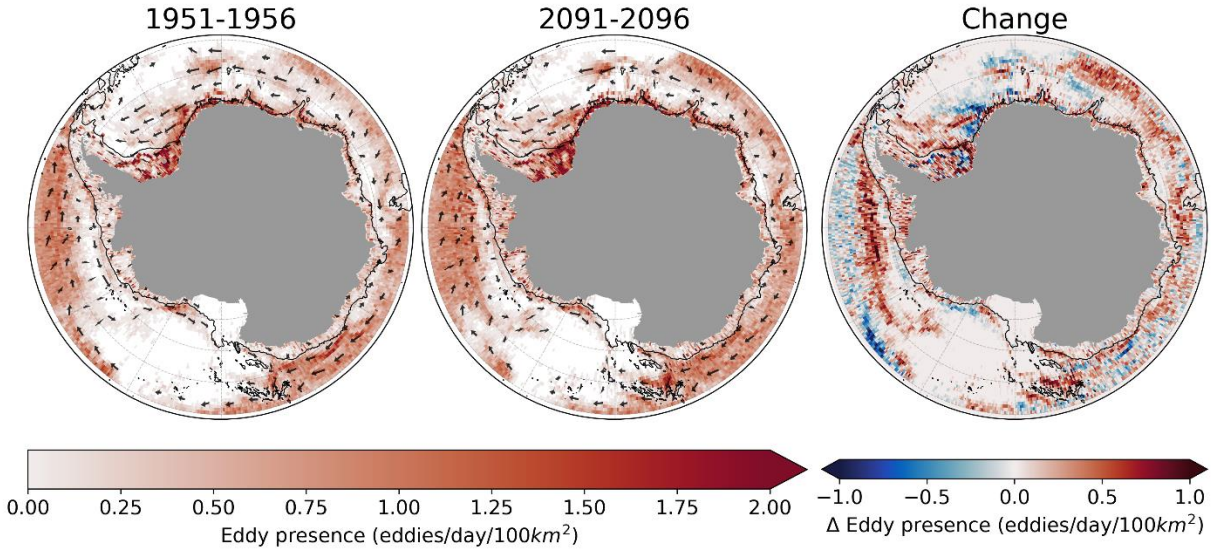

Supplementary Figure C4. Same as Figure 4.1 but for 25–30 m depth.

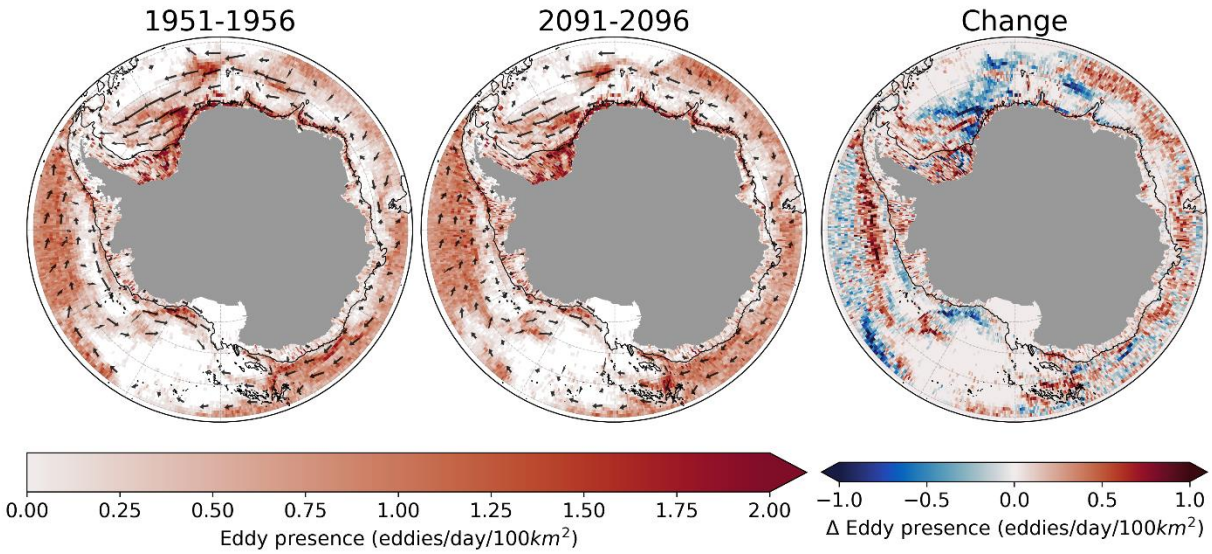

Supplementary Figure C5. Same as Figure 4.1 but for 190–200 m depth.

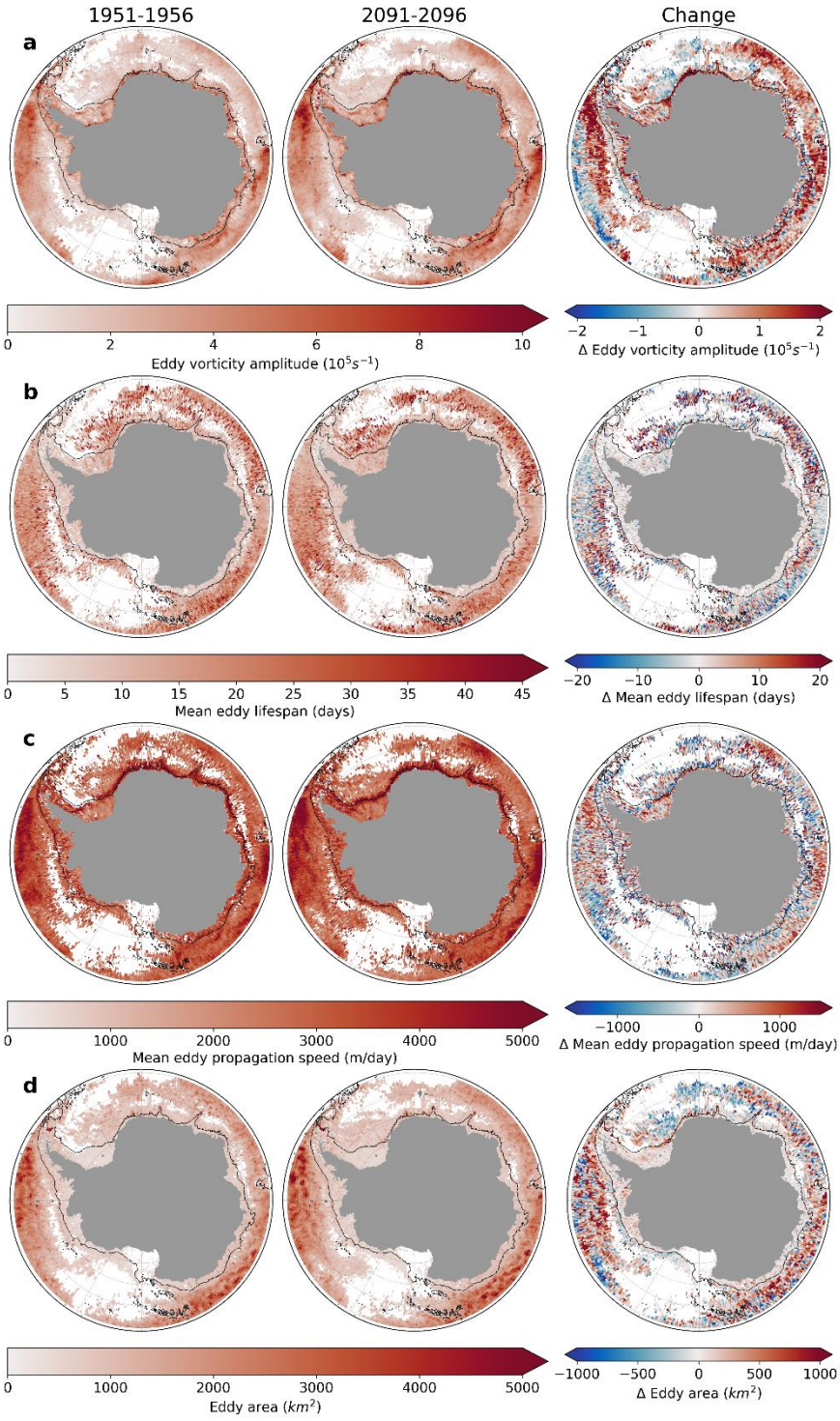

Supplementary Figure C6. Same as Figure 4.2 but for 0–5 m depth.

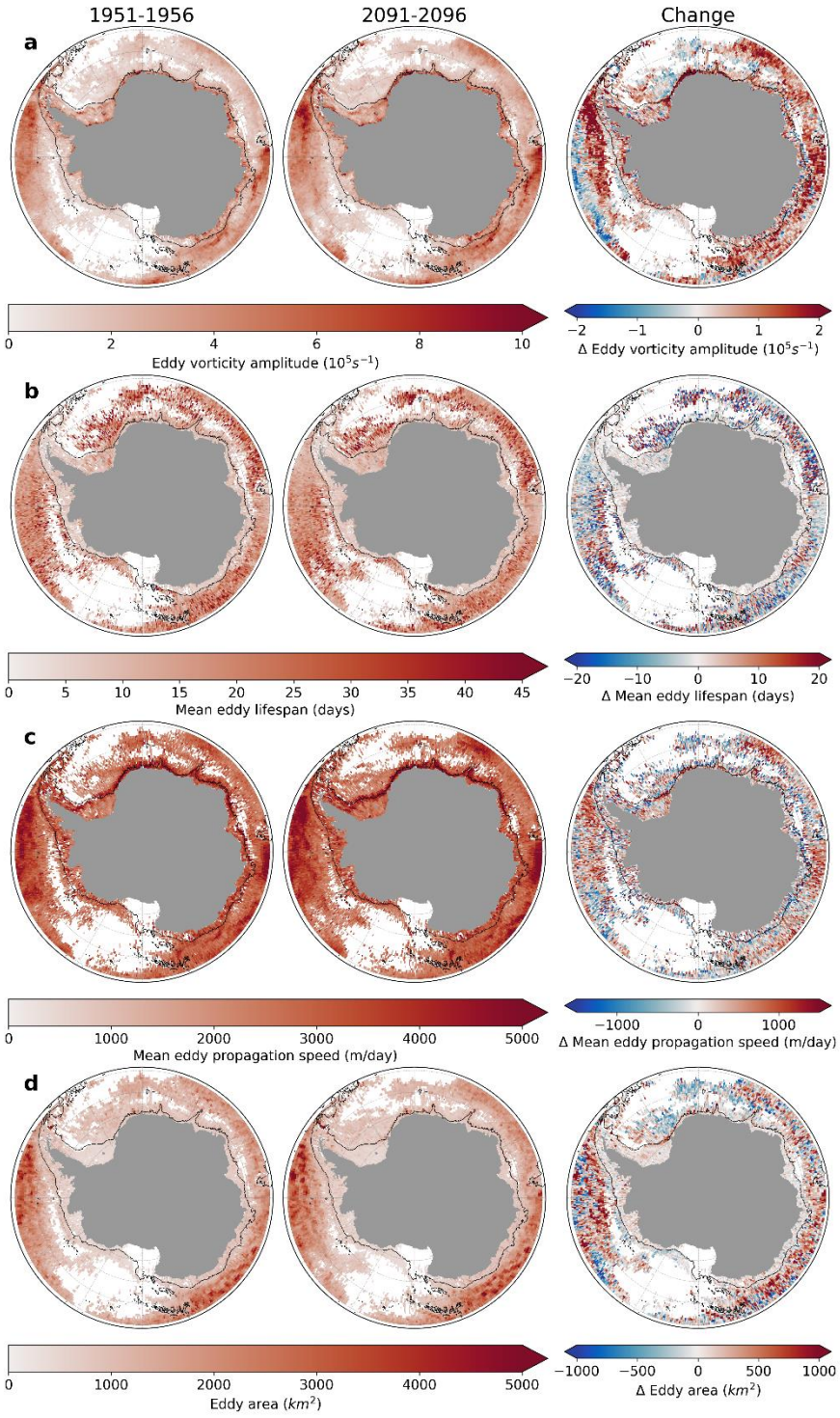

Supplementary Figure C7. Same as Figure 4.2 but for 25–30 m depth.

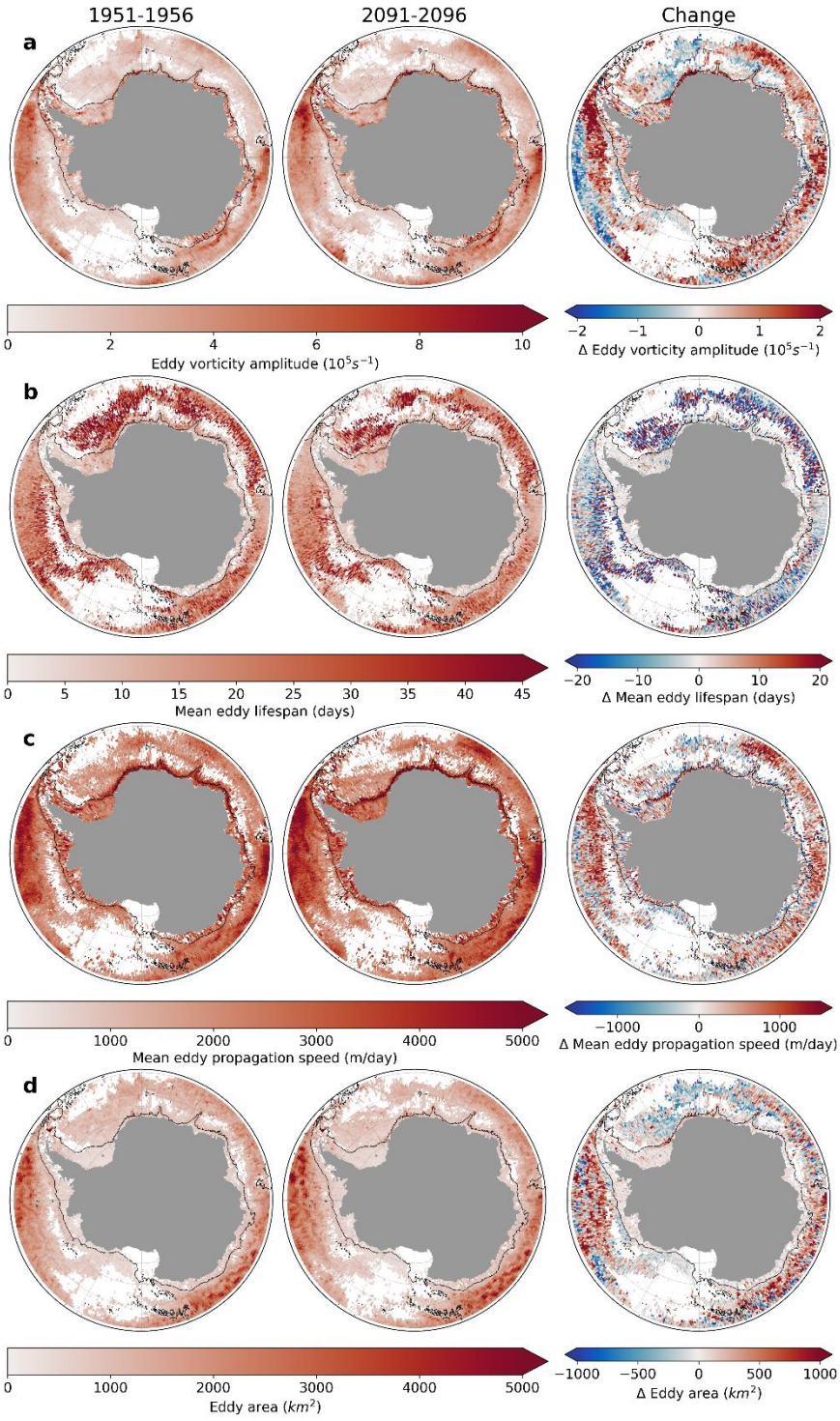

Supplementary Figure C8. Same as Figure 4.2 but for 190–200 m depth.

Acknowledgements

Firstly, I thank Prof. Dr. Thomas Jung, Dr. Tido Semmler, and Dr. Thomas Rackow for their consistent support over the years. There is not much in this thesis that would be there without them.

Thanks as well to Dr. Sergey Danilov and Dr. Qiang Wang for their contributions as coauthors and for all the Friday meetings.

Thanks to Dr. Nikolay Koldunov for answering more than a few questions.

Special thanks to Sarah and Rog for putting up with me spending so long away.

A million thanks to Julia for more than I can write.

Thanks to the Freunde von Fiets for helping paddle the canoe.

Finally, thanks to Woodstock for everything else.